ALMA MATER STUDIORUM-UNIVERSITÀ DI BOLOGNA

DOTTORATO DI RICERCA

FISICA

Ciclo XXI

Settore scientifico disciplinare

FIS/04

Fisica Nucleare e Subnucleare

Study of production of high-P_T leptons and limits on single top production at HERA

Presentata da: Stefano Antonelli

Coordinatore Dottorato:	Relatore:
Prof. F. Ortolani	Prof. G. Venturi

Esame Finale anno 2009

Contents

Introduction

The Standard Model (SM) of particle physics describes the electroweak and strong interactions of elementary particles with excellent accuracy over the whole energy range currently accessible to experiments. However, many fundamental facts remain unexplained like the quark-lepton symmetry and the structure of gauge groups. Also the incorporation of gravity has not succeeded yet. The experimental observation of a deviation from the SM could provide an important guidance to develop theories providing a deeper understanding of the structure of the matter. Rare SM processes with clean experimental signatures are good candidates to look for such deviations. At HERA, events with isolated leptons and large missing transverse momentum are an example with a very low rate expected from SM processes. Any excess over this predictions would provide a hint of new physics beyond the SM. One SM process, the direct production of single W boson with subsequent leptonic decay which leads to an event with isolated lepton and high missing transverse momentum has a measurable cross section of about 1 pb. The production of single t quark via flavour changing neutral current (FCNC, anomalous coupling between u quark, t quark and a photon or Z boson) also leads to isolated leptons and large missing transverse momentum by its dominant decay to a W boson and a b quark with the W decaying leptonically: $ep \rightarrow etX$, $t \rightarrow W^+b$, $W^+ \rightarrow e^+\nu$, $\mu^+\nu$, $\tau^+\nu$. These events are charac-

terised by the presence of additional large hadronic transverse momentum originating from b quark. However, in the Standard Model, no sizable cross section for top production is predicted since the charged current (CC) process $ep \to \nu tX$ at HERA has a cross section less than 1 fb. On the other hand, many extensions of the SM, such as anomalous magnetic coupling $\kappa_{\gamma u}, \gamma_{Zu}$, anomalous vector and axial coupling to the Z, v_Z, a_Z, contain processes which enhance the rate of FCNC with singly produced t quarks.

In this thesis we studied the events with isolated leptons and missing transverse momentum using data collected by the ZEUS detector during the HERA running period 2004-2005 (lepton beam e) and 2006-2007 (e^+ beam), corresponding to an integrated luminosity of $278\,\mathrm{pb}^{-1}$.

This thesis is organized as follows:

- Chapter 1: the HERA collider and the ZEUS detector are presented with emphasis on the detector components used in the analysis.
- Chapter 2: a teorethical overview of the lepton-nucleon scattering at HERA with emphasis on the processes which involve the production of high-p_T isolated leptons.
- Chapter 3: an overview of the event topology and the search strategy.
- Chapter 4: a summary of the data samples used and the simulation of the background and signal events.
- Chapter 5: a description of the methods for the event reconstruction.
- Chapter 6: this chapter is dedicated to the analysis on isolated leptons. Plots of some kinematical variables compared to the Monte Carlo prediction are shown.

- Chapter 7: this chapter is dedicated to the study on limits of single top cross section and $\kappa_{tu\gamma}$.

- Chapter 8: this chapter is dedicated to the conclusions.

Chapter 1

HERA and the ZEUS detector

In this chapter the HERA accelerator and the ZEUS detector are described briefly, giving particular emphasis on the parts of the detector used in the analysis described in this thesis. A detailed description of the ZEUS detector can be found in [1].

1.1 The HERA collider

The HERA (Hadron Elektron Ring Anlage) collider was a unique particle accelerator for the study of high energy electron[1]-proton (ep) collisions [2].

It was located at the DESY (Deutsches Electronen SYnchrotron) laboratory in Hamburg, Germany, and has been in operation from 1992 to 2007. The HERA ring was located ≈ 30 m under ground level and had a circumference of 6.3 km. Fig. 1.1 shows an aerial view of the tunnel area in Hamburg and the position of the different experimental halls; the ring had 4 linear sections linked at their extremities by 4 arcs of 779 m radius, see Fig. 1.2. The HERA machine collided electrons, accelerated to an energy of 27.5 GeV ,

[1]Electron refers both to electrons and positrons unless stated otherwise.

Figure 1.1: *The Hamburg Volkspark showing the DESY site. The location of the HERA and PETRA rings are shown.*

with 920 (820) GeV protons (the energy of the proton beam was changed at the beginning of 1998 from 820 to 920 GeV). The resulting center-of-mass energy was 318 (300) GeV , more than an order of magnitude higher than previous fixed-target lepton-nucleon experiments.

1.1.1 The HERA injection system

HERA provided two different injection systems for the beams, shown in Fig. 1.2.

The proton acceleration chain started with negative hydrogen ions (H^-) accelerated in a LINAC to 50 MeV. The electrons were then stripped off the H^- ions to obtain protons, which were injected into the proton synchrotron DESY III and accelerated up to 7.5 GeV in 11 bunches with a temporal gap of 96 ns, the same as the main HERA ring; these bunches were then transferred to PETRA, where they were accelerated to 40 GeV. Finally they were injected into the HERA proton storage ring, and the injection stopped

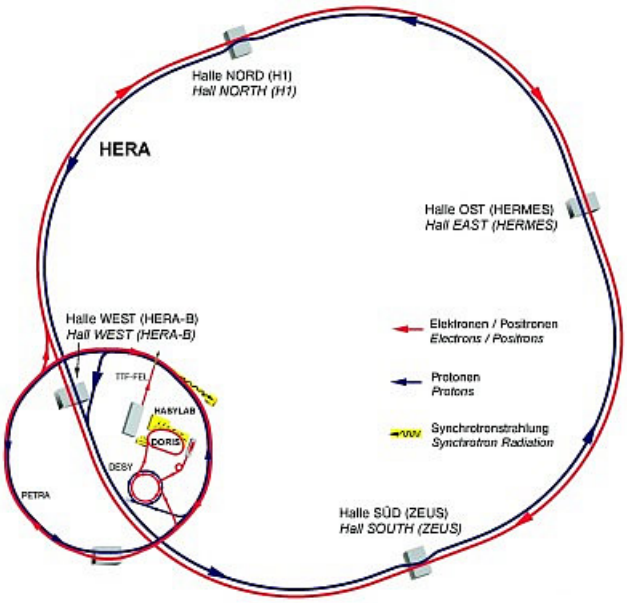

Figure 1.2: *HERA injection system.*

when the ring contained 180 bunches. Through the radiofrequency generated in resonant cavities, the proton beam was then accelerated up to 920 GeV. Pre-acceleration of the electrons started in two cascaded linear accelerators, LINAC I and LINAC II, where the leptons were accelerated up to 250 and 450 MeV respectively. The leptons were then injected into DESY II, accelerated to 7.5 GeV and then transferred to PETRA II, where they reached an energy of 14 GeV in bunches separated by 96 ns gaps. They were injected into HERA where they reached the nominal lepton beam energy of 27.5 GeV, again until the main ring was filled with 210 bunches. Some of these bunches were kept empty (pilot bunches) in order to study the background conditions. When either the lepton or the proton bunch was empty, the beam related background, originating from the interaction of the lepton or the proton beam with the residual gas in the beam pipe, could be studied, whereas when both bunches were empty the non-beam related background, such as cosmic ray

rates, could be estimated.

1.1.2 The HERA luminosity

HERA started delivering data in June 1992. Since then the luminosity has continously increased, as shown in Fig. 1.3. At HERA, luminosity is effectively defined as:

$$L = \frac{f_r \sum_i N_p^i \cdot N_e^i}{2\pi\sigma_x\sigma_y\beta_{yp}^*} \tag{1.1}$$

where f_r represents the beam revolution frequency, N_p^i is the number of protons in the i-th bunch, N_e^i is the number of electron in the i-th bunch; σ_x, σ_y represent the interaction region sizes, where $\sigma_x = \sqrt{\sigma_{x_e}^2 + \sigma_{x_p}^2}$ and $\sigma_y = \sqrt{\sigma_{y_e}^2 + \sigma_{y_p}^2}$. These variables are connected to the corresponding beta function[2] and emittances [3]: $\sigma_\alpha = \sqrt{\beta_\alpha^* \epsilon_\alpha}$. Increasing the intensities of the beams to substantially improve the luminosity would have required a huge financial cost (the currents of the leptonic beam could only have been incremented increasing in an almost proportional way the power of the radiofrequency cavity). The luminosity was increased by making the interaction cross-section smaller by reducing the beta functions at the interaction point. These functions are limited by chromatic effects and limitations on the opening of the low beta quadrupoles. In order to increase the luminosity up to $\sim 7.4 \cdot 10^{31}\,\mathrm{cm}^{-2}\,\mathrm{s}^{-1}$ new superconducting magnets [6] close to the interaction point (inside the calorimeter volume), an absorption system for the synchrotron radiation was installed in the interaction region.

[2] The beta functions describe the beam properties at each position around the ring.

[3] The extent occupied by the particles of the beam in the phase space.

1.1.3 HERA running history

Four experiments were located in four experimental halls placed along the HERA ring (Fig. 1.1 and 1.2). The two beams were brought into collision every 96 ns at zero crossing angle at two interaction points, one in the North Hall where the H1 experiment was located, the other in the South Hall where the ZEUS experiment was placed. In the East Hall the Hermes experiment studied the spin structure of the nucleon using the collisions of longitudinally polarized leptons on an internally polarized gas target (H, 2D or 3He). The HERA-B experiment, located in the West Hall was used until 2003 to collide the proton beam halo with a wire target to study B-meson production. Built between 1984 and 1990, the HERA collider started operation in 1992 in its initial configuration with 820 GeV protons and 26.7 GeV electrons. In 1994 it was realized that the electron beam current was limited by positively ionized dust particles in the beam pipe through the pumps, reducing the lifetime of the beam. For this reason HERA switched to positrons in July 1994, achieving a more stable lepton beam and a significant increase in the integrated luminosity of the collected data. During the 1997-98 shutdown period, new pumps were installed in the lepton beam to improve the electron beam lifetime, and during 1998 and part of 1999 HERA was run again with electrons. In 1998 the energy of the proton beam was raised from 820 to 920 GeV, switching back to positron-proton collisions in 1999. This phase is called HERA I and the total delivered luminosity up to 2000 was 193.2 pb^{-1}. Although a lot of interesting measurements had already been performed at HERA I, the desire was expressed by the experiments for an increase in the luminosity. The motivations for this increase were studied in a one-year workshop held between 1995 and 1996, when it was concluded that having $\sim 1\,\mathrm{fb}^{-1}$ of integrated luminosity would open up

the possibility of new interesting measurements [3]. During the shutdown 2000/2001, the HERA collider was upgraded to achieve a five times higher specific luminosity at the collision point [4]. In addition spin rotators were included to rotate the spin of the leptons such that the lepton beam was longitudinally polarized at all interaction regions. A further longer shutdown was necessary in the middle of 2003 to solve severe background problems [5]. Since October 2003 till the beginning of 2007, HERA provided stable beam operations. During this HERA II running phase a luminosity of 556.3 pb^{-1} (equally distributed between electron and positron beam) was delivered. Before the end of data-taking (June 2007), special proton low energy runs have been delivered in order to measure the longitudinal structure function F_L. This measurement should allow to decompose the contributions of the F_L and F_2 structure functions to the DIS cross section at low Q^2 and provide an important cross check of the conventional QCD at low x; furthermore it could allow to improve the knowledge of the gluon density. HERA agreed with ZEUS and H1 collaborations to run with two different proton energies, see Table 1.2: 460 GeV (Low Energy Run, LER) and 575 GeV (Medium Energy Run, MER). HERA delivered 15.7 pb^{-1} during LER period (from January to April 2007) and 8.1 pb^{-1} during MER (from April to June 2007). A summary of HERA I and HERA II parameters during the running periods 1993-2000 and 2003-2007 can be found in Tables 1.1 and 1.2. Fig. 1.3 shows HERA luminosity during the whole working period, respectively for the two phases HERA I and HERA II. Fig. 1.4 shows, on the left, HERA luminosity for HERA II phase and, on the right, ZEUS luminosity achieved for the same period.

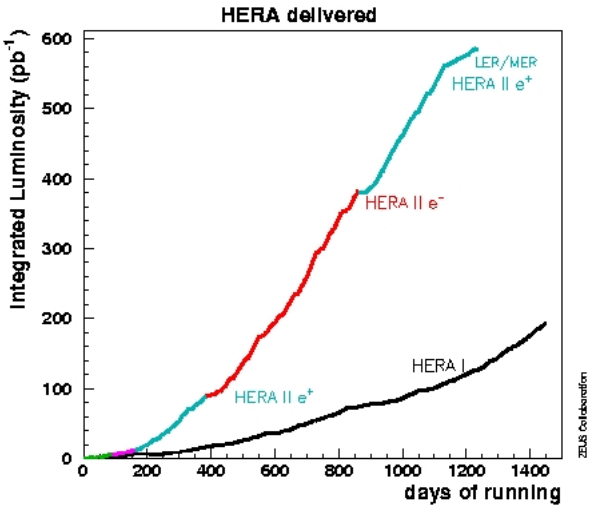

Figure 1.3: *HERA luminosity for the whole working period.*

Running period	1993-1997		1998-2000	
Luminosity	$1.5 \cdot 10^{31}\,\mathrm{cm}^{-2}\,\mathrm{s}^{-1}$		$1.5 \cdot 10^{31}\,\mathrm{cm}^{-2}\,\mathrm{s}^{-1}$	
Center-of-mass energy (GeV)	300		318	
	lepton	proton	lepton	proton
Energy (GeV)	30	820	27.5	920
Max number of bunches	210	210	210	210
Beam current (mA)	43	163	43	163
Particles per bunch	$3.65 \cdot 10^{10}$	10^{11}	$3.65 \cdot 10^{10}$	10^{11}
Beam width (σ_x) mm	0.286	0.280	0.286	0.280
Beam width (σ_y) mm	0.060	0.058	0.060	0.058

Table 1.1: *HERA I design parameters [7], [8].*

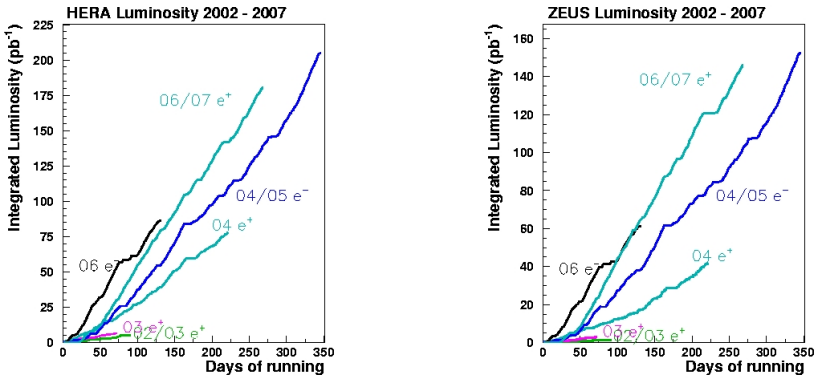

Figure 1.4: *HERA and ZEUS luminosity for HERA II.*

Running period	2003-2006		2007 LER		2007 MER	
Luminosity	$7.0 \cdot 10^{31}\,\mathrm{cm}^{-2}\,\mathrm{s}^{-1}$		$1.47 \cdot 10^{31}\,\mathrm{cm}^{-2}\,\mathrm{s}^{-1}$		$1.47 \cdot 10^{31}\,\mathrm{cm}^{-2}\,\mathrm{s}^{-1}$	
Center-of-mass energy (GeV)	318		225		251	
	lepton	proton	lepton	proton	lepton	proton
Energy (GeV)	27.5	920	27.5	460	27.5	575
Max number of bunches	184	180	180	180	180	180
Beam current (mA)	58	140	38	140	58	140
Particles per bunch	$4.18 \cdot 10^{10}$	10^{11}	$4.18 \cdot 10^{10}$	10^{11}	$4.18 \cdot 10^{10}$	10^{11}
Beam width (σ_x) mm	0.118	0.118	0.118	0.118	0.118	0.118
Beam width (σ_y) mm	0.032	0.032	0.032	0.032	0.032	0.032

Table 1.2: *HERA II design parameters [7], [8].*

1.2 The ZEUS detector

ZEUS was a multi-purpose, magnetic detector designed to study electron proton collisions. It measured $12 \times 10 \times 19\,\mathrm{m}^3$, weighted 3600 tons and it was quasi-hermetic, covering most of the 4π solid angle, with the exception of the

small regions around the beam pipe. As a result of the asymmetric beam energies, most of the final state particles were boosted in the proton beam direction. Consequently, the sub-detectors of ZEUS were coaxial but asymmetric with respect to the interaction point. For low momentum charged particles, the tracking in the magnetic field was very precise, while high energy particles were well measured by the calorimetric system (see Sections 1.4 and 1.6). Particle identification was needed in a wide momentum range to achieve the physics goals. In neutral nurrent (NC) deep inelastic scattering (DIS) events the scattered lepton has to be identified and measured with high precision and the identification of electrons, positrons and muons is also needed in order to study the semi-leptonic decay of heavy quarks and exotic processes involving leptons. In charged current (CC) DIS processes a hermetic detector is needed in order to reconstruct the missing transverse momentum carried by the outgoing neutrino. In these kinds of events and also in untagged photoproduction events, the precise reconstruction of the final state was important in order to determine the event kinematics. The ZEUS coordinate system was a right-handed, cartesian system with the origin defined as the nominal Interaction Point (IP)[4]. Since the proton-beam axis has a slight tilt, the y axis does not precisely coincide with the vertical. The actual IP varies from event to event, and the average proton tilt varies on a fill-by-fill basis. Polar angles were defined with respect to the proton beam direction ($\theta = 0$) and the leptonic beam is therefore at $\theta = \pi$. The azimuthal angles ϕ were measured with respect to the x axis. The pseudo rapidity variable is often used in event analysis; this quantity is an approximation at

[4]The ZEUS coordinate system is a right-handed Cartesian system, with the Z axis pointing in the proton beam direction, referred to as the "forward direction", and the X axis pointing left towards the center of HERA. The coordinate origin is at the nominal interaction point.

high energies of the particle rapidity given by $y = \log \frac{E+P_z}{E-P_z}$ and is defined by $\eta = -\log(\tan \frac{\theta}{2})$, where θ is the polar angle. The ZEUS coordinate system is illustrated in Fig. 1.5.

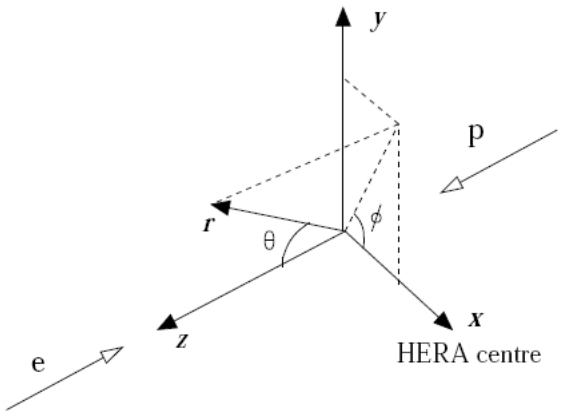

Figure 1.5: *ZEUS coordinate system.*

A brief outline of the various detector components is given below and a more detailed description of the sub detectors relevant to the present analysis will be given later in this chapter. The two projection views of the detector in the (Z,Y) and (X,Y) planes (Fig. 1.6 and 1.7) help to understand how the different components were placed in the different angular regions.

At the center of ZEUS, surrounding the beam pipe, lied the inner charged particle tracking detector. The main tracking device was the CTD (Central Tracking Detector) placed in a solenoidal magnetic field ($B = 1.43\,\mathrm{T}$) generated by a thin superconducting solenoid. In 2001, a silicon-strip Micro Vertex Detector (MVD), replaced the Vertex Detector (VXD) which was part of the initial configuration and removed during the 1995-1996 shutdown. The MVD

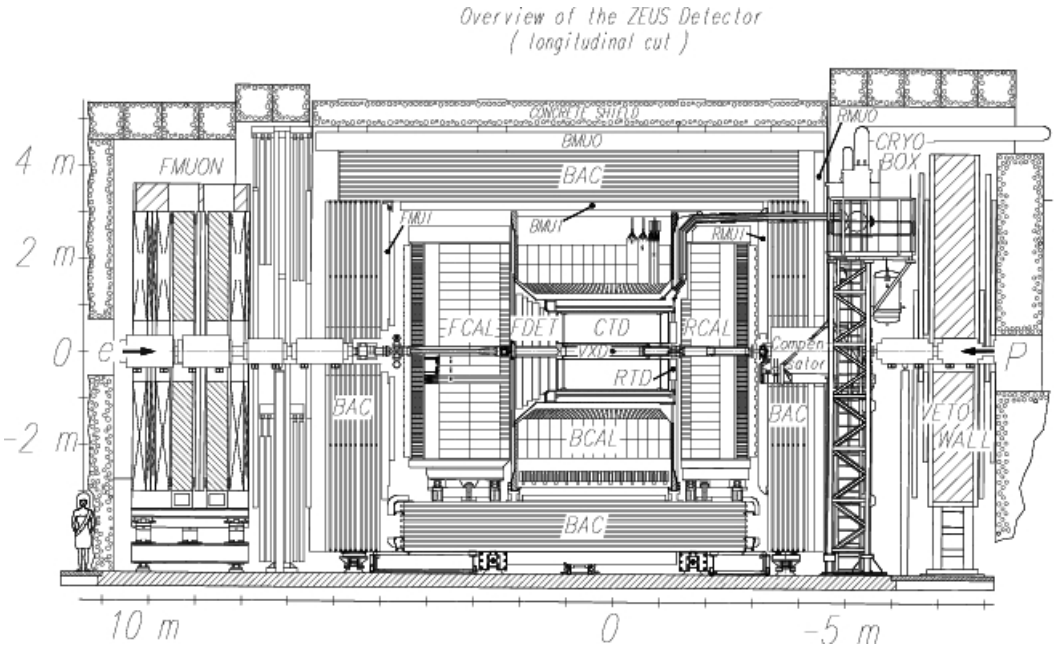

Figure 1.6: *ZEUS longitudinal section (Z, Y).*

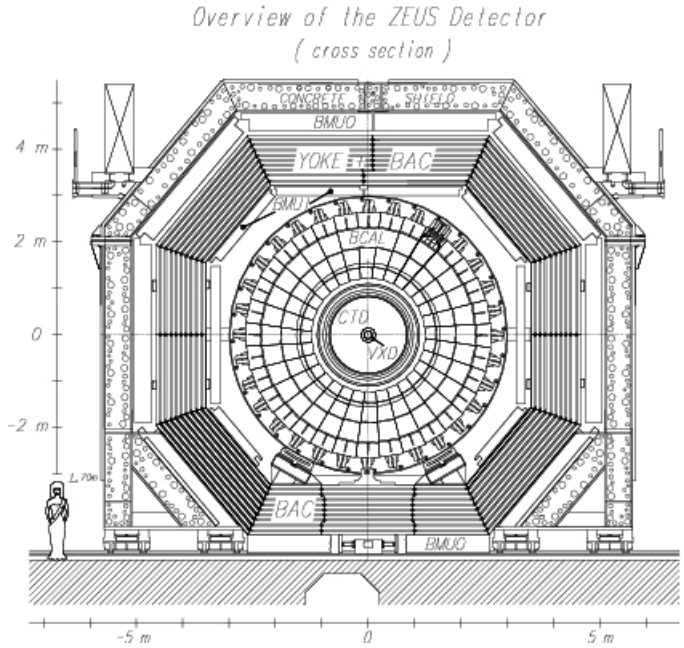

Figure 1.7: *ZEUS transversal section (X, Y).*

was installed inside the CTD nearest to the interaction point. The CTD was supplemented in the forward direction by three sets of planar drift chambers (FTD) with interleaved Transition Radiation Detectors (TRD), labelled FDET in Fig. 1.8.

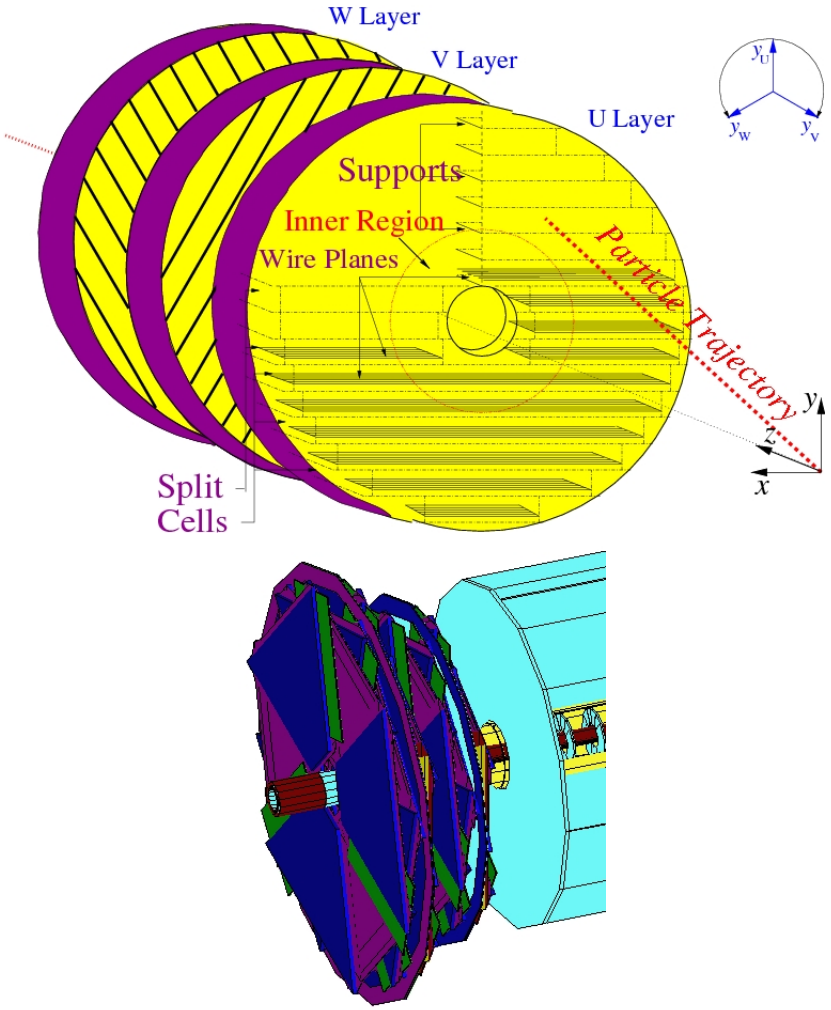

Figure 1.8: *Planar drift chambers (up) and straw tubes (down) which constitued the FDET.*

The rear direction was supplemented by one planar drift chamber consisting of three layers (RTD). Although technically part of the calorimeter,

the Small Rear Tracking Detector (SRTD) provided improved position resolution for particles and was particularly useful for the identification of the scattered lepton in the rear direction not intercepted by the rear part of the calorimeter. Together, the tracking detectors offered an angular acceptance of $10^\circ < \theta < 160^\circ$ for charged particles. The tracking system was surrounded by a compensating high resolution uranium-scintillator sampling calorimeter (UCAL, see Section 1.6) which was used as the main device for energy measurements. It was divided into three sections: the Forward (FCAL), Barrel (BCAL) and Rear (RCAL) calorimeters. The iron yoke, which provided the return path for the solenoidal magnetic field flux, was equipped with a set of proportional tubes and served as a calorimeter (BAC) for the detection of shower tails not completely "contained" by UCAL. This device acted also as a tracking device for muon detection. Dedicated muon detectors (see Section 1.7) were located inside (FMUI, BMUI and RMUI) and outside (FMUO, BMUO and RMUO) the iron yoke. For the inner muon chambers, the iron of the yoke was magnetized with a toroidal field (with strength $B \simeq 1.7\,\mathrm{T}$) in order to analyse the muon momentum. For the forward muon detector the average field inside the toroids was $\sim 1.7\,\mathrm{T}$. Other detectors were located several meters away from the main detector along the beam pipe. The VETO wall was located in the rear direction about $z = -7.5\,\mathrm{m}$ from the IP. It consisted of an iron wall supporting scintillator hodoscopes and was used to reject background from beam-gas interactions. The LUMI detector (see Section 1.8) was made of two small lead-scintillators calorimeters at $z = -35\,\mathrm{m}$ and $z = -104$, $z = -107\,\mathrm{m}$ and detected electrons and photons from bremmstrahlung events for the luminosity measurement. The 6 m Tagger was a small scintillating fiber/tungsten calorimeter located close to the beam line at $z = -5.37\,\mathrm{m}$. Its prime purpose was to tag quasi-real electrons

from photoproduction events and to assist the acceptance determination for the lumi system. During the last period, the tagger has received a lot of attention because of its role in the measurement of F_L and the total photoproduction cross section.

1.3 The Central Tracking Detector (CTD)

The Central Tracking Detector (CTD) [9] was a cylindrical wire drift chamber used for measuring the direction and momentum of the charged particles and to estimate the energy loss dE/dx which provided information for particle identification.

The inner radius of the chamber was 18.2 cm, the outer was 79.4 cm and its active region covered the longitudinal interval from $z = -100$ cm and $z = 104$ cm, resulting in a polar angle coverage of $15° < \theta < 164°$. The chamber was fluxed, close to the atmosferic pressure, with a gas mixture of argon (Ar), carbon dioxide (CO_2) and ethane (C_2H_6) in the proportion 90:80:2. An alcohol/H_2O mixture (77/23 %) was injected into the gas. The sense wires were 30 μm thick while the field wires had different diameters. A total of 4608 sense wires and 19854 field wires were contained in the CTD. The 4608 sense wires were organized in 9 superlayers, each constisting of 8 wire layers, see Fig. 1.9. A group of eight radial sense wires with associated field wires in one superlayer made up a *cell*. The wires in superlayers 1, 3, 5, 7 and 9 ran parallel to the beam direction (axial layers), numbered from the innermost to the outermost, while wires in even-numbered (stereo) SLs were at a small stereo angle of $\pm 5°$ to measure the z coordinate. The CTD was designed to operate in a magnetic field to allow the momentum measurement of charged particles. The field wires were tilted at 45° with respect to the radial direction, in order

to obtain a radial drift under the influence of the electric and magnetic field. An octant of the CTD is shown in Fig. 1.9. The achieved resolution is

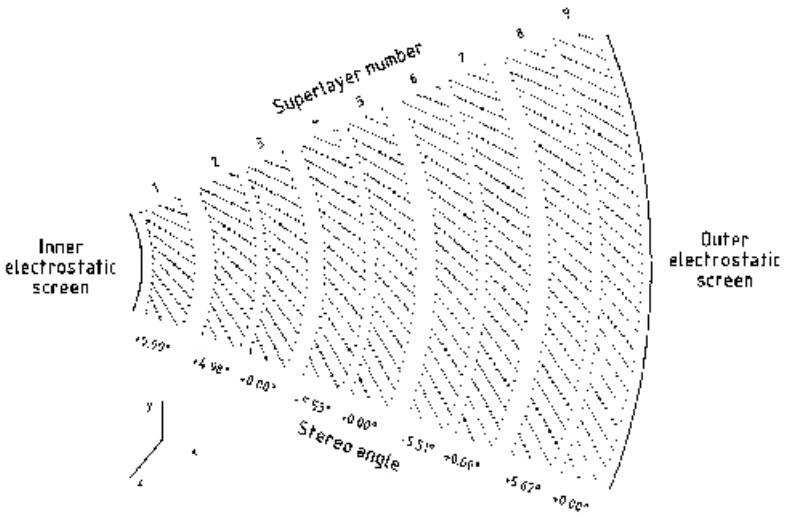

Figure 1.9: *Transverse cross section of one octant of the CTD.*

$\sim 100 - 120\,\mu$m in the $r - \phi$ plane and 1.4 mm in the z coordinate. A charged particle traversing the CTD produced ionization of the gas in the chamber. Electrons from the ionization drifted towards the positive sense wires, while the positive ions were repelled and drifted towards the negative field wires. The drift velocity of the electrons was approximately constant and equal to $50\,\mu$m/ ns. An avalanche effect occurred close to the wire giving an amplification factor on the electrons of $\sim 10^4$ so that a measurable pulse was induced on the sense wires. The three inner axial superlayers (SL1, SL3, SL5) were additionally instrumented with the z-by-timing system. This estimated the z-position of a hit by measuring the difference in arrival time of the pulses on the sense wires at each end of the detector. Although the resolution achieved (~ 3 cm) was much cruder than that obtained using the full axial and stereo wire information, it was a relatively fast method and

used predominantly for trigger and track seed-finding. As mentioned before, the CTD was contained within a superconducting solenoid which provided a magnetic field of 1.43 T. This field caused charged particles to travel in a circular path of radius, R, given by:

$$R = P_T/QB(S.I.units) \tag{1.2}$$

where Q was the charge of the particle (Coulomb), B the strength of the magnetic field (Tesla) and P_T was the transverse momentum ($\mathrm{kg}\cdot\mathrm{m}\cdot\mathrm{sec}^{-1}$). This allowed an accurate determination of the P_T of the charged particle. Since the installation of the MVD in 2001, the resolution has changed. It was expected that the influence from multiple scattering was larger (more material between CTD and the IP) but that the hit resolution was better compared to the resolution quoted above (due to the inclusion of MVD hits). Latest results including the MVD in the global track reconstruction indicated that the momentum resolution for tracks traversing 9 CTD SLs is [10]:

$$\sigma(P_T)/P_T = 0.0026P_T \oplus 0.0104 \oplus 0.0019/P_T \tag{1.3}$$

1.4 The ZEUS Micro Vertex Detector (MVD)

During the 2000-2001 shutdown, planned for the luminosity upgrade, a silicon microvertex detector (MVD) was installed in ZEUS. The MVD, placed between the beam pipe and the inner volume of the CTD, provided an improvement in the global precision of the tracking system and allowed the identification of events with secondary vertices originating from the decay of particles with long lifetime ($c\tau \gtrsim 100\,\mu\mathrm{m}$). This device helped the study of hadron decays containing heavy quarks such as charm and beauty, or tau leptons thanks to an improvement in the track resolution with the possibility

to resolve secondary vertices. The technical requirements which were taken into account during the design of the MVD were:

- angular coverage around the IP between $10^\circ < \theta < 160^\circ$;
- measurement of three points for each track in two independent projections;
- 20 μm intrisic hit resolution;
- separation of two tracks up to 200 μm.

The main limitations were due to the small amount of space available between the CTD (radius=18.2 cm, see Section 1.4) and the beam pipe. The following description summarizes the main characteristics of the MVD in its two components covering the central (BMVD) and forward (FMVD) region (see Fig. 1.10).

1.4.1 Barrel and forward micro vertex detector

The barrel section of the MVD was 64 cm long, see Fig. 1.10, and was substructured in three layers to allow high efficiency in the pattern recognition and to make an estimate of the track momentum in the trigger phase. The first layer of silicon detectors follows the elliptical path around and along the beam pipe and was placed at a variable radius between 3 and 5 cm from the CTD axis (see Fig. 1.11).

The beam pipe was not centred with respect to the CTD axis and the nominal interaction point was shifted towards the centre of HERA (along the x axis) by about 4 mm in order to accommodate the primary synchrotron radiation spread inside the beam pipe volume. The second and third layer were placed along a circular path at $r \sim 8.6\,\text{cm}$ and $r \sim 12.3\,\text{cm}$. On average

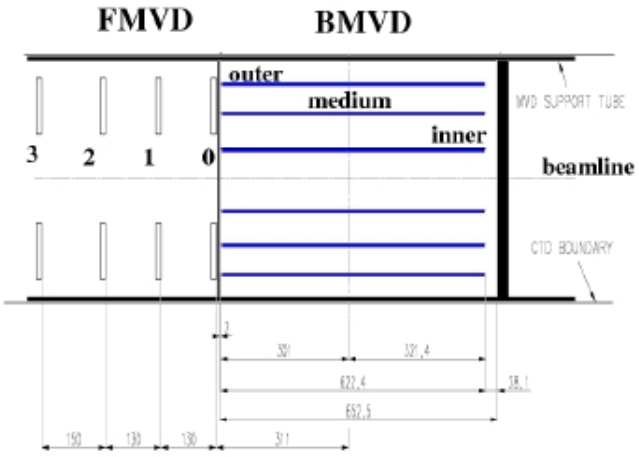

Figure 1.10: *Longitudinal MVD section. There were three layers in the barrel region and four wheels in the forward region.*

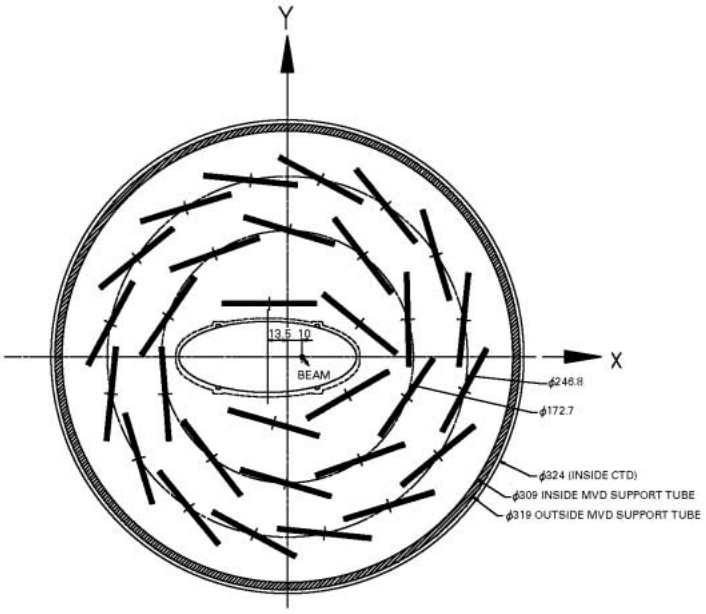

Figure 1.11: *BMVD section. Three superlayers around beampipe are shown.*

a track crosses 2.8 layers. The resolution on the impact parameter, based on Monte Carlo studies, was $\sim 100\,\mu m$. It was defined for tracks perpendicular to the beam pipe ($\eta = 0$) which crossed all three layers and was a function of track momentum. The BMVD was equipped with 600 silicon strips sensors mounted on 30 carbon fibre structures called *ladders* (Fig. 1.12);

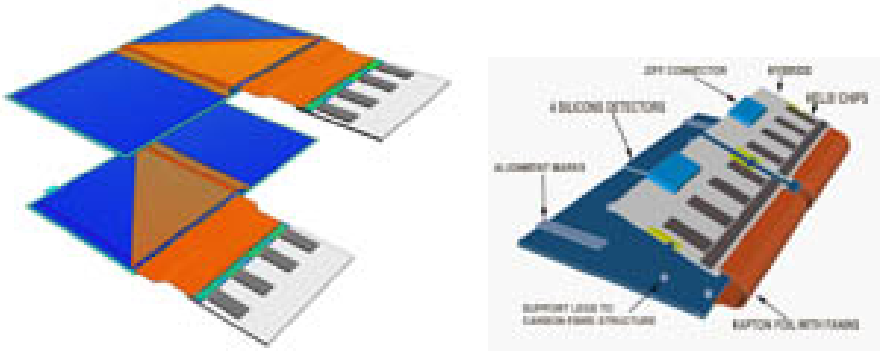

(a) *Half modules* (b) *Ladders*

Figure 1.12: *Half modules and ladders.*

two layers of sensors were placed parallel and perpendicular to the beam line in order to measure $r - \phi$ and $r - z$ coordinates. Each layer was made of two single-sided silicon strip planes ($320\,\mu m$ thickness) with p^+ strips implanted in a n-type bulk. The strip pitch was $20\,\mu m$; every 6^{th} strip had an AC coupling with a read out line made by an aluminium strip through a dielectric material ($SiO_2 - SiN_4$). Two sensors were glued together, electrically connected with a copper path excavated in a Upilex foil of $50\,\mu m$ of thickness (see Fig. 1.12). From the figure it can be seen that the sensor was connected to the readout device; the resulting surface covered by the two sensors and by the readout system was called a "half-module" and was $6.15\,cm \times 6.15\,cm$.

The FMVD consisted of 4 planes called *wheels*; each of them was made of two layers of 14 silicon sensors with the same technical characteristics of

the barrel sensors but with a trapezoidal shape (Fig. 1.13).

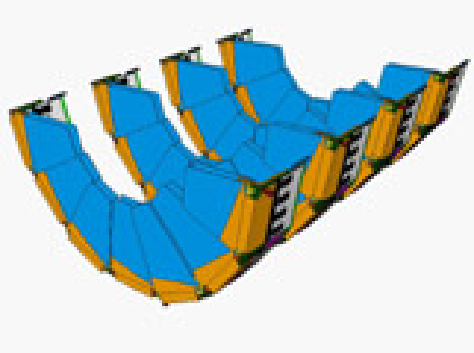

Figure 1.13: *FMVD four wheels.*

This device allowed to extend the acceptance in pseudorapidity up to $\eta = 2.6$, a region where tracking information had yet to be used in ZEUS. Each wheel had inner and outer sensors. They were mounted back to back. An inner and outer wheel sensor formed a sector. The crossing angle between the strips in the inner and outer sensor was $\sim 13°(180°/14)$. Inside a layer of sensors the adjacent sensors were slightly overlapped in order to minimize the dead regions. The four wheels were positioned at $z = 32, 45, 47$ and 75 cm ; the first wheel was linked to the structure supporting the BMVD. A more detailed description can be found in [11].

1.5 The Uranium-scintillator Calorimeter (UCAL)

The ZEUS calorimeter (UCAL) [12] was a high-resolution compensating calorimeter. It completely surrounded the tracking devices and the solenoid, and covered 99.7% of the 4π solid angle. It consisted of 3.3 mm thick depleted uranium plates ($98.1\%U^{238}, 1.7\%Nb, 0.2\%U^{235}$) as absorbers alternated with 2.6 mm thick organics scintillators (SCSN-38polystyrene) as active material, see Fig. 1.14.

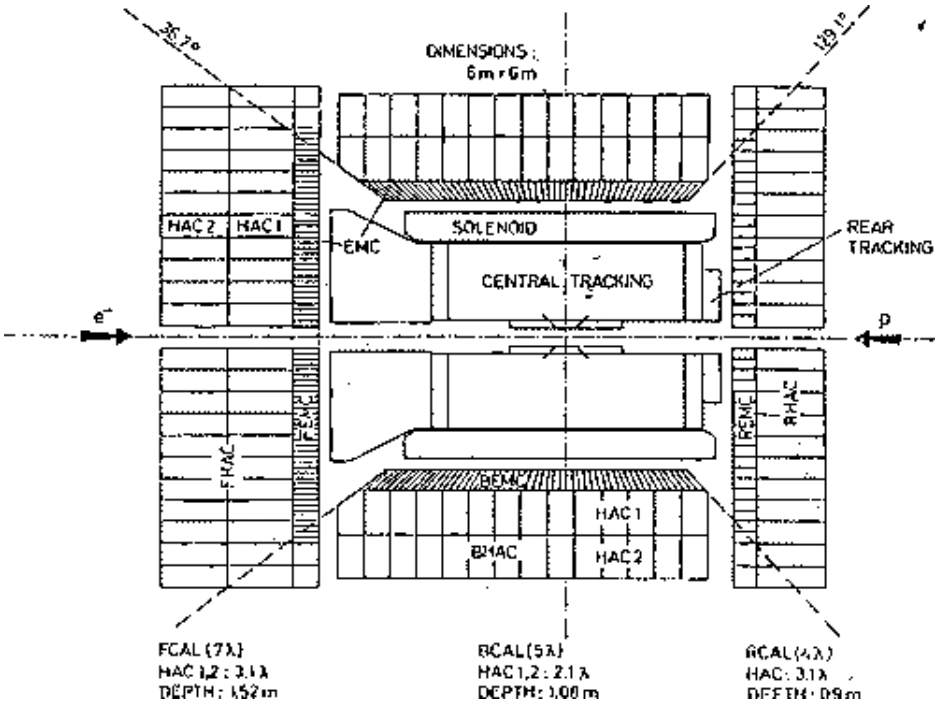

Figure 1.14: *UCAL sections.*

The hadronic showers contained both hadronic and electromagnetic components whose proportions could fluctuate enormously. In order to take into account this phenomenon and therefore optimize the energy detection of both shower components, the uranium calorimeter was designed to be compensating, so as to obtain the same mean detector response from hadronic and electromagnetic showers of the same energy ($e/h = 1$). Therefore the UCAL had different layers of depleted uranium and scintillator with thickness of 3.3 mm and 2.6 mm. Under test beam conditions [13], the electromagnetic energy resolution achieved was:

$$\frac{\sigma_E}{E} = \frac{18\%}{\sqrt{E}} \oplus 2\% \tag{1.4}$$

whilst the hadronic resolution was:

$$\frac{\sigma_E}{E} = \frac{35\%}{\sqrt{E}} \oplus 1\% \tag{1.5}$$

where E was the particle energy measured in GeV. The UCAL was divided into three regions: the forward (FCAL), barrel (BCAL) and rear (RCAL) calorimeter. Since most of the final state particles in a lepton-proton interaction at HERA were boosted to the forward (proton) direction, the three parts were of different thickness, the thickest being the FCAL ($\sim 7\lambda$), then the BCAL ($\sim 5\lambda$) and finally the RCAL ($\sim 4\lambda$), where λ was the interaction length. Each part of the calorimeter was divided into modules. The 23 FCAL modules and the 23 RCAL modules were rectangular, see Fig. 1.15, whereas the 32 BCAL modules which surrounded the cylindrical CTD were

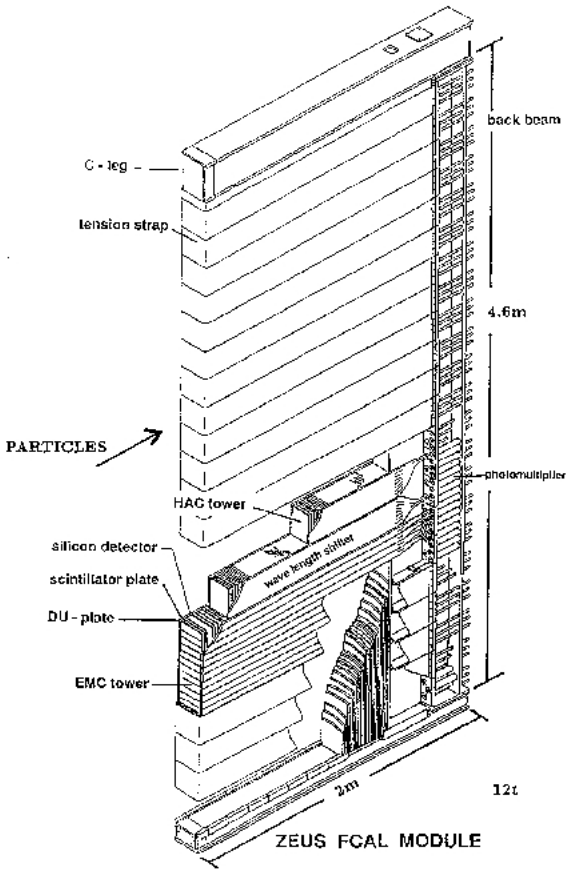

Figure 1.15: *FCAL module.*

wedge-shaped covering 11.25° in azimuth, see Fig. 1.16.

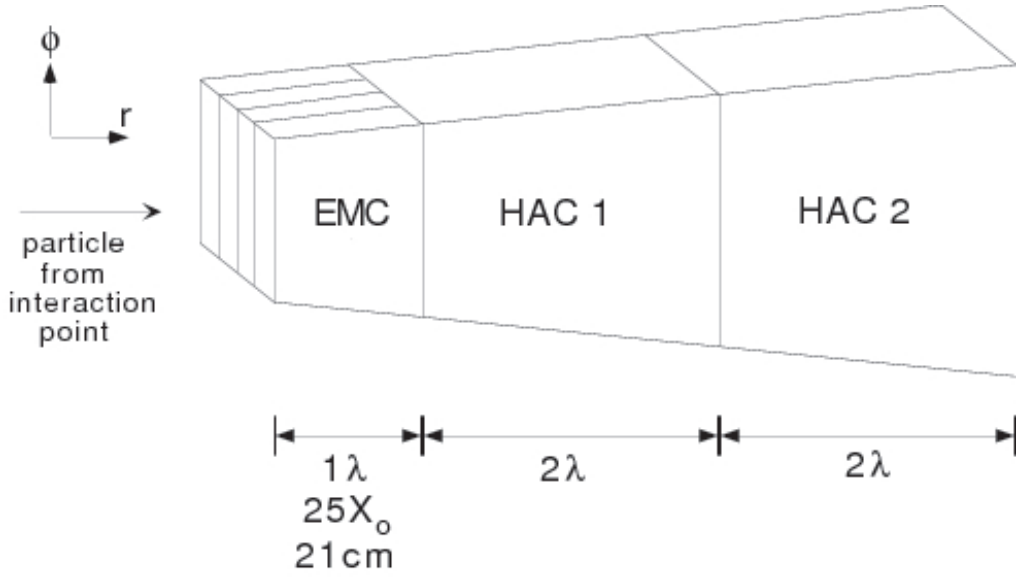

Figure 1.16: *BCAL module.*

Each module consisted of so called *towers* of $20 \times 20\,\mathrm{cm}^2$ which were subdivided longitudinally into one electromagnetic (EMC) and two (one in RCAL) hadronic (HAC) sections. The EMC sections were further transversely divided into four cells (only two in RCAL). The FCAL EMC section per tower consisted of the first 25 uranium-scintillator layers and had a depth of $25X_0$, where X_0 was the radiation length. Each of the two HAC sections per FCAL tower was 3.1λ deep and consisted of 160 uranium-scintillator layers. The BCAL EMC section was made of the first 21 uranium-scintillator layers, the two HAC sections of 98 layers. The resulting depth was $21X_0$ for the electromagnetic section and 2.0λ for each hadronic section. The RCAL towers consisted of one EMC and only one HAC section. Therefore its depth was $26X_0$ for the EMC part and 3.1λ for the HAC part. Light produced in the scintillators was read out by 2 mm thick wavelength shifter (WLS) bars at both sides of the module, and brought to one of the 11386 photomultiplier

tubes (PMT) where it was converted into an electrical signal. The summed information per cell was used for energy and time measurements. The UCAL provided accurate timing information, with a resolution of the order of 1 ns for particles with an energy deposit greater than 1GeV. This information could be used to determine the timing of the particle with respect to the bunch-crossing time, and it was very useful for trigger purposes in order to reject background events, as will be illustrated later in the trigger section. Calibration of the PMTs and the electronics was mainly performed using the natural radioactivity of the depleted uranium which produced a constant signal in the PMTs. The signal could be used to intercalibrate geometrically identical regions and to transport the absolute calibration scale determined in test beam measurement. In addition, laser, LED and test pulses were also used for the calibration. The achieved uniformity of calibration was better than 1%. The Presampler [14] was a thin scintillator layer placed on the inner side of the forward and rear calorimeter (FCAL and RCAL) and was used to cover the forward and rear regions which could not be covered by the barrel section. It was used to estimate the shower dimensions and hence the energy loss in the passive material before entering the calorimeter.

1.6 The Muon Detectors

These detectors were specifically designed to measure penetrating tracks coming from the interaction region (pointing tracks) which could cross the whole calorimeter and the iron yoke. These tracks were identified mainly with muons which can traverse large amounts of material without being absorbed. The momenta of muons can be very different, depending on their polar angle due to the boost in the forward direction. Muons with more than 10GeV

momentum were frequently produced in the forward region. In the barrel and rear regions, the average momentum of the muons was expected to be much lower. Therefore the muon detection system was split into two sub-detectors, the Forward Muon Detector (FMUON) and the barrel and rear muon detectors (BMUON and RMUON respectively).

1.6.1 The Forward MUON detector (FMUON)

The muon detection in the forward region was important for HERA because important physical phemomena, like heavy quarks or leptoquarks production, produced leptons with small decay angles. Since the resolution and the acceptance of tracking detectors placed inside the calorimeter decreased at low angles, the FMUON was used to measure momenta up to 100 GeV with a resolution of 25% in the forward region independently of the inner region detectors. This detector was equipped with a trigger system which applied a momentum cut and required a candidate track originating from the interaction point.

The FMUON consisted of:

- a system of four limited streamer tube trigger planes (LT1-LT4) [15], with digital ρ[5] and ϕ readout;
- two planes of limited streamer tubes with digital (ρ, ϕ) and analog ρ readout, in the large polar angle region (LW1 and LW2);
- four planes of drift chambers (DC1-DC4) for the measurement of pseudo ρ [16];
- two large toroidal iron magnets providing a magnetic field of 1.7 T

[5]The ρ coordinate defined the direction perpendicular to the beam line.

for the momentum separation and measurement in the angular region $5° < \theta < 16°$.

The first limited streamer tube plane and the first drift chamber made up the FMUI detector, while the FMUO detector consisted of the rest of the system, see Fig. 1.17.

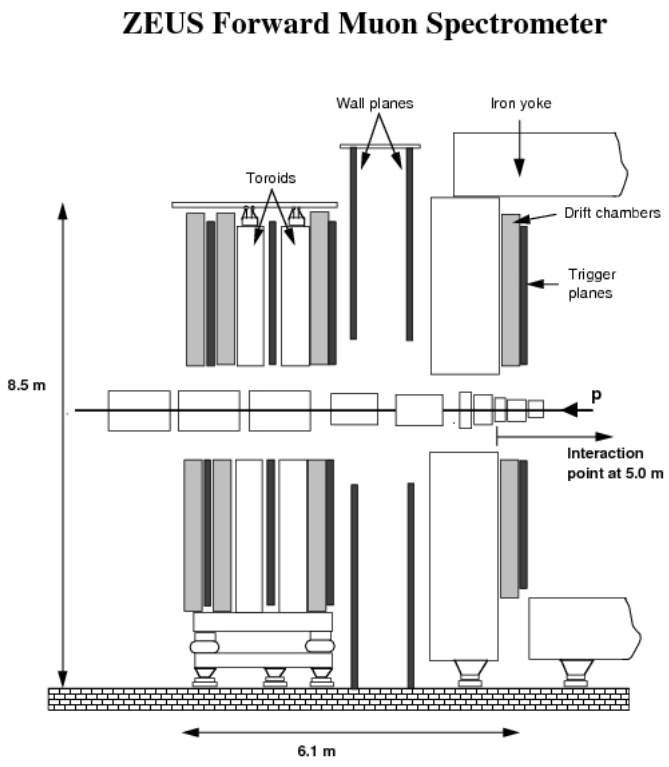

Figure 1.17: *FMUON longitudinal section.*

The Limited Streamer Tubes (LST) Planes The aim of the limited streamer tubes (LST) was to trigger on muon candidates and to reconstruct their position in terms of the azimuthal and radial coordinates of the track. A trigger plane was made of four LST chambers, grouped in pairs in two half-planes. A quadrant consisted of two layers of LST positioned horizontally inside a plastic sheet. The tubes of the two planes were slightly displaced (0.5 cm) in order to achieve a complete geometrical acceptance. Each quadrant was contained in an aluminium air tight box. On the outer side, copper strips were glued in polar geometry. The LSTs induced a signal in the copper strips if a particle crossed the plane. There were 132 radial ρ strips each 1.9 cm wide. They were divided along the bisector of the quadrant so that the simplest unit of the trigger plane to be read out was the octant. The number of ϕ strips was 32 per octant and each strip covered an interval of 1.4° in the azimuthal angle.

The Drift Chambers (DC) The drift chambers allowed to reach a spatial resolution in pseudo-ρ of $\sim 300\,\mu$m. Each plane consisted of 8 chambers, grouped in two half planes, fixed on a support panel. The basic constituent of the chamber was the cell, made of four sense wires and of the layers needed to generate the appropriate electric field. The signals of the four sense wires were sent to a TDC, which converted them into a time distance, connected to the space distance by a known relation.

The Large Angle Coverage Planes (Limited Streamer Wall, LW) The two large angle coverage planes (LW) were needed in order to achieve the desired geometrical acceptance also in the region left uncovered by the

toroids ($16^\circ < \theta < 32^\circ$). They were also useful for trigger purposes in combination with the first LST planes. Each plane consisted of eight steel tight wrappings that contained a LST layer. The LST signal was induced on copper strips with a radial geometry, spaced at 0.7° in the ϕ coordinate and at 1.8 cm in the ρ coordinate. There were 64 ϕ strips per octant and 192 ρ strips per octant. The achieved resolution in the ρ coordinate, using a charge barycenter method, was ~ 1 mm.

1.6.2 The Barrel and Rear MUON detector (B/RMUON)

The barrel and rear muon detector [17] covered a very large area ($\sim 2000\,\mathrm{m}^2$) and consisted of LST chambers as the basic structure. The chambers covering the inner barrel part between the CAL and the iron yoke were called BMUI while the chambers situated outside the yoke were denoted as BMUON. The rear region was divided into RMUI and RMUO chambers in a similar way (see Fig. 1.18). The chambers had different shapes and dimensions depending on their location, but their nominal structure was the same. The supporting structure of each chamber was an aluminium honeycomb frame 20 cm thick in the rear chambers and 40 cm in the barrel. Two plates of LST were placed on both sides of the honeycomb. The two layers on the same side of the chamber were displaced by 8.3 mm in order to minimize dead areas for particles traversing at 90° with respect to the wire plane. Each LST was made of a plastic sheet with eight cells. Each cell contained a copper-beryllium wire of 100 μm diameter, the distance between two sense wires being 1 cm. Each LST plane was equipped on one side by 13 mm wide readout strips with 15 mm pitch that ran orthogonal to the wires. In the BMUI and BMUO chambers the LSTs were parallel to the beam direction while in RMUI and RMUO they were horizontal (parallel to the x-axis). With the analog strip

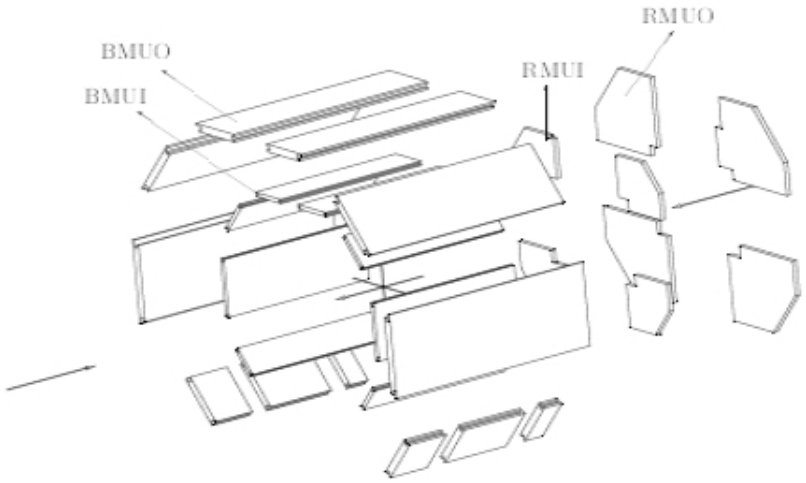

Figure 1.18: *Layout of the barrel and rear muon detector.*

readout the achievable spatial resolution on the coordinate orthogonal to the wires was 200 μm while it was 700 μm for the coordinate parallel to the wires.

1.7 The Backing Calorimeter (BAC)

The Backing Calorimeter (BAC) [18] used the return iron yoke as an absorber to form an additional tracking calorimeter using aluminium proportional tubes operating in an $Ar - CO_2$ atmosphere. The BAC measured showers leaking out of the CAL allowing the selection of event samples with a resolution corresponding to the intrinsic resolution of the CAL. It could distinguish between hadron showers and muons and provided muon identification and trigger capabilities in the bottom yoke and other areas where no muon chambers were present. The BAC was built from modules inserted into the yoke (see Fig. 1.6) consisting of 7-8 proportional tubes of a cross section of 11×15 mm and a length between 1.8 and 7.3 m. Modules were

equipped with 50 cm long aluminium cathode square pads in addition to the gold plated tungsten wires of 50 µm diameter. The wires were parallel to z in barrel (providing ϕ) and parallel to x in Forward/Rear zone (providing y). The wires were read out on one side and provided both analogue and digital signals whereas the pads had only an analogue read-out.

Energy was measured by summing up the analogue signals in towers of a width of 25-50 cm (2-4 modules) over the full depth of the BAC. The pads of 2-4 neighbouring modules were added up to pad towers with an area of $50 \times 50\,\mathrm{cm}^2$ (4 modules) similar to the wire towers. They provided also patterns of hit positions in the BAC to reconstruct muon trajectories. The spatial resolution of the BAC was $\sim 1\,\mathrm{mm}$ perpendicular to the wires, whereas the resolution parallel to the wires was defined mainly by the pad size. The energy resolution determined by test beam measurements was:

$$\frac{\sigma_E}{E} = \frac{1.1}{\sqrt{E}} \tag{1.6}$$

where E was the particle energy in GeV.

1.8 The luminosity measurement

The luminosity measurement at ZEUS was done by studying the production rate of photons through the Bethe-Heitler process:

$$e + p \rightarrow e' + p + \gamma \tag{1.7}$$

where the photon was emitted from the electron at very small angles with respect to the ingoing lepton direction (negative z). The cross section for this process at the leading order (LO) was expressed as:

$$\frac{d\sigma}{dk} = 4\alpha_e r_e^2 \frac{E'}{kE}\Big(\frac{E}{E'} + \frac{E'}{E} - \frac{2}{3}\Big)\Big(ln\frac{4E_pEE'}{Mmk} - \frac{1}{2}\Big) \tag{1.8}$$

where E and E_p were the energies of the lepton and proton beams respectively, E' was the outgoing electron energy, k was the photon energy, M and m were the proton and electron masses, α_e the electromagnetic coupling and r_e^2 represents the classical electron radius. Higher-order corrections in the above cross section calculation were less that 0.5%.

The luminosity monitor consisted of a photon and a lepton calorimeter, located along the beam pipe at $z = -(104 - 107)$ m and $z = -35$ m, respectively (Fig. 1.19).

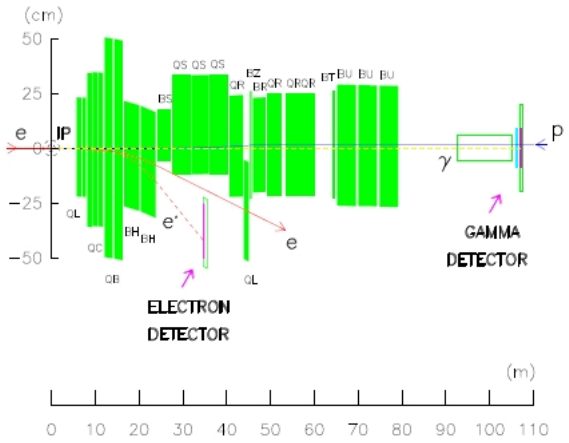

Figure 1.19: *The layout of the ZEUS Luminosity Monitor. The nominal interaction point was located at (0,0)*

To protect the photon calorimeter against synchrotron radiation, it was shielded by a carbon-lead filter. The resulting calorimeter resolution, (with E in GeV), was:

$$\frac{\sigma_E}{E} = \frac{0.25}{\sqrt{E}} \tag{1.9}$$

The bremsstrahlung event rate was determined by counting the number of

photons above a fixed energy threshold, E_γ^{th}, and not by the simultaneous identification of the lepton and the photon, because of the dependence of the lepton calorimeter acceptance on the beam position and angle. The luminosity was then extracted using:

$$L = \frac{R_{ep}(E_\gamma > E_\gamma^{th})}{\sigma_{ep}^{acc}(E_\gamma > E_\gamma^{th})} \tag{1.10}$$

where $\sigma_{ep}^{acc}(E_\gamma > E_\gamma^{th})$ is the cross section corrected for the detector acceptance, $R_{ep}(E_\gamma > E_\gamma^{th})$ is the photon rate.

1.9 Background

The background event rate at ZEUS could be much higher than the ep interaction rate, depending on the beam-pipe vacuum conditions. The main background sources which had to be removed were:

- Interactions inside the beam pipe: beam particles interact with the residual gas inside the beam pipe or off-momentum beam particles interact a gainst the beam pipe walls. If this interaction happens near the detector, the interaction products can be detected by ZEUS.

- Halo muons: the hadronic interactions of the beam protons with the residual beam pipe gas can subsequently produce muons through pion or kaon decays; these muons go into the halo beam and were therefore called *halo muons*.

- Cosmic muons: these were muons coming from the cosmic showers generated in the atmosphere which can be detected by ZEUS.

The background was dramatically reduced by the trigger, which was tuned to discriminate against it. The background coming from the interaction of the

particles with the beam gas was limited through the VETOWALL device, an iron wall 87 cm thick and $800 \times 907\,\mathrm{cm}^2$ placed at $z = -7.5\,\mathrm{m}$ from the interaction point. It was instrumented with two scintillator hodoscopes, one for each side of the wall, which can identify the beam-gas interaction events. A $95 \times 95\,\mathrm{cm}^2$ gap window was left uncovered around the beam-pipe. The trigger system, described in the next chapter, takes into account the information coming from the calorimeter, SRTD (a hodoscopic scintillator placed around the beam pipe in front of the RCAL), C5 (a HERA collimator equipped with scintillator counters placed behind the RCAL at 1.2 m from the nominal interaction point in the electron beam direction), CTD and muon detectors.

The timing difference between the FCAL and RCAL measurements can be used to reject the beam gas events, since the products from the beam gas interactions hit the RCAL $\sim 10\,\mathrm{ns}$ before hitting the FCAL. The calorimeter temporal resolution, for energy E greater than few GeV, was better than 1 ns. The same method was used to tag the cosmic muons, studying the temporal difference between the upper and lower side of BCAL.

1.10 The ZEUS trigger system

The bunch crossing frequency at ZEUS was $\sim 10\,\mathrm{MHz}$, corresponding to a timegap of 96 ns between two consecutive bunches. The rate was dominated by the interaction of the proton beam with the residual gas which contributed about $10 - 100\,\mathrm{kHz}$, depending upon the vacuum levels in the beam-pipe up to 100 m upstream of ZEUS. This frequency had to be reduced to a level compatible with the offline data storage without loosing interesting physics events (few Hz). The approach adopted for the ZEUS data acquisition was a

three level trigger system with increasing complexity of the decision making algorithm and decreasing throughput rate (Fig. 1.20).

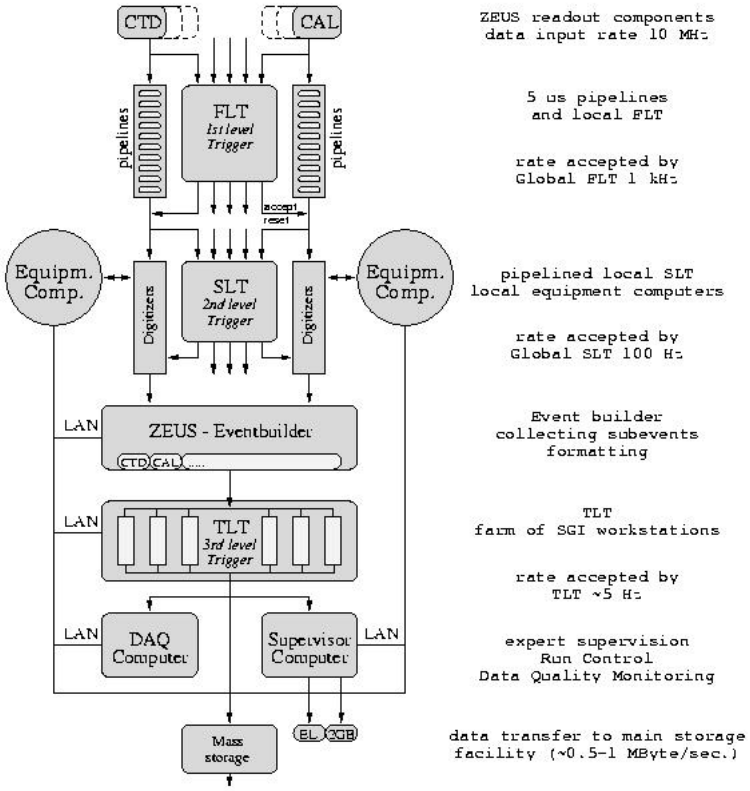

Figure 1.20: *The trigger chain*

- *First level trigger (FLT)*; was a hardware based trigger which used programmable logic to make a quick rejection of background events. The FLT reduced the input rate of 100 kHz to an output rate of ~ 300 Hz. As it was not possible to take a decision within the bunch crossing time, the data were pipelined until the trigger decision was taken. Individual component decisions used a subset of the total data, and were made within $1.0 - 2.5\,\mu$s. The global first level trigger (GFLT) combined informations from the different subdetectors and took abort/accept deci-

sion after 4.4 μs. Typical criteria used by the FLT in taking the trigger decision were the approximate "crude" event vertex position and track multiplicities from CTD, the transverse energy of the event and energy sums in sections of the calorimeter, the timing vetoes from CAL, SRTD, C5 and the presence of muons. The FLT had a good efficiency for *ep* physics ($\sim 100\%$), but still had a very low purity ($\sim 1\%$).

- *A second level trigger (SLT)*; the SLT was a parallel processor utilising a network of transputers. It reduced the FLT output rate of ~ 300 Hz to an output rate of $\lesssim 100$ Hz. As in the FLT, the outputs of the component SLT decisions were passed to the global SLT (GSLT) where the event decision was made. The GSLT made its decision after $5.2 - 6.8$ ms. The decision was based upon limited charged particle tracking, vertex determination, calorimeter timing, $E - P_z$ and scattered electron tagging.

  Data from an event accepted by the SLT trigger were sent directly from the component to the event builder (EVB). The EVB stored the data from the components until the third level trigger (TLT) was ready to process it, and combines the data from different components into one consistent record: the event. One event was stored in a single record of the ADAMO [53] database tables.

- *Third level trigger (TLT)*; was a software trigger which was sent asynchronously with the bunch crossing on a dedicated PC farm. At this stage a version of the event reconstruction software was run, including tracks and interaction vertex reconstruction. The TLT has been designed to cope with an input rate of 100 Hz from the SLT at design luminosity. The output rate was reduced to about 5 Hz. After

accepting an event, the TLT sends the data via optical link to the DESY computer centre, where the events were written onto disk to be available for further offline reconstruction and data analysis.

Chapter 2

Theoretical overview

In this chapter the theoretical concepts relevant for the following analysis are described. The Standard Model is briefly introduced with emphasis on the remaining open questions, which motivate searches for phenomena beyond the Standard Model. Lepton nucleon scattering at HERA is described, including all physics processes considered for the following search for isolated leptons. Theories beyond Standard Model are introduced which could produce the signature of interest. Emphasis is given to a generic model describing the production of single top quarks through quark-flavour changing neutral current (FCNC), which is chosen as the signal process in the search for isolated muons and electrons.

2.1 The Standard Model

The Standard Model (SM) of particle physics describes the behaviour of the subatomic world in the framework of renormalizable gauge theories. In the SM, the forces between the fundamental particles (fermions) are mediated by the exchange of (virtual) gauge vector boson which are related to the

gauge symmetries of the field theories. Three basic forces (*interactions*) are contained in the SM: the *electromagnetic*, the *weak* and the *strong*. The group structure of the SM is:

$$SU(3)_C \times SU(2)_L \times U(1)_Y \tag{2.1}$$

where $U(n)$ denotes the group of all unitary $n \times n$ matrices and $SU(n)$ is the group of all unitary $n \times n$ matrices with determinant 1. The weak and electromagnetic interactions (called electroweak interaction) are unified in the gauge group $SU(2)_L \times U(1)_Y$.

The fermions are divided into two groups, the *leptons* and the *quarks* [28] and each group has three *doublets* with two particles each. The doublets of each group differ only by the particle masses, not by interaction (*universality*). For each particle X there exists a corresponding anti-particle $\bar{X}$ with the same mass but oppositely signed quantum numbers. The gravitational force is not incorporated in the SM.

The fundamental gauge bosons and forces described in the SM are listed in Tab. 2.1 and the SM fermions in Tab. 2.2.

Interaction	boson	Q_{EM}	related group
electromagnetic	γ	0	$SU(2)_L \times U(1)_Y$
weak	Z^0	0	$SU(2)_L \times U(1)_Y$
	$W^{\pm}$	1	
strong	8 gluons g	0	$SU(3)_C$

Table 2.1: *The fundamental interactions in the Standard Model. The value of the electromagnetic charge, Q_{EM}, is given in multiples of the elementary charge unit.*

	Generations			Q_{EM}	Interactions el.magn.	weak	strong
Quarks	u	c	t	$+2/3$	yes	yes	yes
	d	s	b	$-1/3$	yes	yes	yes
Leptons	ν_e	ν_μ	ν_τ	0	no	yes	no
	e	μ	τ	-1	yes	yes	no

Table 2.2: *The fundamental fermions in the Standard Model, ordered in three generations. The value of the electromagnetic charge, Q_{EM}, is given in multiples of the elementary charge unit.*

Through a process called spontaneous symmetry breaking, the bosons of the weak interactions ($Z^0, W^\pm$) acquire masses ($M_W = 80.398 \pm 0.025$ GeV, $M_Z = 91.1876 \pm 0.0021$ GeV), whereas the photon remain massless. The electroweak unification can take place at an energy of the order of the weak gauge boson masses.

Quantum chromodynamics (QCD) describes strong interactions as an exact ($SU(3)_C$) gauge symmetry. The charge is called "color". The force carriers of the color interactions are the massless gluons, forming a color octet. Three colors can be assigned to each quark, making it a fundamental triplet representation of $SU(3)_C$. Quarks are confined in colorless packages of two (mesons) or three (baryons). Any single quark or gluon in the final state of an elementary reaction ends up in a jet of colorless particles.

Leptons do not carry color charge and are hence singlet representation of $SU(3)_C$. All quarks and leptons are subject to the weak force. The electrically charged fermions partecipate in the electromagnetic interactions, described by the theory of quantum electrodynamics (QED).

The SM has been probed down to length scale of 10^{-18} m. No deviations from the predictions have been found so far. There are however many open questions and problems, some of which are listed below:

- *Higgs boson*: the massive scalar Higgs boson has been introduced in the SM to explain the generation of particle masses. Gauge bosons and fermions are assumed to obtain their masses through interactions with the Higgs field. So far the Higgs boson has not been observed. The LEP II data collected by four experiments (Aleph, Delphi, L3 and Opal) excluded a SM Higgs up to Higgs masses of $M_H = 114$ GeV.

- *Lepton-quark simmetry:* the quark and letpon sectors exhibit a striking simmetry which is not explained by the SM.

- *Fine tuning problem*: radiative corrections to the Higgs boson masses have quadratic divergences. At large scales, the corrections to the Higgs mass are many orders of magnitude larger than the Higgs mass itself.

- *Particle masses*: the particle masses are not explained in the SM. Their spread over many order of magnitude is puzzling.

- *Generation problem*: the existence of three families of quarks and leptons is not explained by the SM.

- *Gravity*: the SM does not include the gravitational force and it is not understood why the strength of gravity is 36 orders of magnitude weaker than that of the electromagnetic force.

It is widely believed that the SM is only a low energy approximation of an overlying more complete theory. Extensions to the SM have been proposed, such as Grand Unified Theories (GUTs), string theories or Supersimmetry

(SUSY). Any search for deviations from the SM is hence also a search for an indication of a more general theory.

2.2 Lepton-nucleon scattering at HERA

Scattering experiments have been a rich source of information for understanding structure of matter in the past decades. Scattering leptons on hadrons is a very appropriate method to study the structure of the hadron, since the pointlike lepton acts as a probe. A seminal experiment of this kind was performed at the Stanford Linear Accelerator Center (SLAC) in 1967 [29], with an electron beam of 20GeV colliding on a nucleon target. It was observed that the structure function, which describes the internal structure of the hadron, depends only on an adimensional variable x, introduced by Bjorken [30]. This behaviour, known as scaling, agrees with the expectation for electrons scattering off free pointlike objects within the nucleon. Influenced by the SLAC measurement and motivated by the assumption of Gell-Mann [31] and Zweig [32] that hadrons could be described as combinations of more fundamental objects, the quarks, Feynman proposed the quark-parton model (QPM) [33]. In this model the hadrons are built by elementary pointlike electrically charged objects (partons). By varying the resolution with which the hadron is inspected in a DIS experiment, one observes the same pointlike sub-structure, a phenomenon that explains the scaling.

In the QPM (quark parton model), DIS is described as the incoherent sum of elastic processes of the lepton off electrically charged point-like constituents (*partons*) of the proton. Subsequent experiments with higher lepton beam energy has shown a breaking of scale invariance, confirming the prediction of the parton density evolution equations as obtained by the Quantum

Chromodynamics (QCD), the theory of strong interaction.

At the HERA electron-proton collider, the structure of the proton and the nature of the electroweak and strong forces are probed at small distances with higher precision than any other experiment before, down to length scales of 10^{-18} m.

The partons, which do not interact amongst themselves in this model, are identified with the quarks in the proton. Neglecting radiative corrections, DIS can be described in terms of the *structure functions* $F_1(x, Q^2), F_2(x, Q^2), F_3(x, Q^2)$[1] and $F_L(x, Q^2)$ [2], which describe the distribution of the charged constituents of the proton.

The following sections introduce the kinematics of electron-proton scattering at HERA and the processes that might contribute to the signature of interest in the search for isolated leptons events performed in this analysis.

2.2.1 Kinematic variables

Fig. 2.1 illustrates the interaction of an electron or positron with the proton. The incoming electron interacts with the incoming proton via the exchange of a virtual vector boson in a *charged current* (CC) or a *neutral current* (NC) process. The NC process is mediated by a photon or a Z^0-boson exchange. In the CC process, a W-boson is exchanged, which tranforms the electron into an outgoing neutrino. Given the four-vectors of the initial and final states, $k = (E_e, \vec{k})$, $P = (E_p, \vec{P})$ and $k' = (E_{e'}, \vec{k'})$, $P' = (E_{X'}, \vec{P'})$, where $E_e, \vec{k}$ and $E_p, \vec{P}$ are the energy and momentum of the incoming electron and proton, respectively, and $E_{e'}, \vec{k'}$ and $E_{X'}, \vec{P'}$ the energy and momentum of the outgoing electron and proton, respectively, the event kinematics can be

[1] The parity violating structure function F_3 is negligible at $Q^2 \ll M_{Z,W^\pm}$

[2] At first order in perturbative QCD, F_L is zero

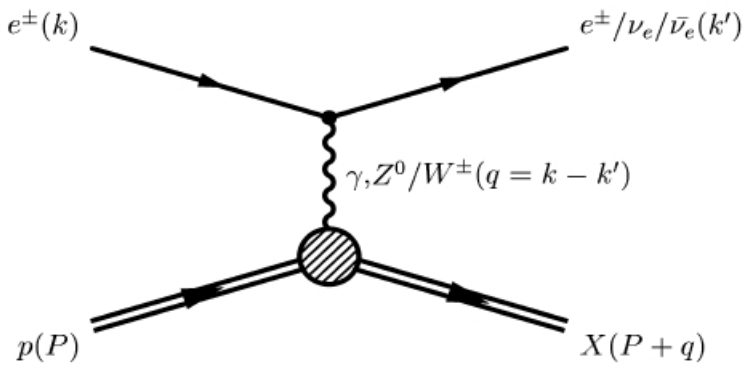

Figure 2.1: *Electron-proton scattering. The four-vectors of particles are given in parenthesis.*

described in terms of the following Lorentz invariant variables:

$$s = (k + P)^2 \tag{2.2}$$

$$Q^2 = -q^2 = -(k - k^{'})^2, \ 0 \leq Q^2 \leq s \tag{2.3}$$

$$x = \frac{Q^2}{2P \cdot q}, \ 0 \leq x \leq 1 \tag{2.4}$$

$$y = \frac{q \cdot P}{k \cdot P}, \ 0 \leq y \leq \tag{2.5}$$

The variables are related by the equation

$$s = \frac{Q^2}{xy} \tag{2.6}$$

The centre-of-mass energy $\sqrt{s}$ is fixed at HERA to a value of 318 GeV (300 GeV for 1994-1997) by the beam energies of 27.5 GeV and 920 GeV (820 GeV for 1994-2000) for leptons and protons respectively. Hence only two of the four variables are independent. The negative square of the exchange boson mass, Q^2, denotes the virtuality of the exchanged boson. Deep inelastic scattering processes (DIS) are characterized by values of Q^2 much larger than 1 GeV^2. HERA data covered a Q^2 region up to 40000 GeV^2, corresponding to a resolvable distance scale of $\lambda \approx \hbar c\sqrt{Q^2} = 10^{-18}$ m which is 1/1000 of

the proton radius. The Bjorken scaling variable x denotes the fraction of the proton momentum carried by the massless parton interacting with the lepton. This is true in a reference frame where the parton mass is negligible respect to its energy. The inelasticity parameter y can be interpreted as the fraction of the lepton energy transferred to the hadronic system in the rest frame of the proton. In this system, HERA collisions are equivalent to fixed target collisions with an incident lepton energy of ≈ 50TeV.

2.2.2 The DIS cross section

The electron scattering off a proton via the exchange of a virtual gauge boson can be described, at lowest order in QED, in terms of two structure functions, $F_1(x, Q^2)$ and $F_2(x, Q^2)$ which describe the distribution of electric charge within the proton. The double differential cross section for the neutral and charged current DIS ep cross sections with respect to x and Q^2 are determined by these structure functions as:

$$\frac{d^2\sigma^{NC}(e^{\pm}p \to eX)}{dxdQ^2} = \frac{4\pi\alpha^2}{xQ^4}[xy^2F_1 + (1-y)F_2] \tag{2.7}$$

$$\frac{d^2\sigma^{CC}(e^{\pm}p \to eX)}{dxdQ^2} = \frac{G_F^2}{2\pi}(\frac{M_W^2}{M_W^2+Q^2})^2[xy^2F_1 + (1-y)F_2] \tag{2.8}$$

$$\tag{2.9}$$

where α and G_F denote the fine structure constant and the Fermi constant, respectively. In the Quark Parton Model, F_1 and F_2 can be expressed as a sum of the quark and antiquark densities in the proton and are related by the Callan-Gross relation [19]:

$$F_2 = 2xF_1 \tag{2.10}$$

Taking QCD corrections into account, also the longitudinal structure function F_L enters; $F_L(x, Q^2) = F_2(x, Q^2) - 2xF_1(x, Q^2)$

At low $Q^2 \ll M_Z^2$, the ep cross section is dominated by photon exchange. The exchange of Z and W bosons is suppressed by their large masses and contributes only for large values of Q^2:

$$\frac{\sigma(Z, W^{\pm})}{\sigma(\gamma)} \sim \left(\frac{Q^2}{Q^2 + M_{Z,W^{\pm}}^2}\right)^2 \tag{2.11}$$

Fig. 2.2 shows the differential cross sections measured by the H1 and ZEUS collaborations as a function of Q^2 for e^-p and e^+p scattering. The

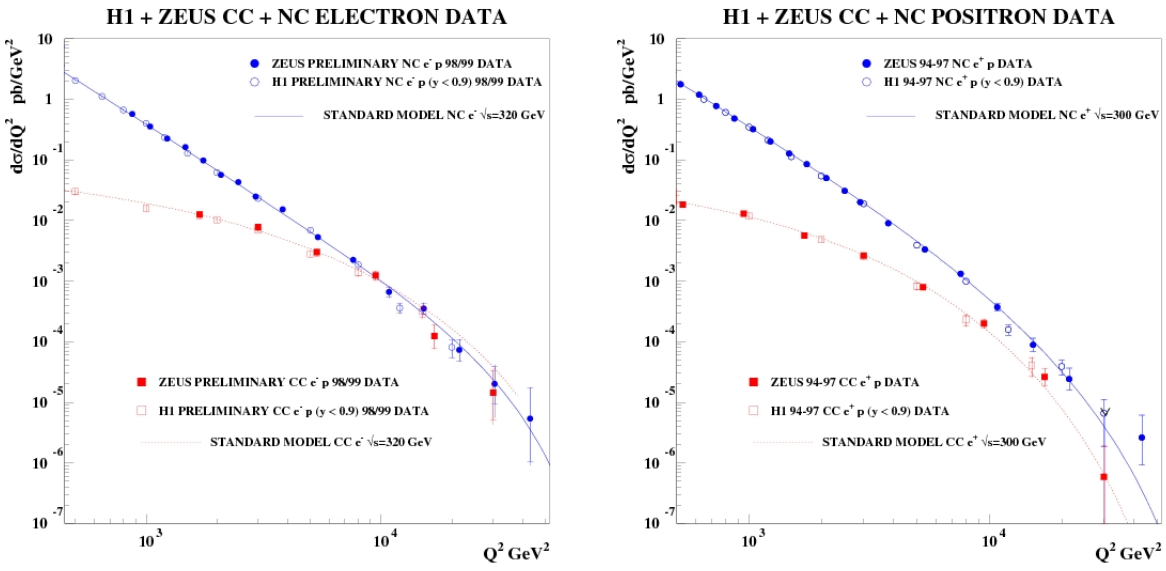

(a) *differential NC cross section* (b) *differential CC cross section*

Figure 2.2: *The differential NC and CC cross sections as function of Q^2, as obtained by the H1 and ZEUS collaborations [20] for e^-p (left) and e^+p (right) scattering. The solid and dashed lines correspond to NC DIS and CC DIS predictions from the SM respectively.*

CC cross section is suppressed with respect to the NC cross section until Q^2 reaches values close to the boson masses ($O(10^4$ GeV$^2)$). In this region, $\gamma - Z^0$ interference becomes important and leads to sizeable deviations from a

pure QED prediction. The CC cross section is larger for e^-p scattering than for e^+p scattering, due to the larger u-quark content of the proton, which is relevant for W^- exchange for e^-p scattering, as opposed to the smaller d-quark content,which is relevant for W^+ exchange in e^+p scattering.

2.2.3 QCD factorisation and the parton densities

Lepton-hadron interactions are described in QCD calculations as an incoherent sum of the interactions of the constituent partons (quarks and gluons) from one hadron with the lepton. At present the distribution of partons in hadrons cannot be calculated from first principles within perturbative theory. A separation of the short-range part (hard process) of a DIS interaction from the long-range part (soft process) is introduced, called factorisation. In this approach the proton structure function F_2 can be expressed as a convolution of the perturbatively calculable hard scattering subprocess and the parton distribution function:

$$F_2(x, Q^2) = \int_x^1 dx' f(x', \mu_F^2) \hat{\sigma}(\frac{x}{x'}, Q^2, \mu_F^2) \tag{2.12}$$

where $f(x', \mu_F^2)$ is the probability to find a quark with momentum fraction x' in the proton and $\hat{\sigma}(\frac{x}{x'}, Q^2, \mu_F^2)$ is the cross section for that quark scattering elastically off a photon with virtuality Q^2. The quark can radiate a gluon before interacting, thus lowering its effective momentum fraction of the total proton momentum from x' to x. The factorisation scale μ_F defines the scale at which this gluon radiation is absorbed into the parton density function f (PDF) rather than into the hard scattering cross section. The structure function F_2 as a physical observable is independent of the arbitrary choice of the factorisation scale μ_F.

It is possible to calculate the evolution of the PDFs as a function of Q^2

using th DGLAP evolution equations [21]. These equations use the measured values of the PDFs at a given scale to predict their evolution to some new scale. The knowledge of the evolution of the PDFs can be exploited to determine them experimentally. If the perturbative part is calculated and the cross section of a certain process is measured, the PDFs can be extracted from the data. The factorisation theorem of QCD states that the PDFs are process independent. Once determined for a given process, they can be used to make prediction for another process.

Fig. 2.3 shows an example of the PDFs extracted from a ZEUS next-to-leading order QCD analysis of data on deep inelastic scattering [22]. As

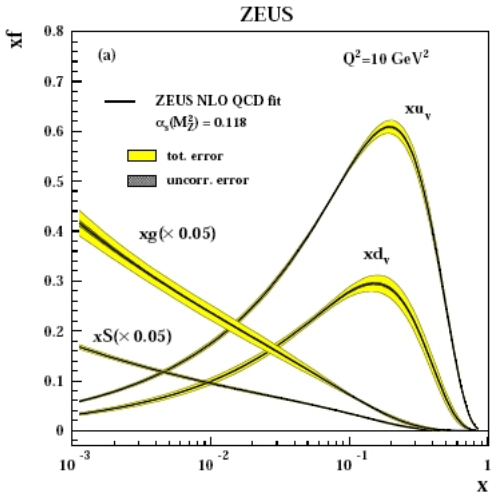

Figure 2.3: *The gluon, sea, u and d valence distribution extracted from the ZEUS NLO QCD fit at* $Q^2 = 10\ GeV^2$ *from [22].*

can be seen from the figure, the u and d valence-quark densities dominate at large values of $x \gtrsim 0.3$ while sea-quarks and gluons become important only at low values of x.

2.2.4 Photoproduction

Photoproduction (γp) is defined as the interaction of a quasi-real photon ($Q^2 \ll 1$ GeV^2) with the proton. It is the dominant process at HERA with a total cross section of $\approx 150\,\mu$b. The majority of γp interactions are soft, i.e. the transverse energy of the final state particle is small and hence they are not observed in the main detector. Hard γp interactions, resulting in jets at high transverse momenta, allow for perturbative QCD calculations to be made. The hard interactions can be divided in two types:

- *Direct process.* In the direct process the photon couples as a point-like particle to a parton from the proton. The two direct processes in leading order (LO) of the strong coupling constant α_s which are dominant at HERA, are the QCD Compton process (see Fig. 2.4 a) and the boson-gluon-fusion (BGF) (see Fig. 2.4 b).

- *Resolved process.* In this process the photon acts through vacuum fluctuation as a source of partons. One of these partons, carrying a fraction of the total photon momentum, interacts strongly with a parton from the proton, (see Fig. 2.4 c) The resolved photon structure can be subdivided in a part which can be treated by perturbation theory (anomalous resolved process) and a non perturbative part, which is usually modelled by the Vector Meson Dominance Model (VDM) and needs to be fixed by data.

2.3 High-p_T leptons production at HERA

After a general introduction of the characteristics of electron-proton scattering, in this section we will focus on the processes which are sources of genuine

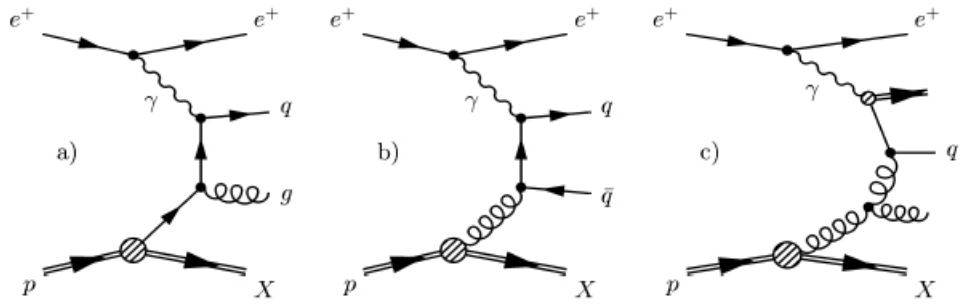

Figure 2.4: *LO Feynman diagrams for direct and resolved hard photoproduction processes: a) QCD Compton process; b) boson-gluon-fusion process; c) resolved photon process.*

high-p_T leptons at HERA: QED leptons pair production, W production and single top which could be an extra source of high-p_T leptons beyond the SM expectations.

2.3.1 Lepton pair production

Lepton pairs are produced at HERA mainly through the following two processes:

- *Bethe-Heitler process.* The dominant production mechanism for lepton pairs is the Bethe-Heitler process $ep \rightarrow \gamma\gamma \rightarrow l^+l^-$. A quasi-real photon emitted from the electron interacts with a photon radiated from a quark inside the proton. The two photons produce a lepton anti-lepton pair $e^+e^-, \mu^+\mu^-, \tau^+\tau^-$ as shown in Fig. 2.5 a). The total cross section for the photon-photon interaction is relatively large, but falls down steeply with the transverse momentum of the produced leptons ($\sim P_{T,l}^{-3}$). The leptons are produced with opposite charge and have a back-to-back topology. For an elastic reaction, with low momentum transfer on the proton side, the proton stays intact in the scattering process.

An additional hadronic jet from the scattered quark can be produced for large momentum transfers on the proton side. In a quasi-elastic reaction, the proton is transformed into an excited nucleon state, which decays into a nucleon and mostly pions. In an inelastic reaction with a large momentum transfer from the incoming proton to the hadronic final state, the proton breaks off and many hadrons are produced. In case of high momentum transferred on the electron side, the scattered electron can be observed in the main detector.

- *Internal photon conversion and Z^0 production.* An example for the production of an on- or off-shell boson with subsequent decay to lepton pair is shown in Fig.2.5 b). The lepton pairs are produced with a back-to-back topology in such reactions. The cross section peaks at low values of the invariant mass of the two leptons and the invariant mass of the Z^0 boson.

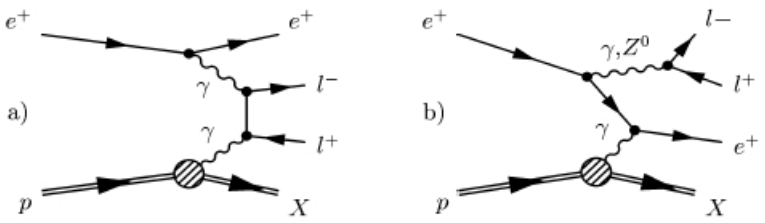

Figure 2.5: *Feynman dyagrams for the $\gamma\gamma$ lepton-pair production process a) and an example for a QED Compton process with a photon or a Z^0 boson emitted from the electron.*

Requiring that at least one of the produced leptons is accepted by the main detector and has a sizable transverse momentum ($p_T > 5$ GeV), a total cross section for lepton pair production of $\approx 120\,\text{pb}$ is expected at HERA energies.

2.3.2 Production of single W bosons

In the SM, the direct production of single W boson at HERA can occur via the processes:

$$ep \rightarrow eWX \; and \; ep \rightarrow \nu WX \tag{2.13}$$

where X denotes the hadronic final state [23]. The cross section of the second process $ep \rightarrow \nu WX$ is only about 5% of the total cross section. Seven diagrams contribute to the process $ep \rightarrow eWX$ at leading order, as shown in Fig.2.6 for the case of positron-proton scattering and with subsequent leptonic decay of the produced W boson. Diagrams a) and b) correspond to

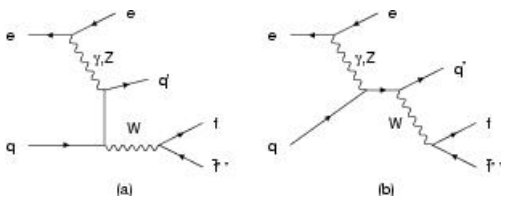

Figure 2.6: *Feynman diagrams for the lowest order single $W^{\pm}$ boson production processes in positron quark scattering at HERA, includeing the decay $W \rightarrow l\nu$.*

the radiation of a W boson from the incoming and scattered quark, respectively. The u-channel exchange of a quasi-real photon and a massless quark in these diagrams has the largest contribution to the W production cross section. Diagram c) contains the $WW\gamma$ triple-gauge-boson coupling. With a cross section measurement it is thus possible to probe anomalous $WW\gamma$ couplings. Diagrams d) and e) contain off-shell W bosons. Diagrams f) and g) represent the coupling of the W boson to the scattered neutrino and the incoming positron, respectively.

Examples of next-to-leading order (NLO) real and virtual QCD corrections to the W production process are shown in Fig.2.7. The total calculate

cross section for single W production at HERA, including NLO QCD corrections for the photoproduction regime, amounts to 0.96 pb (1.16 pb) for $\sqrt{s} = 300$ GeV (318 GeV) [24]. Taking into account the NLO QCD corrections, the remaining theoretical uncertainty on the W production cross section is $\approx 15\%$.

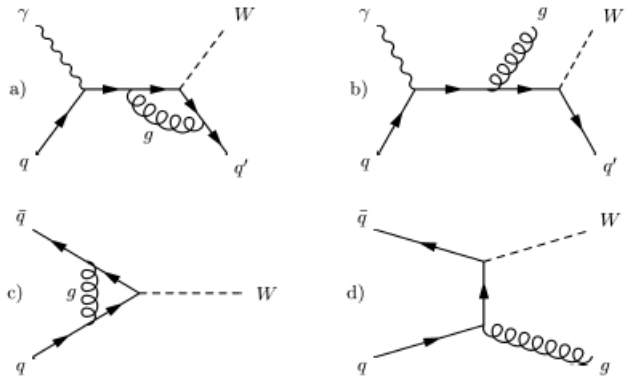

Figure 2.7: *Typical NLO diagrams contributing to the photoproduction of W bosons: a) virtual correction and b) real correction to the direct mechanism, c) virtual correction and d) real correction to the resolved mechanism*

The experimental signature for W production depends on the subsequent decay of the W boson. For the leptonic decays $W \to e\bar{\nu_e}, \mu\bar{\nu_\mu}$ one expects an electron or muon at high transverse momentum and missing transverse momentum due to the undetected neutrino. For the leptonic decay $W \to \tau\bar{\nu_\tau}$, the signature depends on the subsequent tau decay mode. For the leptonic decay modes, the signature is similar to the one of the electronic or muonic decay except for the larger missing transverse momentum due to the additional neutrinos in tau decay. For the hadronic decay, one expects a narrow jet with low particle multiplicity and also additional missing transverse momentum due to the neutrino from the tau decay. Hadronic decays $W \to qq'$ lead to events with two jets. An additional jet can be expected from all de-

cay modes in case of a sizable momentum transferred to the scattered quark. Since it originates from a different vertex in the diagram (Fig.2.6), it is separated from the W decay products in the detector. The cross section for single W production is dominated by photoproduction, leading to a steeply falling transverse momentum spectrum of the scattered quark.

2.3.3 The top quark

The top quark was discovered in 1995 in $p\bar{p}$ collisions at the Tevatron [25],[26]. With a mass of $M_{top} = 171.2 \pm 2.1$ GeV [27], measured from decays of pair produced top quarks, it is the heaviest elementary particle known to date. Since its mass is close to the electroweak symmetry breaking (EWSB) scale, the properties of the top quark could give insights into the nature of EWSB and into new physics possibly arising at higher mass scales. The top quark decays rapidly ($\tau \approx 10^{-24}$ sec) and almost exclusively through the single mode $t \to bW$, before the formation of top flavoured meson states can take place. Unlike for the lighter quarks with longer lifetime, it is thus possible to study properties of the top quark, such as spin correlations, without the difficulty that light quarks fragment before they can be detected.

The centre-of-mass energy of $\sqrt{s} = 1.96$TeV at the Tevatron allows for the production of $t\bar{t}$, while at HERA ($\sqrt{s} = 318$ GeV) and LEP ($\sqrt{s} \leq 209$ GeV) only single-top production is kinematically allowed.

2.3.4 Possible production of single top quarks at HERA

Besides the direct production as described in 2.2.6, W-bosons can also emanate from decay of singly produced t-quarks at HERA[3]. In addition to the

[3]The centre-of-mass energy of HERA does not allow for t-quark pair production.

signature of directly produced W-bosons, one expects a jet with high transverse energy from b-quark. Since the t-quark is not expected to be produced with high transverse momentum at HERA energies, this jet and the decay products of the W-boson have a back-to-back topology in the azimuthal plane.

In the SM single t-quarks can be produced via CC ep-interactions as shown in Fig. 2.8 (a),(b). Due to the very small values of the corresponding

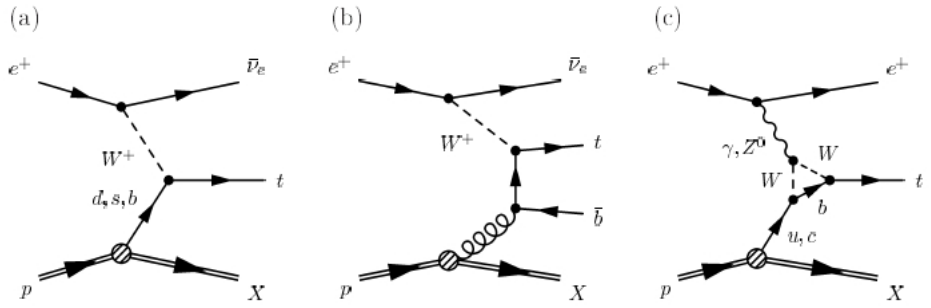

Figure 2.8: *The given examples show (a) direct CC process, (b) resolved CC process and (c) FCNCprocess at lowest order within the SM in e^+p collisions.*

off-diagonal elements of the CKM matrix [34], these flavour changing processes are highly suppressed. The expected total cross section for SM CC single t-quark production at HERA energies amounts to about 1 fb [35].

NC ep-interactions preserve the quark flavour at LO in the SM. Thus flavour changing processes are present only via higher order radiative corrections. Fig. 2.8 (c) shows an example of such one-loop *flavour changing neutral current* (FCNC) process at HERA. The dominant production mechanism for single top quarks at the HERA ep collider is expected to come from an anomalous magnetic coupling $\kappa_{tu\gamma}$ at the $t-u-\gamma$ vertex, see Fig. 2.9.

The majority of interactions at HERA involve the exchange of a photon

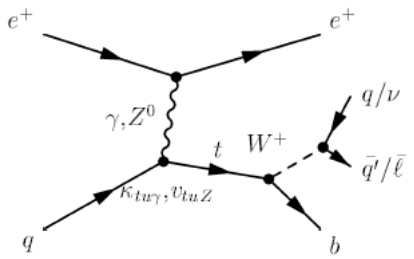

Figure 2.9: *Single top-quark production via FCNC transitions at HERA and subsequent SM decay* $t \to bW^+$.

at low virtuality (low Q^2). The Z^0 exchange is suppressed for $Q^2 \ll M_{Z^0}$. With an incident lepton energy of 27.5 GeV, the struck quark must carry a minimum momentum of 278 GeV to produce a single top quark with a mass of 175 GeV. This correspond to $x \approx 0.3$; for $x > 0.3$ the parton density of u-valence quarks is the highest, see Fig. 2.3.

Chapter 3

Search strategy and event topology

In this chapter we present an overview of the different processes which can lead to the experimental signature of interest.

3.1 Physics processes

3.1.1 Topology of single W-boson production

In W-boson production the isolated lepton and the missing transverse momentum are both due to the leptonic decay of the W-boson. An observation of the scattered beam electron is rare, because this reaction is dominated by the photoproduction regime. A sizable momentum transfer to the struck quark with a resulting separate jet is also rather unlikely. Such events are hence characterised by a small value of the hadronic P_T. For the leptonic decay ($\sim 11\%e, \sim 11\%\mu, \sim 11\%\tau$) one expects a lepton with high transverse momentum and missing transverse momentum due to the undetected

neutrino, see Fig. 3.1.

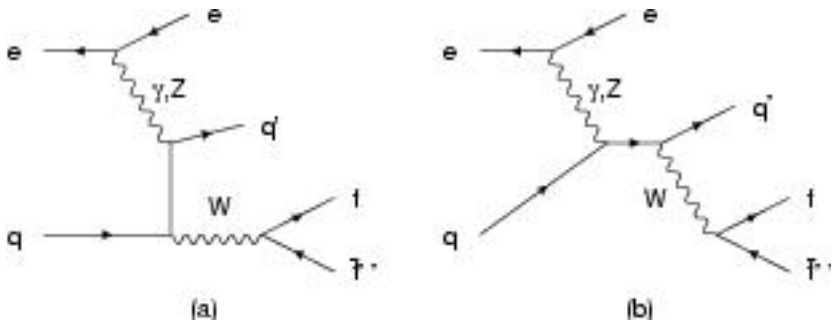

Figure 3.1: *Two Feynman diagrams showing the main contributes to the W production*

In case of muonic decay it must be considered the fact that the μ leaves a mip signal in the calorimeter so that the calorimetric missing P_T is tipically low differently from the case of the electronic decay.

For the τ decay of the W and the subsequent leptonic decay ($\sim 17\%e, \sim 17\%\mu$), the experimental signatures is very similar to the corresponding direct leptonic decay of the W wiht a typical larger missing P_T due to presence of extra neutrinos.

3.1.2 Topology of single t-quark production

In the process of single top production, the W comes from the top-quark decay together with a b-quark. The main difference, respect to the SM W production, is hence the significantly larger P_T of the W balanced by the b-quark which leads to a large hadronic P_T. Furthermore, the isolated leptons are restricted to be positively charged.

Due to the very small cross section within the SM at HERA, any observation of such a signal would, hence, be an evidence of physics beyond the SM.

The most plausible BSM mechanism is a FCNC process $eu \rightarrow et$ based on an anomalous magnetic coupling $\kappa_{tu\gamma/Z}$ at the $t-u-\gamma/Z$ vertex, see Fig. 3.2.

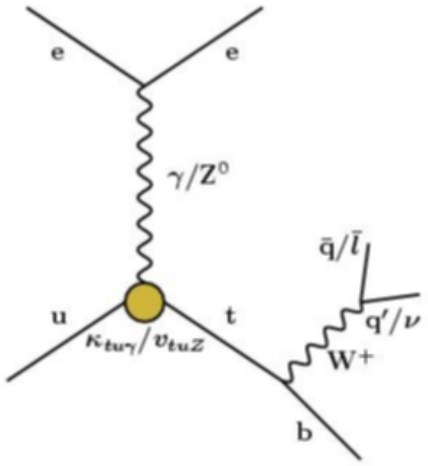

Figure 3.2: *The Feynman diagram shows the FCNC process for single t production*

The experimental signature of the process depends on the decay channel of the W^+ boson. For the leptonic channel the same considerations drawn for the SM production hold. The basic difference is the large hadronic P_T which produces a large calorimetric missing P_T also for the μ channel. The process, as shown in Fig. 3.2, can also proceeds via a Z-exchange and a vector coupling v_{tuZ}. The sensitivity on this coupling at HERA is anyway poor respect to LEP experiments [36].

3.2 Background processes

In this section we present the processes which contribute via mismeasurements to the signal of interest, lepton and missing P_T.

3.2.1 Standard model $e - p$ background

Different processes are considered:

- **charged current deep inelastic scattering:** CC DIS events are characterised by missing transverse momentum coming from the neutrino in the final state, see Fig. 3.3, 3.4. This result in signal events

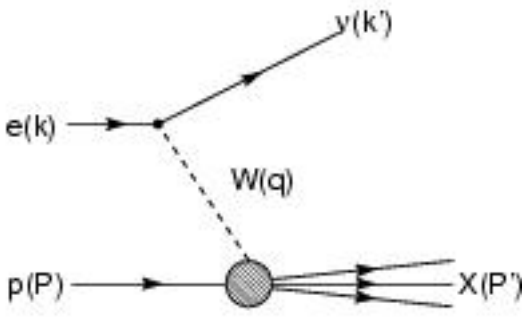

Figure 3.3: *Feynman diagram for CC interaction.*

  if a hadron is misindentified with a lepton;

- **neutral current deep inelastic scattering:** in NC DIS the scattered beam electron is usually identified within the main detector, see. Figs. 3.5, 3.6. If the hadronic final state or the electron is mismeasured or the event contains muons or neutrinos, a significant missing transverse momentum can arise;

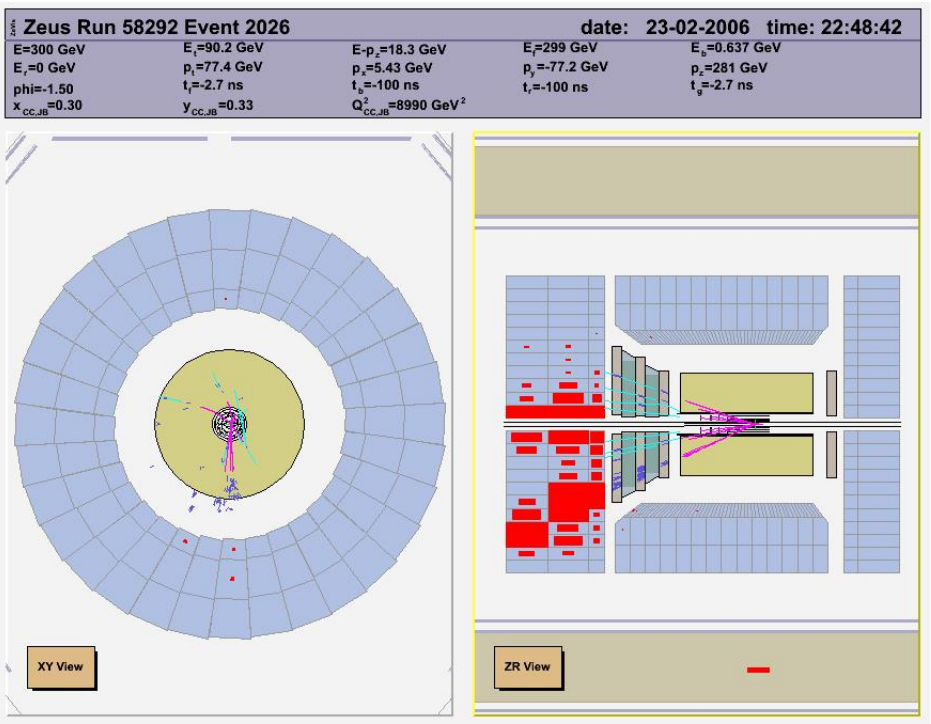

Figure 3.4: *CC event visualized with the Zeus Event VISualization (ZeVis).*

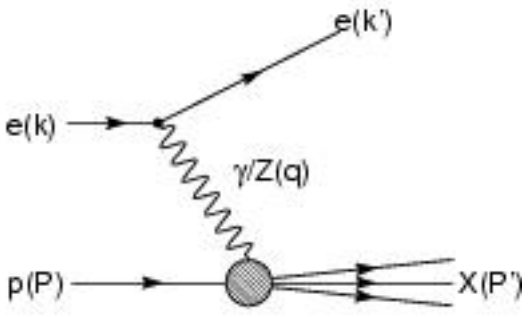

Figure 3.5: *Feynman diagram for NC interaction.*

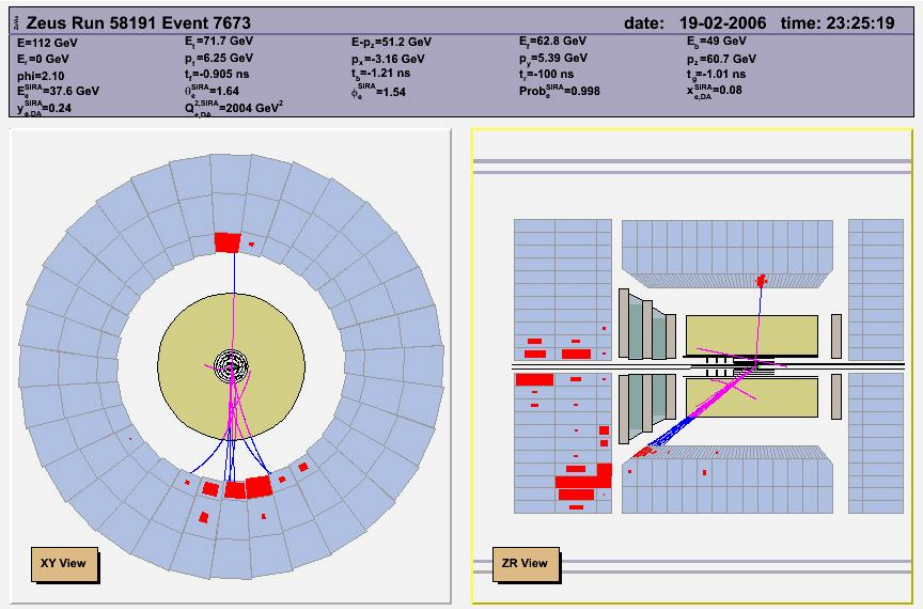

Figure 3.6: *NC event visualized with ZeVis.*

- **photoproduction:** in photoproduction processes the scattered electron escapes the detector through the beampipe. Thus a mismeasurement of the hadronic final state can lead to significant missing transverse momentum which with a fake isolated lepton could mimic a signal event. The probability of such combined mismeasurements is very low but the process should be considered due to the very large photoproduction cross section;

- **lepton pair production:** in this case there is one true lepton and the missing p_T can be caused by a measmeasurements, see Fig. 3.7. In particular for the μ-channel the μ-pair production is the main source of background.

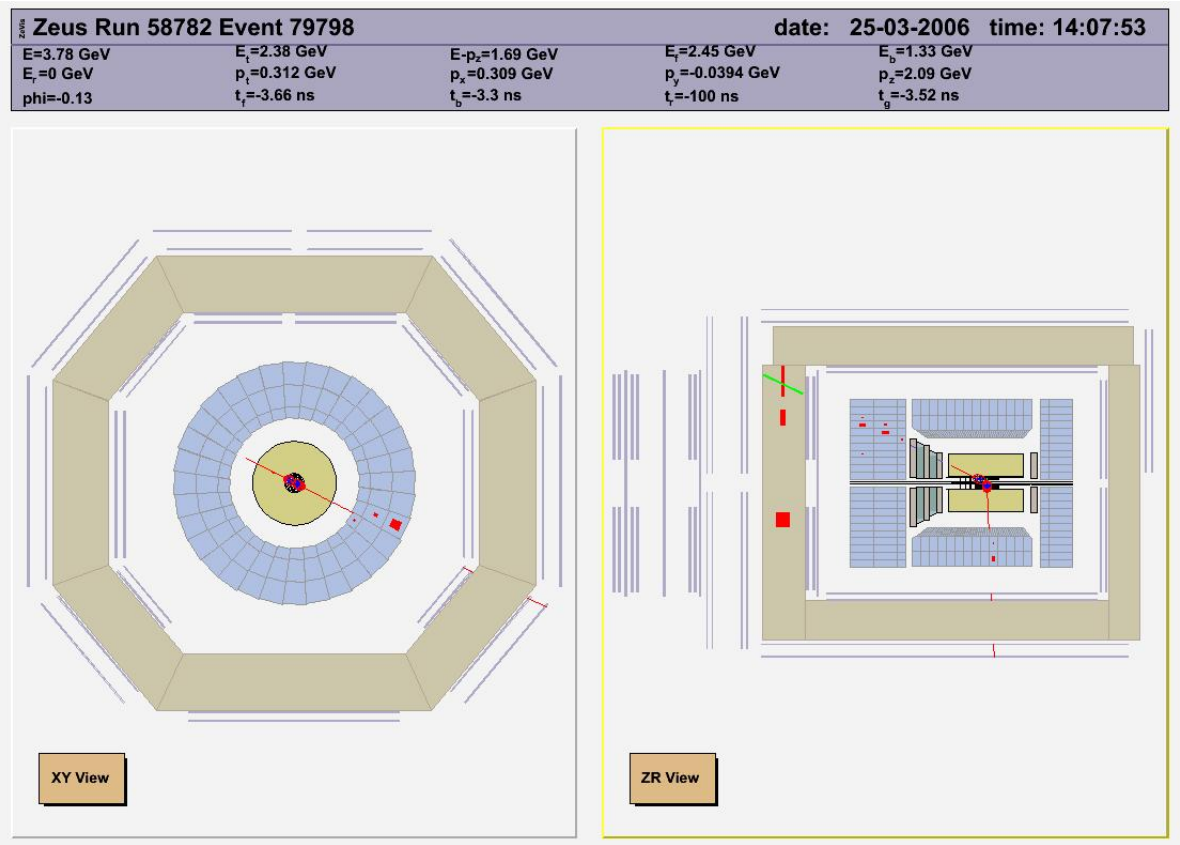

Figure 3.7: *Dimuon event visualized with ZeVis.*

3.2.2 Non $e-p$ background

Beside the $e-p$ interactions, other sources of background to be considered are:

- **beam gas interaction:** beam gas interactions are interactions of the beam particles with residual gas nuclei inside the beam pipe. In particular collisions produced from p-gas interactions upstream the ZEUS detector are tagged by the VETO wall, see Fig. 3.8

- **halo muons:** beam gas interactions can produce particles ($\pi^{\pm}$, $K^{\pm}$) which decay into muons passing the detector almost parallel to the beam line; they can overly ep events giving quite large calorimetric missing P_T, see Fig. 3.9. They can be tagged by the VETO wall and by the typical energy deposit in the CAL;

- **cosmic muons:** cosmic rays interacting in the atmosphere can produce high energy muons which can traverse the CTD (rate $\sim$ 500 Hz). Most of them pass on straight lines from top to bottom, see Fig. 3.10. They can react inelastically ($\mu N \rightarrow \nu X$) inside the detector giving large energy deposition and missing transverse momentum in the CAL. They can also overlay events from $e-p$ interactions; They can be suppressed looking at the calorimetric timing and the track distance from the reconstructed interaction vertex (see Section 6.1.1);

- **sparks in CAL cells:** sparks are spontaneous high voltage discharge of the photomultipliers (PMT) in the CAL cells. These lead to fake energy depositions and are identified by a large imbalance between the two independent PMTs used to readout a CAL cell (see Section 1.5).

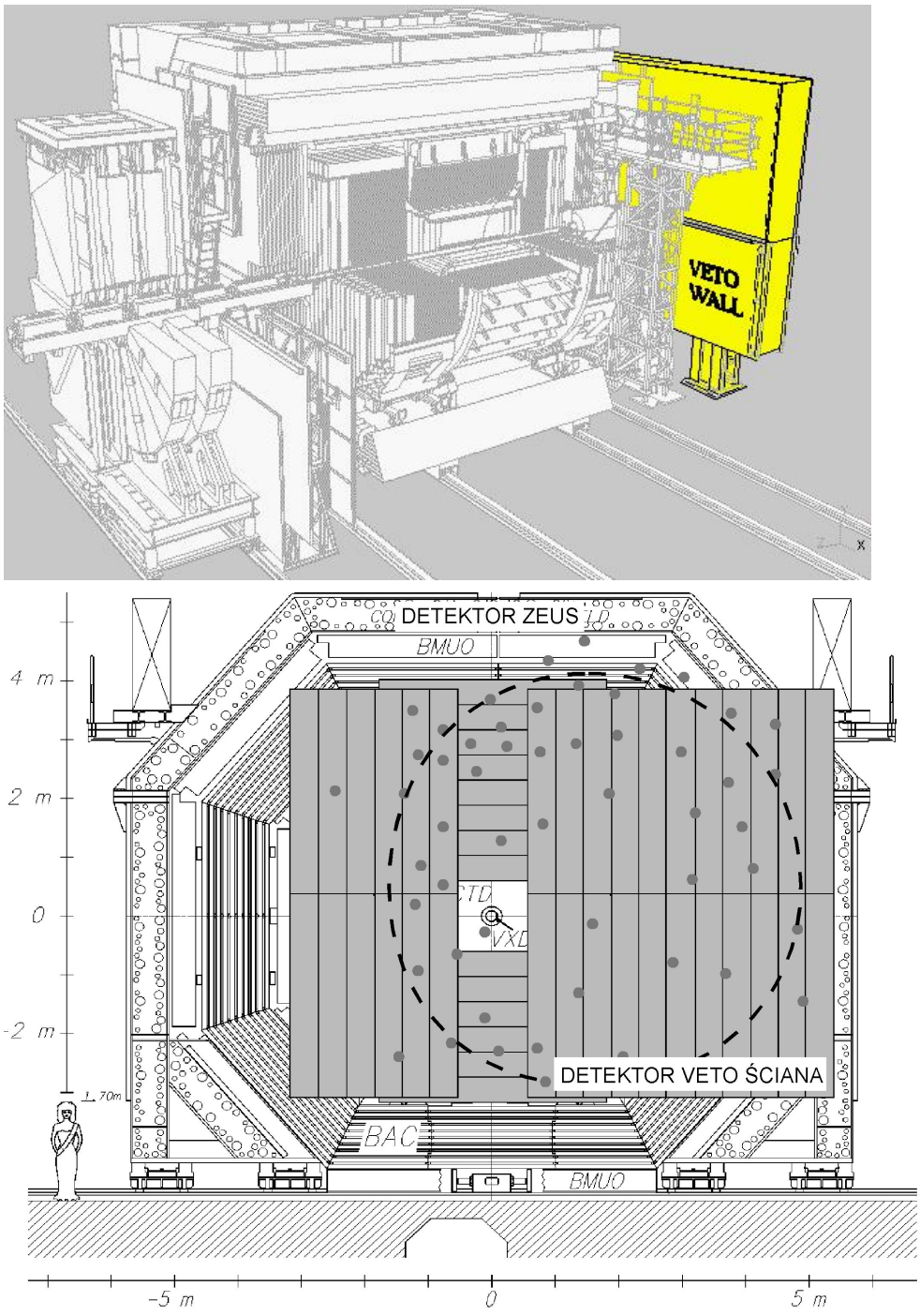

Figure 3.8: *Up: the VETO wall, situated about* 7.5 *m upstream the IP. Its main purpose is to protect the detector against particles from the beam halo. Down: range of the veto wall.*

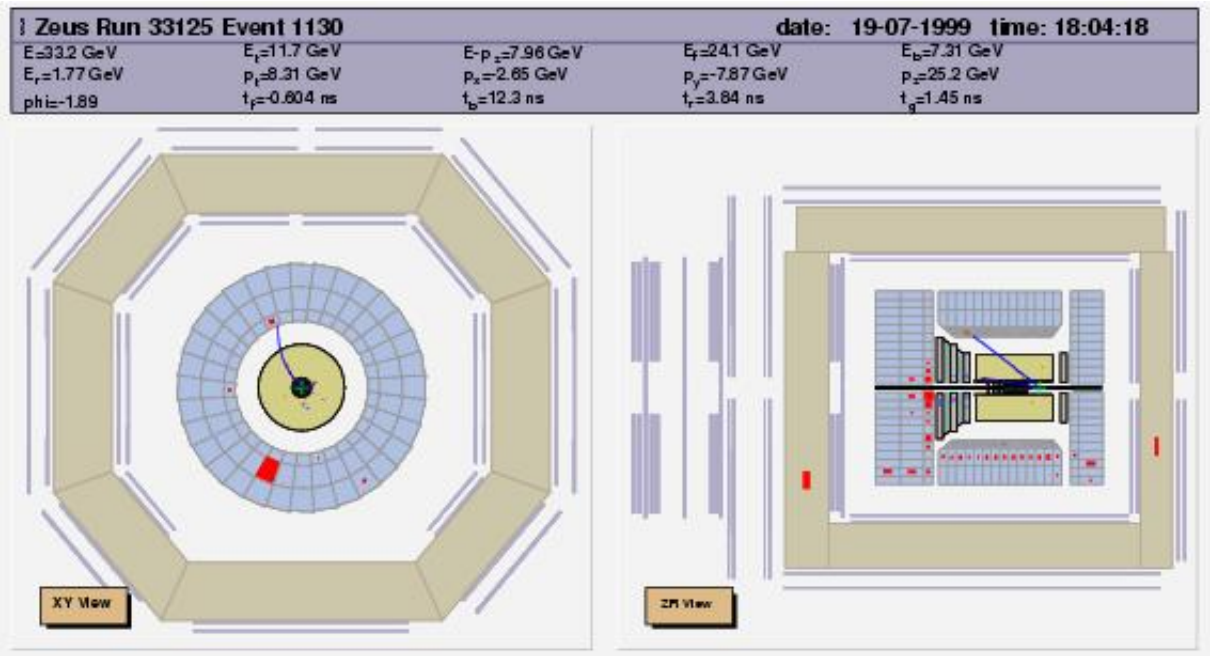

Figure 3.9: *An example of halo muon.*

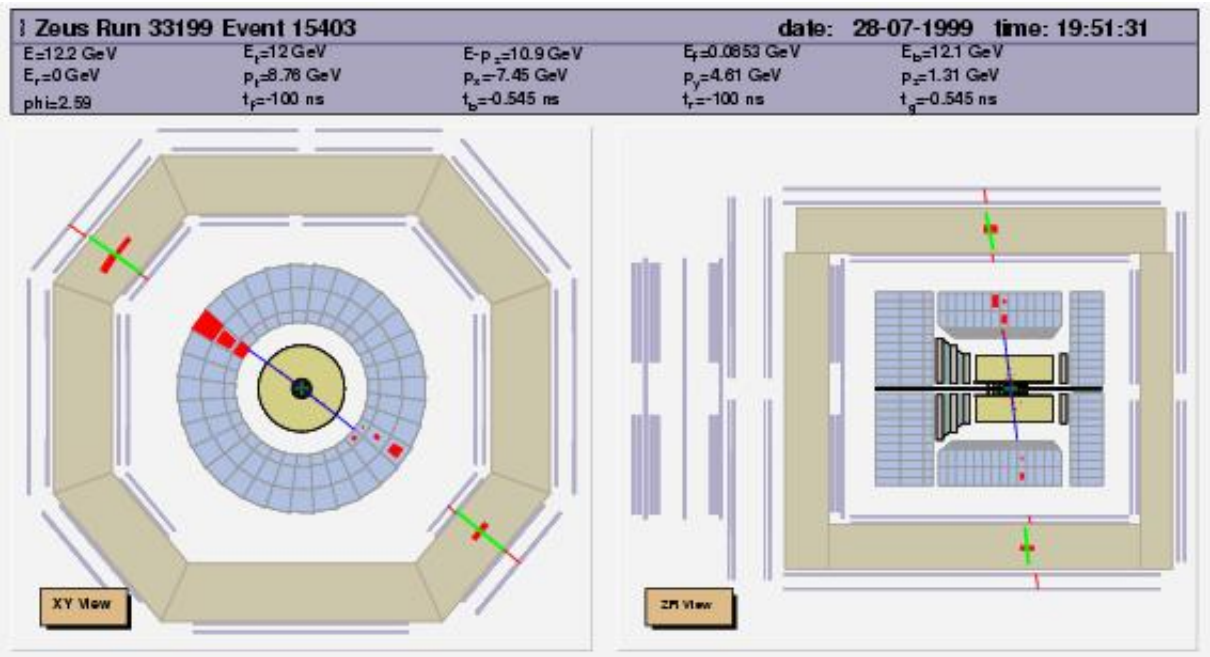

Figure 3.10: *An example of cosmic muon.*

Chapter 4

Data sample and Monte Carlo

4.1 Data Sample

The analysed data used for this analysis consist of events from e^+p and e^-p collisions taken during 2004-2005 (e^-p) and 2006-2007 e^+p and are reported in the Table 4.1.

Period	Lepton beam	$\sqrt{s}$ (GeV)	lepton beam polarization	$\mathcal{L}(\text{pb}^{-1})$
2004-2005	e^-	318	-1	46.92
2004-2005	e^-	318	+1	87.68
2004-2005				134.60 ± 1.9%
2006-2007	e^+	318	-1	46.03
2006-2007	e^+	318	+1	95.72
2006-2007				141.75 ± 2.3%

Table 4.1: *Data samples used.*

4.2 Monte Carlo

Monte Carlo (MC) generators are used to simulate the processes. Their output consists of the final state particles and their four-momenta. This information is then passed to a subsequent program that simulates the detector response. The simulation of the process involves different steps. The first step is the simulation of the hard process, that, in *ep* collision, means the interaction between the electron or the photon and the parton inside the proton. The simulation has then to take into account the initial and final state QCD radiation that can be calculated perturbatively. The last and non trivial step is to go from the parton level to final state hadrons; this step is called *hadronization*. In this chapter a description of the different methods used by the MC generators to treat the QCD radiation and the hadronization will be given. Then the event generators used to simulate the SM background and the signal will be described.

4.2.1 QCD radiation

The QCD initial- or final-state radiation in DIS accounts for events with two or three jets in the final state, see Fig. 4.1. The most common approaches to describe the QCD radiation are the Color Dipole Model (CDM) [37] and the Matrix Element Parton Shower Model (MEPS). In the CDM method the radiation is assumed to be emitted by independently radiating dipoles, see Fig. 4.2 (a). In *ep* scattering case, the first dipole is made up by the struck quark and the proton remnant. The gluon radiated by the first dipole is itself, together with the struck quark and the proton remnant, a source of dipoles that can emit softer gluons.

In the MEPS model, the radiation corresponds to higher orders in per-

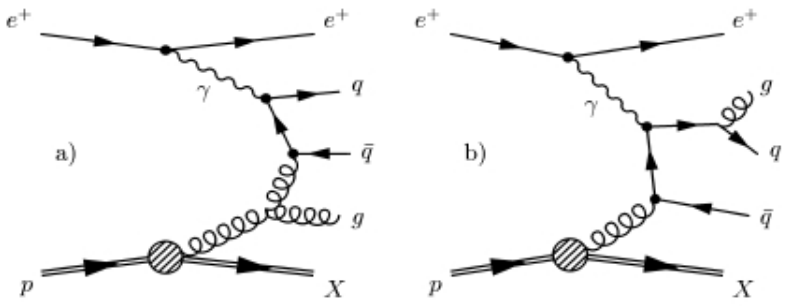

Figure 4.1: *Example Feynman diagrams for three-jet production through initial state (left) and final state radiation (right).*

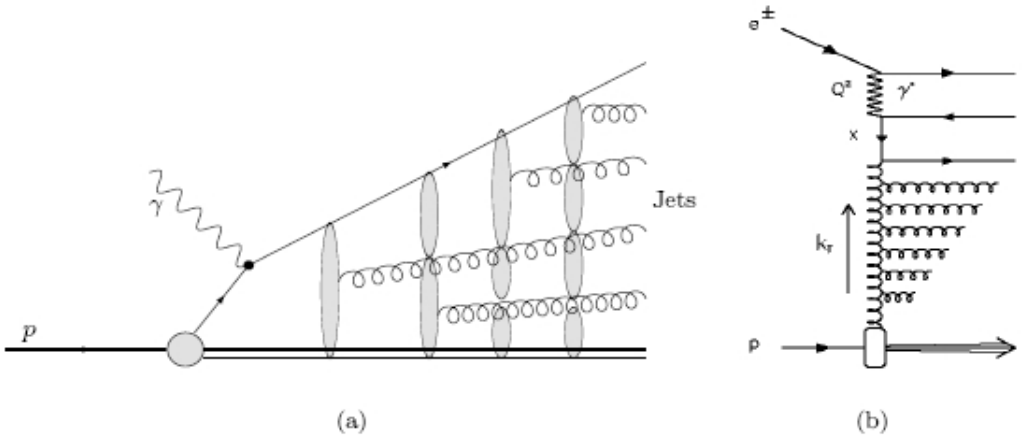

Figure 4.2: *(a) Gluon emission by color dipoles in the CDM; (b) angular ordering in the parton shower model.*

turbative QCD; the higher order terms are all summed up using the DGLAP "leading log approximation". The perturbation is applicable down to parton energies of $\approx$ 1GeV. A parton shower is generated and the splitting processes are calculated using the Altarelli-Parisi splitting functions [21]. The angular ordering, see Fig. 4.2 (b), is imposed for the final radiation: considering, for example the branching $q_0 \rightarrow qg$, the original color charge is inherited by the gluon while q and g share a color-anticolor pair.

4.2.2 Hadronization

Perturbative QCD describes how the partons evolve but, in the detector, due to the color confinement, we can observe only colorless hadrons. The process that leads to the formation of hadrons starting from partons is described by two models: the Lund string model [38] and the Cluster fragmentation model [39].

The Lund string fragmentation model treats the color field between diverging $q\bar{q}$ pairs as a string of constant energy density of $\approx$ 1GeV/fm, thus taking into account the self interactions of the gluons. As the distance between $q\bar{q}$ increases, the potential energy of the string becomes high enough to produce another $q\bar{q}$ couple. The string thus splits consecutively into smaller parts and the process continues with the formation of smaller strings and ends when the energy of the initial $q\bar{q}$ couple is exhausted.

The Cluster fragmentation model exploits the concept of pre-confinement of color. Gluons are non-perturbatively split into $q\bar{q}$ couples. Color singlet are then considered. Due to the color pre-confinement the invariant mass and the size of the clusters peak to low values and they are asymptotically independent from the hard subprocess and the energy scale. Clusters subsequently decay into pairs of colorless hadrons or, if they are too light, they

decay into the lightest hadrons of their flavor, exchanging four-momentum with the neighboring clusters to adjust the mass.

4.3 Simulation of the background events

4.3.1 Photoproduction

The generator HERWIG [40] was used in its version 5.9 to simulate both direct and resolved photoproduction. The proton structure function was CTEQ4D [41], the photon structure function GRV-G LO [42]. Partonic processes and initial- and final-state parton showers were simulated using leading order matrix elements. The hadronization was simulated using the Cluster model. The W signal events have a high transverse energy in the final state. Therefore, in order to reduce the amount of events to be processed, events with low P_t^{hard}, defined as the lower value of the momentum of the two outgoing partons of the hard process, are discarded at the parton level (before the hadronization). The number of final events is further reduced requiring a minimum transverse energy, E_t, defined as the scalar sum of the transverse momentum of the final state particles after the hadronization. In Table 4.2 the kinematical cuts and the characteristics of the samples used to simulate photoproduction for the different data samples are reported.

4.3.2 Deep inelastic scattering, NC and CC

Neutral current and charged currents events can be a source of background in searching events with isolated leptons and missing P_T.

NC DIS and CC events were simulated for this analysis with the genera-

MC sample	Period	cross section (pb)	N. of events	$\mathcal{L}(\,\mathrm{pb}^{-1})$
Direct PhP	06-07 e^+p	2830.	515466	182.14
$P_T^{hard} > 6.\mathrm{GeV}$				
$E_T > 30.\mathrm{GeV}$				
Resolved PhP	06-07 e^+p	11900.	615279	51.70
$P_T^{hard} > 6.\mathrm{GeV}$				
$E_T > 30.\mathrm{GeV}$				
Direct PhP	04-05 e^-p	2830.	519980	183.73
$P_T^{hard} > 6.\mathrm{GeV}$				
$E_T > 30.\mathrm{GeV}$				
Resolved PhP	04-05 e^-p	11900.	1941484	163.13
$P_T^{hard} > 6.\mathrm{GeV}$				
$E_T > 30.\mathrm{GeV}$				

Table 4.2: *MC photoproduction direct and resolved samples.*

tor ARIADNE 4.12 [46] interfaced to HERACLES 4.6.1 [43] via DJANGOH 1.6 [44], using CTEQ5D [45] parametrisatrions of the proton PDF. The simulation of the QCD cascades with ARIADNE was based on the color dipole model. The NC and CC samples were generated with a $Q^2 > 100.\text{GeV}^2$ and $Q^2 > 10.\text{GeV}^2$ respectively. The samples are listed in Table 4.3.

MC sample	Period	cross section (pb)	N. of events	$\mathcal{L}(\text{ pb}^{-1})$
NC $Q^2 > 100.\text{GeV}^2$	06-07 e^+p	8111.06	5901096	727.54
CC $Q^2 > 10.\text{GeV}^2$	06-07 e^+p	44.82	249960	5576.97
NC $Q^2 > 100.\text{GeV}^2$	04-05 e^-p	8147.46	7751606	951.41
CC $Q^2 > 10.\text{GeV}^2$	04-05 e^-p	79.42	249975	3147.51

Table 4.3: *MC samples, NC and CC.*

4.3.3 Lepton pair production

Since di-lepton events contain high p_T leptons in the final state, they are also a source of background for this analysis.

The di-lepton production processes were simulated using the generator GRAPE 1.1j (GRAce-based generator for Proton Electron collisions), [47] The generator, which uses the general tool GRACE to generate the FORTRAN code to calculate the Feynman amplitudes, permits to calculate the di-lepton cross section with the exact matrix elements in the electroweak the-

ory. The calculated processes, $\gamma\gamma$ (Bethe-Heitler), γZ^0, $Z^0 Z^0$, QED Compton and Z^0 on/off shell production, have already been described in Sec. 2.3.1.

The calculation of the cross section is done by dividing the process into three kinematic regions: elastic, quasi-elastic and DIS. In the elastic events, the proton does not break up: there is no proton remnant and the final state is constituted only by the two final leptons. In quasi-elastic events the proton breaks up into a low-mass state; in DIS the proton breaks up and the scattered electron or positron is visible in the detector. The Lorentz invariants used to discriminate between the three regions are the negative four-momentum transfer squared at the proton vertex Q_p^2 and the square of the invariant mass of the hadronic final state M_{hadr}^2:

$$Q_p^2 = (p_{e,in} - (p_e + p_{l^+} + p_{l^-}))^2 M_{hadr}^2 = ((p_{e,in} + p_{p,in}) - (p_e + p_{l^+} + p_{l^-}))^2 \quad (4.1)$$

where $p_{e,in}$ and $p_{p,in}$ are the four-momenta of the incoming electron and proton respectively, and p_e, p_{l^+}, p_{l^-} are the four-momenta of the outgoing electron and leptons respectively.

The three kinematic regions are defined by:

- elastic: $M_{hadr} = M_p$.
- quasi-elastic: (I) $Q_p^2 < 1\text{GeV}^2$, (II) $M_p + M_{\pi^0} < M_{hadr} < 5\text{GeV}$.
- DIS (I) to (IV): $Q_p^2 > 1\text{GeV}^2$ and $M_{hadr} > 5.\text{GeV}$, with the subprocesses (I) to (IV) corresponding to the flavour of the initial state quark ($u; \bar{u}$; d or s; $\bar{d}$ or $\bar{s}$).

At least one of the two leptons was required to be in the polar region $5^\circ < \theta < 175^\circ$ and at least one of the two leptons was required to have a transverse momentum $p_T^{lept} > 5.\text{GeV}$. The proton structure function used was CTEQ5L [45]. Tables 4.4 and 4.5 list the samples used.

Process	Period	cross section (pb)	N. of events	$\mathcal{L}$(pb^{-1})
Elastic $\mu^+\mu^-$	06-07 e^+p	10.20	30k	$2.940 * 10^3$
Quasi-el 1 $\mu^+\mu^-$	06-07 e^+p	4.97	30k	$6.037 * 10^3$
Quasi-el 2 $\mu^+\mu^-$	06-07 e^+p	0.17	30k	$1.799 * 10^5$
DIS 1 $\mu^+\mu^-$	06-07 e^+p	13.00	30k	$2.307 * 10^3$
DIS 2 $\mu^+\mu^-$	06-07 e^+p	2.68	30k	$1.119 * 10^4$
DIS 3 $\mu^+\mu^-$	06-07 e^+p	2.38	30k	$1.263 * 10^4$
DIS 4 $\mu^+\mu^-$	06-07 e^+p	1.22	30k	$2.468 * 10^4$
Elastic $\tau^+\tau^-$	06-07 e^+p	6.35	30k	$4.724 * 10^3$
Quasi-el 1 $\tau^+\tau^-$	06-07 e^+p	3.56	30k	$8.420 * 10^3$
Quasi-el 2 $\tau^+\tau^-$	06-07 e^+p	0.14	30k	$2.082 * 10^5$
DIS 1 $\tau^+\tau^-$	06-07 e^+p	5.23	30k	$5.732 * 10^3$
DIS 2 $\tau^+\tau^-$	06-07 e^+p	1.05	30k	$2.865 * 10^4$
DIS 3 $\tau^+\tau^-$	06-07 e^+p	0.95	30k	$3.144 * 10^4$
DIS 4 $\tau^+\tau^-$	06-07 e^+p	0.49	30k	$6.268 * 10^4$
Elastic e^+e^-	06-07 e^+p	13.39	30k	$2.240 * 10^3$
Quasi-el 1 e^+e^-	06-07 e^+p	5.75	30k	$5.218 * 10^3$
Quasi-el 2 e^+e^-	06-07 e^+p	0.22	30k	$1.365 * 10^5$
DIS 1 e^+e^-	06-07 e^+p	32.63	30k	$9.193 * 10^2$
DIS 2 e^+e^-	06-07 e^+p	8.26	30k	$3.633 * 10^3$
DIS 3 e^+e^-	06-07 e^+p	6.48	30k	$4.633 * 10^3$
DIS 4 e^+e^-	06-07 e^+p	3.66	30k	$8.196 * 10^3$

Table 4.4: *MC samples 06-07e^+p, dileptons.*

Process	Period	cross section (pb)	N. of events	$\mathcal{L}$(pb^{-1})
Elastic $\mu^+\mu^-$	04-05 e^-p	13.39	30k	$2.240 * 10^3$
Quasi-el 1 $\mu^+\mu^-$	04-05 e^-p	5.76	30k	$5.212 * 10^3$
Quasi-el 2 $\mu^+\mu^-$	04-05 e^-p	0.22	30k	$1.365 * 10^5$
DIS 1 $\mu^+\mu^-$	04-05 e^-p	33.35	30k	$8.996 * 10^2$
DIS 2 $\mu^+\mu^-$	04-05 e^-p	7.99	30k	$3.754 * 10^3$
DIS 3 $\mu^+\mu^-$	04-05 e^-p	6.45	30k	$4.651 * 10^3$
DIS 4 $\mu^+\mu^-$	04-05 e^-p	3.69	30k	$8.132 * 10^3$
Elastic $\tau^+\tau^-$	04-05 e^-p	6.35	30k	$4.724 * 10^3$
Quasi-el 1 $\tau^+\tau^-$	04-05 e^-p	3.56	30k	$8.420 * 10^3$
Quasi-el 2 $\tau^+\tau^-$	04-05 e^-p	0.14	30k	$2.082 * 10^5$
DIS 1 $\tau^+\tau^-$	04-05 e^-p	5.23	30k	$5.732 * 10^3$
DIS 2 $\tau^+\tau^-$	04-05 e^-p	1.05	30k	$2.865 * 10^4$
DIS 3 $\tau^+\tau^-$	04-05 e^-p	0.95	30k	$3.144 * 10^4$
DIS 4 $\tau^+\tau^-$	04-05 e^-p	0.49	30k	$6.268 * 10^4$
Elastic e^+e^-	04-05 e^-p	6.35	30k	$4.724 * 10^3$
Quasi-el 1 e^+e^-	04-05 e^-p	3.56	30k	$8.420 * 10^3$
Quasi-el 2 e^+e^-	04-05 e^-p	0.10	30k	$2.873 * 10^5$
DIS 1 e^+e^-	04-05 e^-p	5.25	30k	$5.716 * 10^3$
DIS 2 e^+e^-	04-05 e^-p	1.04	30k	$2.876 * 10^4$
DIS 3 e^+e^-	04-05 e^-p	0.95	30k	$3.156 * 10^4$
DIS 4 e^+e^-	04-05 e^-p	0.48	30k	$6.253 * 10^4$

Table 4.5: *MC samples 04-05e^-p, dileptons.*

4.3.4 Production of single $W^{\pm}$ bosons

This section presents a brief discussion of single W production with the introduction of the Monte Carlo generator EPVEC 1.1 [48], which is a leading order (LO) program and does not include QCD radiation.

In principle, W production can occur through either neutral or charged current like interactions:

$$ep \rightarrow eWX\ NC \tag{4.2}$$

$$ep \rightarrow \nu WX\ CC \tag{4.3}$$

where the X is the hadronic final state.

The leading order Feynman diagrams for $e^+p \rightarrow e^+W^{\pm}X$ that are considered from the EPVEC program are shown in Fig. 4.3; The dominant diagrams are (a) and (b); (c) involves the triple gauge boson $WW\gamma$ vertex, (f) and (g) are suppressed by the presence of a secondary heavy propagator and (d) and (e), containing off-shell Ws are necessary to preserve electromagnetic gauge invariance. Diagrams for $e^+p \rightarrow \bar{\nu}W^{\pm}X$ processes can be formed by, for example, replacing the photon in (a) with a W; such processes are expected to have a cross section an order of magnitude lower than $e^+p \rightarrow e^+W^{\pm}X$.

The cross section for $e^+p \rightarrow e^+W^{\pm}X$ has been calculated by splitting the phase space into two regions:

$$\sigma = \sigma(|u| > u_{cut}) + \int_{u_{cut}}^{u} \frac{\mathrm{d}\sigma}{\mathrm{d}|u|}\mathrm{d}|u| \tag{4.4}$$

where $u = (p_q - p_W)^2$ is the square of the four-momentum transferred from the incoming quark to the final state W boson. The first term (DIS W boson production) is calculated using helicity amplitudes for the process $e^{\pm}q \rightarrow e^{\pm}Wq', W \rightarrow l\bar{\nu}$. The cross section for $|u| < u_{cut}$ (resolved photon W boson production) is calculated by folding the Drell-Yan cross section for

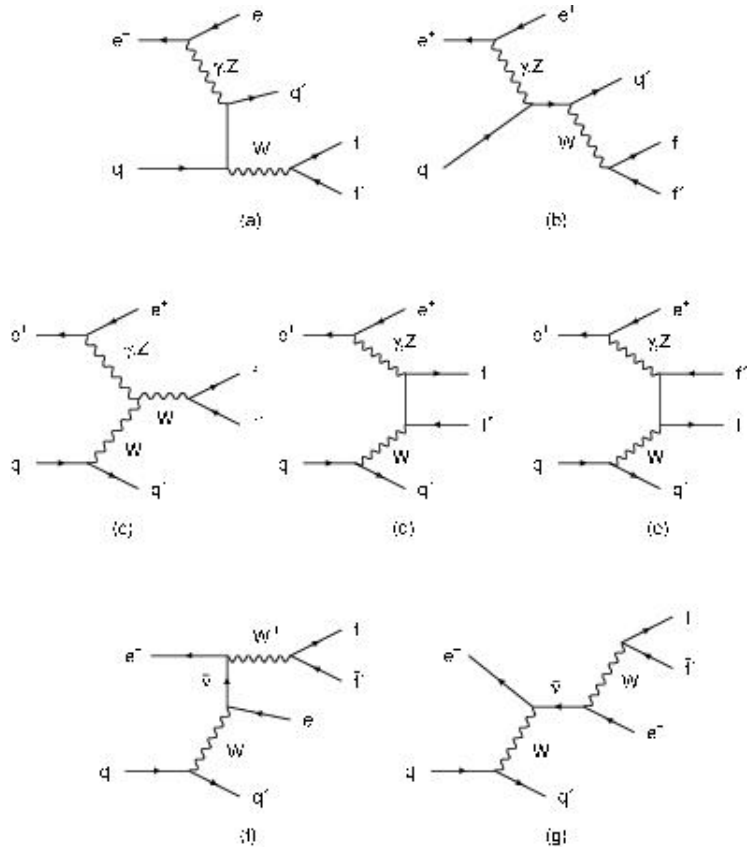

Figure 4.3: *Leading order Feynman diagrams for the process* $e^+p \to e^+W^\pm X$.

$q\bar{q}' \rightarrow W \rightarrow l\bar{\nu}$ with the parton densities in the proton and the effective parton densities for the resolved photon emitted by the incoming lepton; the uncertainties introduced by the choice of u_{cut} is $\approx 5\%$, (Fig. 4.4).

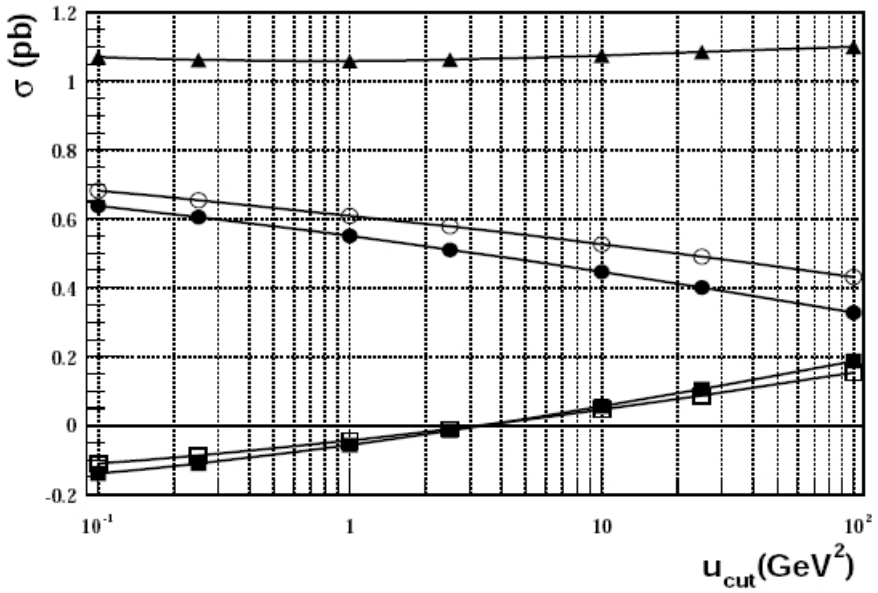

Figure 4.4: *Dependence of W cross section from u_{cut} at $\sqrt{s} = 320 GeV$. Open and full circles refer to W^+ and W^- DIS processes respectively, open and full squares refer to W^+ and W^- PhP processes respectively. The full triangles are the sum of the four processes.*

The hadronization and decay of unstable particles is simulated using the LUND [38] string model as implemented in JETSET 7.4 [54]. The sum of the DIS and resolved cross sections (full triangles in Fig. 4.4) varies little with u_{cut}, see Fig. 4.4, choosen here to be 25GeV^2. Fig. 4.5 shows the dependence of the cross section from the polarization of the lepton beam.

Next-to-leading-order (NLO) real and virtual QCD corrections for the photoproduction regime were taken into account by reweighting the EPVEC MC samples to the cross section obtained from recent LO and NLO calcula-

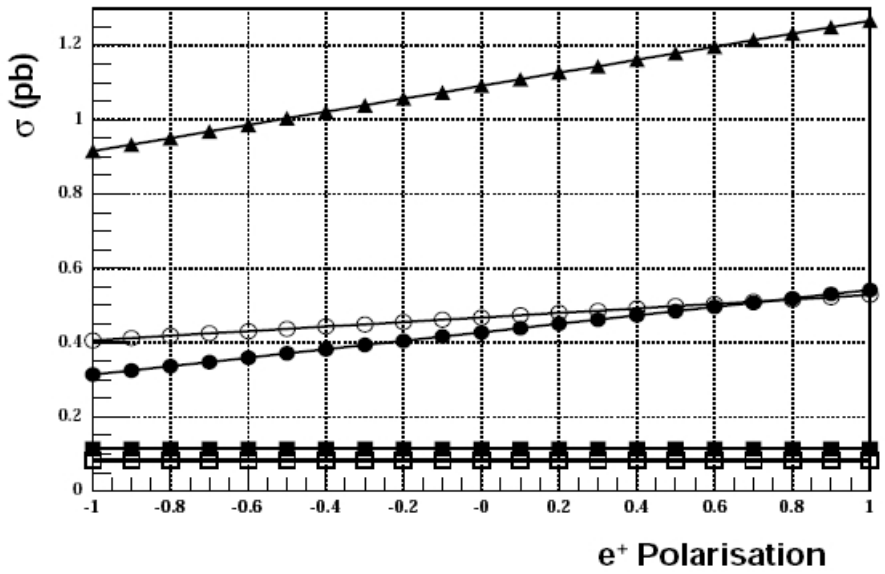

Figure 4.5: *Dependence of W cross section from polarization of the lepton beam. The symbol are the same used in Fig. 4.4.*

tions [55]. In these calculations, two phase space regions were distinguished: the deep inelastic region at high values of Q^2 and the photoproduction region at low values of Q^2. The QCD corrections were calculated for the dominant direct photon mechanism at finite transverse momentum of the W boson. and for the total cross section of the resolved part. The reweighting factors for scaling the EPVEC samples to the cross section calculations were obtained as the ration of the two cross sections in bins of the transverse momentum of the produced W boson p_T^W:

$$weight(p_T^W) = \frac{(d\sigma/dp_T^W)_{NLO}}{(d\sigma/dp_T^W)_{EPVEC}} \tag{4.5}$$

The single W production MC samples used for this analysis are listed in Table 4.6. The cross section and luminosity do not include NLO contributions.

Process	Period	cross section (pb)	N. of events	$\mathcal{L}$(pb^{-1})
W^+ DIS	06-07 e^+p	0.50	48432	$9.747 * 10^4$
W^+ RES	06-07 e^+p	0.08	10000	$1.220 * 10^5$
W^- DIS	06-07 e^+p	0.41	47995	$1.169 * 10^5$
W^- RES	06-07 e^+p	0.11	10000	$8.773 * 10^4$
W^+ DIS	04-05 e^-p	0.50	50000	$1.093 * 10^5$
W^+ RES	04-05 e^-p	0.08	50000	$6.100 * 10^5$
W^- DIS	04-05 e^-p	0.41	50000	$1.153 * 10^5$
W^- RES	04-05 e^-p	0.11	50000	$4.376 * 10^5$

Table 4.6: *MC samples, W production.*

4.3.5 Simulation of single top process

At HERA we are most sensitive to single top production mediated by γ exchange via a FCNC coupling $\kappa_{tu\gamma}$ (see Sections 2.3.3 and 2.3.4). The process was simulated using both HEXF [56] and COMPHEP [57]. Since the process does not depend on the lepton beam charge, only samples with the 06-07e^+p configuration have been used.

HEXF is a generator of excited fermions based on the fenomenological model of Hagiwara et al.[58, 59]. It was adapted to single top production requiring the generation of an excited u quark (u^*) with the same mass and decay channel of the top. HEXF includes initial-state radiation from the beam electron using Weizsäcker-Williams approximation [60]. The matrix-element and parton-shower of Lepto [61] is used for the simulation of the QCD cascade. The hadronization and decay of unstable particles is simulated using the Lund [38] string model as implemented in JETSET 7.4 [54]. The parton density functions of the proton are evaluated from the MRSA

parametrisation.

CompHEP is a program which allows to calculate process cross section at the tree level and to simulate the final state of the hard scattering. It is intefaced to PYTHIA [62] for the simulation of the hadronic cascade and the hadronization and decay of unstable particles. The QCD radiation is simulated within PYTHIA using a combination of the matrix-elements and parton-showers approaches. For the fragmentation, the Lund string model of JETSET is used.

The Table 4.7 lists the samples used.

Period	Top mass (GeV)	Process	Decay	Generator	N. of events
06-07e^+	170	FCNC $\kappa_{tu\gamma}$	$t \to bW$	HEXF	50000
06-07e^+	175	FCNC $\kappa_{tu\gamma}$	$t \to bW$	HEXF	50000
06-07e^+	180	FCNC $\kappa_{tu\gamma}$	$t \to bW$	HEXF	50000
06-07e^+	175÷190	FCNC $\kappa_{tu\gamma}$	$t \to bW$	COMPHEP	15079

Table 4.7: *MC samples, single top production.*

4.3.6 Detector simulation

To compare the MC simulation with the data, the generated MC events are passed to a simulation of the ZEUS detector. The program MOZART [50] (Monte carlo for Zeus Analysis, Reconstruction and Trigger) is a full GEANT [49] simulation of the ZEUS detector and simulates the response of the different detector components and the interaction with inactive material taking into account the geometric acceptance and the effects of dead material. Each version of MOZART is designed such that it can simulate the detector configuration of any year of data-taking. The output of MOZART is passed

to ZGANA [51] which simulates the trigger behaviour and then passed to the event reconstruction package ZEPHYR [52]. The program ZEPHYR is used to reconstruct both Monte Carlo and real events. ZEPHYR contains the event reconstruction routines for the different components, including the calibration corrections. It builds physics objects like tracks from single hits and applies calibrations. The final events, both MC and data, are organized using the ADAMO [53] data management system.

Chapter 5

Events Reconstruction

In this chapter will be described the reconstruction of the physical objects used in this analysis: tracks and vertices, calorimeter variables, electrons, muons, jets.

5.1 Tracks and vertices reconstruction

VCTRAK [63] is the package used in ZEUS for the reconstruction of tracks, primary and secondary vertices inside the detector. Its development, begun in 1990 and continued along the years taking into account the different configurations of the ZEUS tracking system. All reconstructed tracks use hits from the CTD integrating also informations from other tracking devices (MVD, F/RTD, STT). The reconstruction of the tracks proceeds through the local coordinate reconstruction, the track pattern recognition and the track fit. Once the tracks have been reconstructed, they are used for the vertex finding and fit.

5.1.1 Beam spot

In this analysis, for rejecting the cosmic background, has been used the impact parameter of the tracks respect to the beam spot.

The beamspot is a measure of the average primary vertex position of interesting physics events measured in the ZEUS detector. Good events are selected using the following cuts:

- reconstructed event vertex;
- $E - p_z > 10.$ GeV;
- $E_T > 5.$ GeV;
- $RCAL\_time - FCAL\_time > -8$ ns;
- $P_T < 5.$ GeV;
- greater than 4 primary vertex tracks.

The beamspot is found by fitting the x, y and z distributions of the primary vertex every 2000 "good" events; all runs within the same HERA filling are treated as a single run. The vertex distributions in x, y and z are then plotted and fitted using a Gaussian.

The beamtilt is a measure of how the vertex x and y values vary with respect to the z value; this is obtained by a straight line fit through x/z and y/z plots. The beamspot and tilts are related with the equation:

$$x_{bsp} = x_{offset} + z_{bsp} \cdot tilt_x \tag{5.1}$$

The reasons to use B.S. instead of primary vertex as reference for the measure of the impact parameter are:

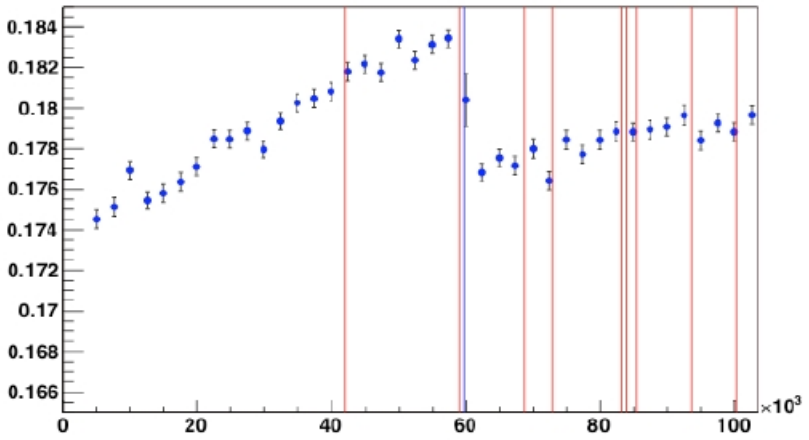

Figure 5.1: *Mean beam spot y position (cm) as a function of the event number recalculated every 2000 events. The vertical red lines represents a change of an HERA fill.*

- it is practically uncorrelated with the tracks in the actual event, furthermore gives an unbiased reference for decay lengths, while the primary vertex may be biased by other long-lived particles;

- its simulation is easier than the primary vertex one;

- its resolution is much better than the primary vertex one.

5.2 Calorimeter variables

The global calorimeter variables are calculated starting from the information regarding the cells. Isolated cells with energy below the noise threshold, 100 MeV for the electromagnetic cells and 150 MeV for the hadronic cells, are discarded.

Given E_i the energy measured in the i_{th} cell of the calorimeter, the total

calorimeter four-momentum (E, P_X, P_Y, P_Z) is defined as:

$$\begin{aligned} E &= \sum_i E_i \\ P_X &= \sum_i E_i sin\theta_i cos\phi_i \\ P_Y &= \sum_i E_i sin\theta_i sin\phi_i \\ P_Z &= \sum_i E_i cos\theta_i \end{aligned} \tag{5.2}$$

where θ_i and ϕ_i are the cell angles in a spherical coordinate system, centered in the reconstructed event vertex. The calorimeter transverse momentum can be written as $P_T = \sqrt{P_X^2 + P_Y^2}$. Another variable used at HERA is $E - P_Z = \sum_i E_i(1 - cos\theta_i)$ which, in the initial state, is equal to $2E_e$, E_e being the energy of the incoming electron beam. For energy conservation, if all the particles in the final state are detected by the calorimeter, $P_T \simeq 0$ and $E - P_Z \simeq 55\,\text{GeV}$. The quantity $E - P_Z$ is not sensitive to particles escaping the forward beam pipe, like the proton remnant. On the other hand, particle escaping detection close to the beampipe in the rear direction, carry away large $E - p_z$ giving a measured $E - p_z \ll 55.\text{GeV}$. DIS events have hence $E - p_z \approx 55.\text{GeV}$, while photoproduction events, for which the electron is lost in the rear direction have much lower values of $E - p_z$.

The total transverse energy, E_T, is defined as the scalar sum of the transverse energies of the calorimeter cells: $E_T = \sum_i E_i sin\theta_i$.

5.3 Electron identification

The electron identication is based on the fact that electrons or positrons, after being detected in the tracking detectors, release all their energy in the electromagnetic calorimeter. Here and later the term electron will refer to

both electron and positrons, as the analysis does not distinguish between the two. In this analysis the electron identication was performed using the EM electron-finder [64]. It uses both CAL and tracking information. EM calculates the likelihood for different variables to be originating from an electron, based on sample of electrons which were selected by other algorithms. The algorithm consists of three steps. First of all, cells with a local energy maximum are found and grouped to form a "cluster" together with the surrounding cells which have an energy deposit above the noise. Each cluster is treated as an electron candidate. The center of the cluster is obtained by weighting each tower of the cluster with a logarithmic function of the energy deposit. The polar angle of the deposit is calculated using the reconstructed vertex as center of the coordinate system. If the candidate electron is within the CTD acceptance, a matching track with $p_T^{trk} > 0.1$ GeV and distance of closest approach (DCA) to the beam line less than 2 cm is required. The DCA between the cluster and the extrapolation of the track to the calorimeter has to be lower than 50 cm.

In the second step, seven variables are calculated for each electron candidate. Four of them are related to the calorimeter energy deposit: the fraction of energy in the HAC layers, two parameters associated to the lateral energy profiles and the total energy of the calorimeter cells not associated to the cluster but lying within a cone of radius $R = \sqrt{(\Delta\eta)^2 + (\Delta\phi)^2)} = 0.8$ centered on the cluster. The last three parameters, which are used for the matching with the track, are the polar and azimuthal difference between the track and the cluster position and the quantity $1/E_{clu} - 1/p^{trk}$, being E_{clu} the energy of the cluster and p^{trk} the track momentum.

Finally, for each of the seven variables, a sub-probability is derived. The probabilities are then combined into a global probability P_e assuming that

the variables are not correlated. If the electron candidate is outside the CTD acceptance or if it has no matching track, only the calorimeter variables are taken into account to calculate th P_e. The global probability has values between 0 and 1 and it is higher for real electron candidates. For candidates electron in this analysis, the product of the likelihood was required to be greater than 0.001.

The electron energy is taken to be equal to the cluster energy since the CAL energy resolution is better than the CTD momentum resolution for tracks with $p_{trk} > 10.$ GeV. The electron polar and azimuthal angles are determined from the associated track or, in absence of it, from the calorimeter cluster position.

5.4 Muon identification

Muons, unlike electrons or hadrons, release only a small fraction of their energy into the calorimeter and are detected in the muon chambers. Their energy deposit in the calorimeter is that of a minimum ionizing particle (MIP).

There are several muon finding algorithms based on matching between the CTD track and the muon chamber track or between the CTD track and an energy deposit in the calorimeter compatible with a MIP. The muon finder used in this analysis is MV [65]. MV is an algorithm which matches CAL cell patterns to CTD tracks, using also HES and B/RMU informations for the identification of muons with energy $> 2.$ GeV. To identify muons, MV uses a phase space probability (*phase space probability function, PSPF*) trained on Monte Carlo simulations. The phase space has 8 dimensions whose coordinates are defined later in this paragraph. Calorimeter is subdivided into

three parts covering different ranges of polar angle: FCAL ($3^\circ < \theta < 37^\circ$), BCAL ($37^\circ < \theta < 129^\circ$) and RCAL ($129^\circ < \theta < 176^\circ$). Each part is divided into towers of $\approx 20 \times 20\,\mathrm{cm}^2$ in transverse size and segmented longitudinally into an electromagnetic section (EMC) and two hadronic sections (HAC1, HAC2) (one in RCAL), see Fig. 5.2. Calorimeter cells are grouped into is-

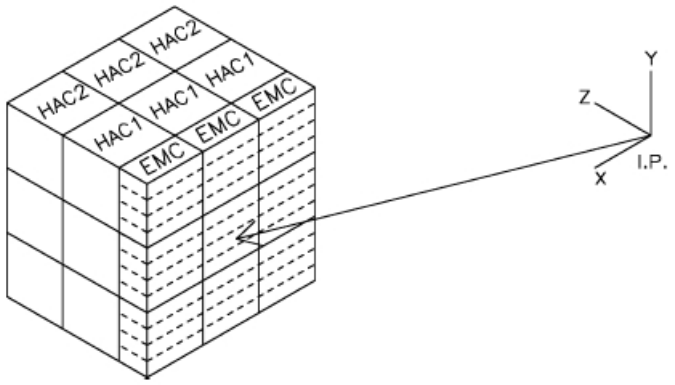

Figure 5.2: *The CAL structure.*

lands starting from the most energetic cell and attaching to it the non-zero energy adjacent cells. Found cells are removed and the procedure repeats. These groups are called Islands. The coordinates of the center of the island are the energy weighted sum of the coordinates of the constituent cells. Then islands are grouped into clusters whose energy is the energy of all the islands whose centers are inside a cone of angle 2α from the vertex at the interaction point. The clustering starts from the most energetic island. The angle α varies between $0^\circ < \alpha < 6^\circ$, depending on the inclination of the particle trajectory to the CAL surface.

The phase space is constituted by eight variables associated to the calorimeter clusters: θ, ϕ (polar and azimuthal angles of the cluster center), E_{emc}, E_{hac1}, E_{hac2} (the energy depositions in different CAL sections, see Fig. 5.3) and N_{emc}, N_{hac1}, N_{hac2} (number of cells in the calorimeter sections, see Fig.

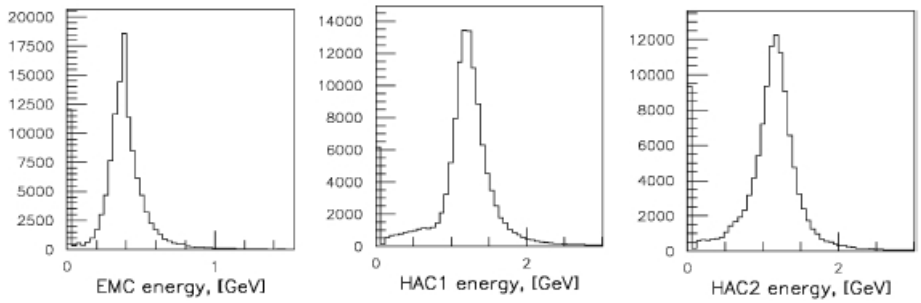

(a) *EMC energy* (b) *HAC1 energy* (c) *HAC2 energy*

Figure 5.3: *Energy deposition of simulated muons for different sections of the CAL.*

5.4). The eight-dimensional grid for the PSPF is built dividing the region

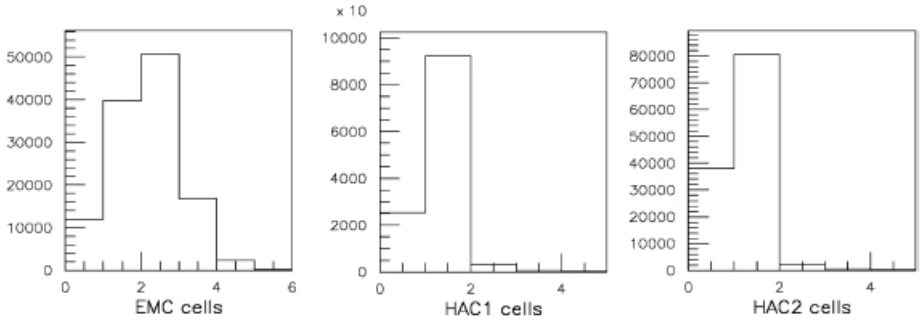

(a) *EMC cells* (b) *HAC1 cells* (c) *HAC2 cells*

Figure 5.4: *The number of cells with a signal in muon clusters.*

of each of the eight variables into equal intervals. A probability function is introduced and a probability is calculated in each box of the grid. In this analysis, muon candidates are selected requiring a PSPF probability greater than 0.6. Kinematical variables of the muon candidate, $(p^\mu, \theta^\mu, \phi^\mu)$, are taken from the track associated to the CAL cluster.

5.5 Jet finding

The energy deposition in the CAL were combined to jets with a cell-based inclusive $k_\perp$ algorithm [66, 67, 68]. The jet algorithm should fulfill the following requirements:

- collinear safety: the resulting jets have to be independent of one parton splitting into two partons moving collinearly. Translated to the experimental point of view, the jet algorithm has to be independent of one particle releasing energy in two adjacent CAL cells.
- infrared safety: the resulting jets have to be independent of the emission of very low energy particles. Experimentally, this is also related to the noise in the detector.
- correct treatment of beam remnants especially of the proton and eventually of the photon.
- Lorentz invariance: independence from longitudinal Lorentz boosts.

The jet transverse energy E_T and the position variables η_{jet} and ϕ_{jet} are defined as:

$$\begin{aligned} E_T^{jet} &= \sum_i E_{T,i} = \sum_i E_i sin\theta_i \\ \eta_{jet} &= \frac{\sum_i E_{T,i}\eta_i}{\sum_i E_{T,i}} \\ \phi_{jet} &= \frac{\sum_i E_{T,i}\phi_i}{\sum_i E_{T,i}} \end{aligned} \tag{5.3}$$

where the sum runs over all cells associated to the jet. $E_i, ET, \theta_i, \eta_i$ and ϕ_i are the energy, transverse energy, polar angle, pseudorapidity and azimuthal angle of cell i respectively.

The following steps are performed by the $k_\perp$ algorithm:

1. The starting point is a list of calorimeter objects; calorimeter cells above an energy threshold of 100 MeV for the electromagnetic section and 150 MeV for the hadronic section are used;

2. for each object i, the distance from the direction of the proton beam defined as $d_i = E_{Ti} \cdot R_0$ is calculated; the quantity R_0 is usually set to 1 and $E_{Ti} = E_i sin\theta_i$;

3. the distance d_{ij} between two objects is evaluated as:

$$d_{ij} = min[E_{Ti}, E_{Tj}] \cdot ((\eta_i - \eta_j)^2 + (\phi_i - \phi_j)^2);$$

4. if the smallest of all the d_i and d_{ij} quantities is a d_{ij}, the two objects i and j are grouped into a new object k wiht E_{Tk}, η_k, ϕ_k following the sum criteria:

$$\begin{aligned} E_{Tk} &= E_{Ti} + E_{Tj} \\ \eta_k &= \frac{E_{Ti}\eta_i + E_{Tj}\eta_j}{E_{Ti} + E_{Tj}} \\ \phi_k &= \frac{E_{Ti}\phi_i + E_{Tj}\phi_j}{E_{Ti} + E_{Tj}} \end{aligned} \tag{5.4}$$

5. if the smallest of all the d_i and d_{ij} quantities is a d_i, the i object is removed from the list of particles and added to the list of jets;

6. the procedure ends when no particle is left in the list of objects.

For this analysis jets with $-3. < \eta < 3.$ and transverse energy of at least 4.5 GeV have been selected.

5.5.1 Recombination scheme

Recombination schemes used by jet finders can influence the jet property during reconstruction, and in particular the corrections to hadronizations level. The most important are:

- Massless (p_T): the kinematic variables for the pseudo-particles are obtained by:

$$\begin{aligned} E_T^{jet} &= \sum_i E_{T,i} \\ \eta_{jet} &= \frac{\sum_i E_{T,i}\eta_i}{\sum_i E_{T,i}} \\ \phi_{jet} &= \frac{\sum_i E_{T,i}\phi_i}{\sum_i E_{T,i}} \end{aligned} \tag{5.5}$$

- Massive (E): this scheme reconstructs the jets as massive particles; this pseudo-particle is considered as a real particle with momentum $\vec{p} = \sum_i \vec{p_i}$ and energy $E = \sum_i E_i$. This is used for heavy flavour jet.

In our analysis, we use the massless recombination scheme.

Chapter 6

Search for isolated leptons

In this chapter we describe the search for events with isolated leptons, and large missing transverse momentum in the electron and muon channels and the following selection for single W and single top events. Electron and muon channels are treated separately.

6.1 Trigger requirements and rejection of non ep background

The analysis looks for events with isolated muons and missing transverse momentum so the selection has been made requiring CC triggers (triggers based on missing transverse momentum requirements) and muon triggers. The events have been selected by an online request of a logical OR of various triggers and, then, the same request of triggers has been applied to Monte Carlo simulation.

Trigger requirements

ZEUS has a three-level trigger system [1, 73] (see Section 1.10).

At the first level only coarse calorimeter and tracking information is available. Events were selected using criteria based on the energy, transverse energy and missing transverse momentum measured in the calorimeter. Generally, events were triggered with low thresholds on these quantities if a coincidence with CTD tracks from the event vertex occurred, while higher thresholds were required for events with no CTD tracks. Typical threshold values were 5 GeV (8 GeV) in missing transverse momentum, or 11.5 GeV (21 GeV) in transverse energy for events with (without) CTD tracks. At this level also informations from FMUON, B/RMUON and BAC are used to flag possible isolated muons.

At the second level, timing information from the calorimeter was used to reject events inconsistent with the bunch-crossing time. In addition, the topology of the CAL energy deposits was used to reject background events. In particular, a tighter cut of 6 GeV (9 GeV for events without CTD tracks) was made on missing transverse momentum, since the resolution in this variable is better at the second level than at the first level.

At the third level, full track reconstruction and vertex finding were performed and used to reject candidate events with a vertex inconsistent with an ep interaction. Cuts were applied to calorimeter quantities and reconstructed tracks to further reduce beam-gas contamination. At the third level, muon chambers and BAC informations are combined with the tracks of the central detector and with isolated deposits in the CAL compatible with a mip. Such muon TLT informations are used in the muon channel selection.

Since at HERA the W is mostly produced at low p_T, in the muon decay channel only a small fraction of events has a significant CAL missing p_T. This means that the CC triggers can select only the tail of the process with a significant hadronic p_T balancing the W. The use of muon triggers is hence

useful to extend the acceptance to low p_T^W and low p_T^{had}.

On the other hand, since the electron releases all its energy in the CAL, the CC triggers have large acceptance in this channel. The online selection in the electron channel has been made exploiting CC triggers at first, second and third level of trigger.

In the Figs. 6.1 and 6.2, we show the distributions of some true Monte Carlo kinematical variables from the decay process $W \rightarrow \mu\nu_\mu$ and the selection made by the different trigger types. The effect of the muon triggers to extend the acceptance to low p_T of the W and low hadronic p_T is clearly visible.

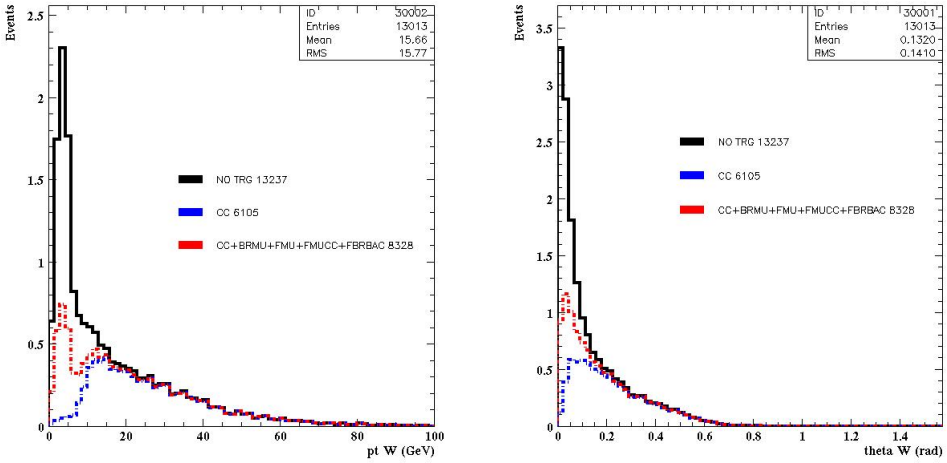

(a) p_T *of the* W (b) θ *of the* W

Figure 6.1: *(a) distribution of the* p_T *of the* W*; (b) distribution of the* θ *of the* W*. In black the full distribution, in blue the events selected by the CC triggers and in red the events selected by the OR logical chain.*

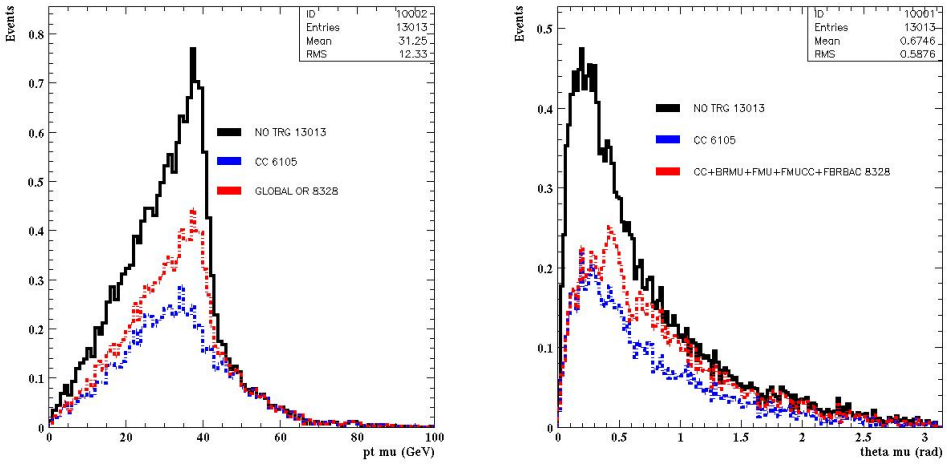

(a) p_T *of the* μ (b) θ *of the* μ

Figure 6.2: *(a) distribution of the* p_T *of the muon from the decay* $W \to \mu\nu_\mu$*; (b) distribution of the* θ_μ*. In black the full distribution, in blue the events selected by the CC triggers and in red the events selected by the OR logical chain.*

Rejection of non $e - p$ background

- *Beamgas rejection*

  Events originating from proton-beamgas interactions, usually have a large number of low-energy tracks associated to secondary vertices [69]. Therefore a cut is made comparing "good tracks" with the total number of tracks;

  $ngoodtracks > (ntracks - 20) \cdot 0.25$ where "good tracks" are defined as tracks with these characteristics:

  - primary vertex track;
  - $p_T > 0.3\,\text{GeV}$;
  - number of CTD superlayers passed > 2.

This cut has been tuned in the previous years of running and is extensively used in ZEUS analysis.

- *Calorimeter timing*

  The timing information from the CAL has been used to reject events from proton-beamgas interaction, which take place upstream the detector, see Fig. 6.3. t_f, t_r, t_b denote the average time in ns for CAL

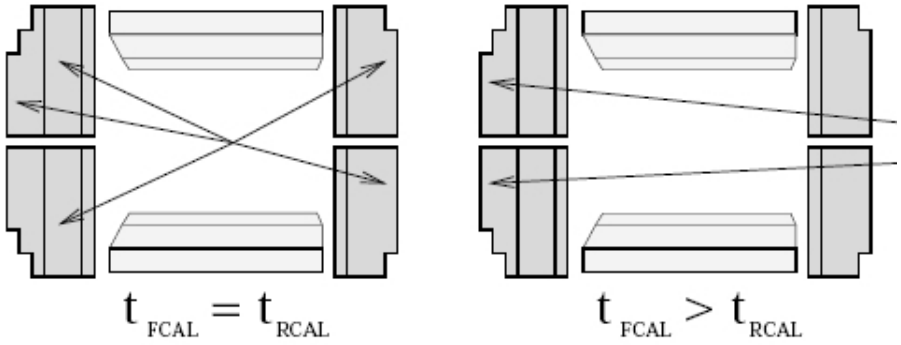

Figure 6.3: *Principle of using calorimeter timing information to reject non-ep events.*

  cells in the FCAL, BCAL, RCAL. All cells are calibrated such that the timing for relativistic particles originating from the nominal IP is close to 0 ns. Table 6.1 gives the cut values for the timing together with the minimum energy requirements in the different part of the CAL. These timing cuts have been applied only to the data events.

Cosmic rejection

The search for events with isolated muons requires the study of how to reject cosmic muons background. Fig. 6.4 shows the calorimeter timing in case of cosmic muon. We have selected a sample for cosmic rejection made by:

- events with only two primary vertex tracks;

Timing cut ns	Energy threshold GeV
$\mid t_f \mid < 6.$	$E_{FCAL} > 4.$
$\mid t_b \mid < 6.$	$E_{BCAL} > 4.$
$\mid t_r \mid < 6.$	$E_{RCAL} > 4.$

Table 6.1: *Timing cuts and minimal energy requirements for the different parts of the CAL.*

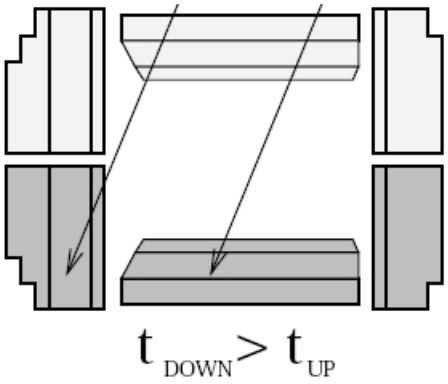

Figure 6.4: *Calorimeter timing up and down in case of cosmic.*

- at least one of them is a μ candidate from MV (see Section 5.4).

The selected sample is enriched of dimuon events, mainly J/ψ, and cosmics events. The cosmics have been rejected using cut on track impact parameter with respect to the beam spot and calorimeter timing. Fig. 6.5(a) shows the distribution of the angle between the two tracks; the peak close to -1. is due

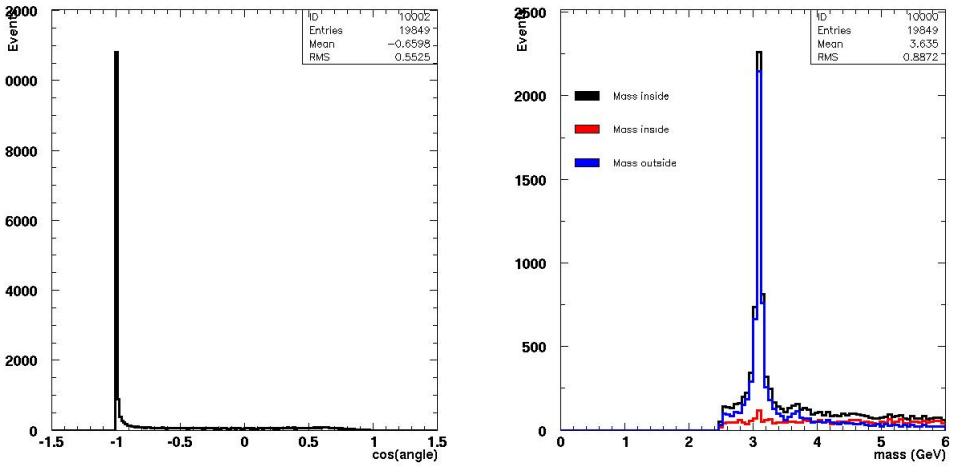

(a) *Distribution of the angle* (b) *Reconstructed dimuons mass*

Figure 6.5: *(a) distribution of the angle between the two tracks; the region with* $cos(\theta) \sim -1$. *is enriched of cosmics; (b) plot of the reconstructed mass: in blue mass the region* $cos(\theta) < -0.98$, *in red* $cos(\theta) > -0.98$.

to cosmics. The cut $cos(\theta) < (>) - 0.98$ is used to separate two samples: one enriched by dimuons from *ep* interactions (mainly J/ψ) and the other of cosmics. Fig. 6.5(b) shows the reconstructed mass, with the contributions of the two samples: dimuons and cosmics. Fig. 6.6(a) shows the track impact parameter for the two samples. Fig. 6.6(b) shows the difference between calorimeter timing in the up (t_u) and down (t_d) region[1] for the two samples.

[1] t_u and t_d are the timing measured in the upper ($0° < \phi < 180°$) and lower ($180° < \phi < 360°$) half of BCAL, respectively

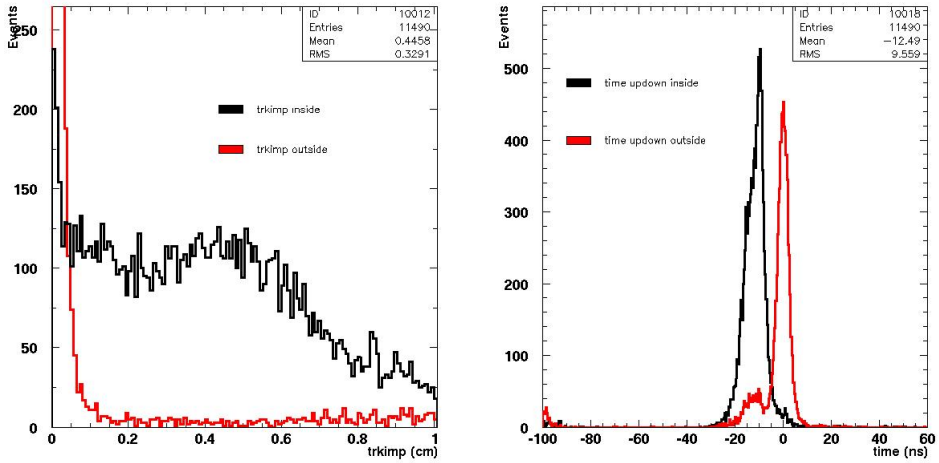

(a) *Track impact parameter* (b) *Calorimeter timing up-down*

Figure 6.6: *Plot of calorimeter timing up-down. In black sample of cosmics, in red sample of dimuons.*

In Fig. 6.7(b) is plotted the calorimeter timing $up - down$ after the cut of 0.05 on the track impact parameter; the fraction of cosmic sample (black one) is largely suppressed in comparison with the dimuons sample.

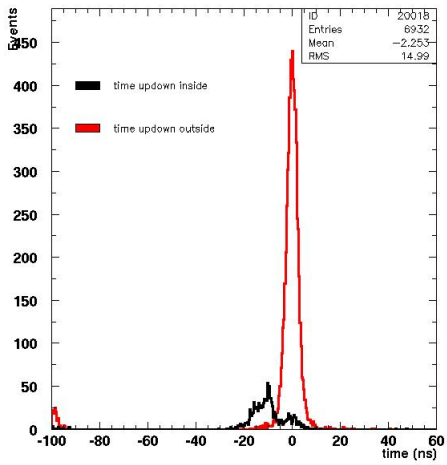

Figure 6.7: *Plot of calorimeter up-down timing after the cut on track impact parameter. In black sample of cosmics, in red sample of dimuons.*

The timing distribution, cleared up from cosmic contributions in this way, has been fitted with a Gaussian and then a range of $\pm 3\sigma$, respect to the mean value, has been choosen. The same method has been applied, respectively, for the timing up and down and for the data sample 04-05e. The values obtained are reported in the Table 6.2.

Period	Lepton beam	time up min/max (ns)	time down min/max (ns)	time up-down min/max (ns)
04-05	e^-	-5.3/4.3	-5.8/4.7	-6.8/6.9
06-07	e^+	-5.9/4.5	-6.4/5.0	-7.4/7.3

Table 6.2: *Values of the calorimeter timing used for cosmic rejection.*

6.2 Muon channel

6.2.1 Preselection

As reported in Section 5.4, the MV finder has been used for the muon identification. The following variables heve been used in the analysis:

- p_T, transverse momentum of the muon;
- P_T, transverse momentum defined as $P_T = \sqrt{(\sum_i P_{X,i})^2 + (\sum_i P_{Y,i})^2}$ where $P_{X,i} = E_i sin\theta_i cos\phi_i$ and $P_{Y,i} = E_i sin\theta_i sin\phi_i$ with E_i, θ_i, ϕ_i energy, polar angle and azimuthal angle of the i_{th} calorimeter cell with respect to the reconstructed primary vertex. The four momentum associated to each cell is $(E_i, E_i sin\theta_i cos\phi_i, E_i sin\theta_i sin\phi_i, E_i cos\theta_i)$ and the sum of each cell of the calorimeter gives the total calorimeter

four momentum. A muon leaves an energy deposit in the calorimeter which is that of a minimum ionizing particle so the P_T must be corrected by using the impulse of the muon coming from its track: $P_T^{corr} = \sqrt{(\sum_i P_{X,i} + p_x^\mu)^2 + (\sum_i P_{Y,i} + p_y^\mu)^2}$. Signal events would contain one neutrino in the final state, leading to a missing transverse momentum in the detector;

- the hadronic P_T^{had}, defined as before but restricted to calorimeter cells attributed to the hadronic deposits (i.e. removing cells associated to eventual candidates from the EM finder);

- $E-p_z$, for events fully contained in the detector and for the conservation of the longitudinal momentum this variable peaks at 55. GeV; in case of photoproduction events, where the electron is scattered at low θ remaining in the beampipe and escaping the detector, this quantity is much lower. Values much bigger than 55. GeV are usually caused by non-ep events;

- isolation of the muon candidate; distance between the muon track and other tracks and jets in the event has been eveluated in the (η, ϕ) plane as:
  $\Delta R_{\mu,trk} = \sqrt{(\phi_{trk} - \phi^\mu)^2 + (\eta_{trk} - \eta^\mu)^2}$ and
  $\Delta R_{\mu,jet} = \sqrt{(\phi_{jet} - \phi^\mu)^2 + (\eta_{jet} - \eta^\mu)^2}$

- the transverse mass; defined as:

$$M_T = \sqrt{2 P_T^\mu P_T^{corr} (1 - cos\phi_{\mu\nu})}$$

  where P_T^μ is the transverse momentum of the muon, P_T^{corr} is the missing transverse momentum in the events and $\phi_{\mu,\nu}$ is the angle between the missing transverse momentum and the muon, see Fig. 6.8;

- acoplanarity, (see Fig. 6.8); defined as the azimuthal separation be-

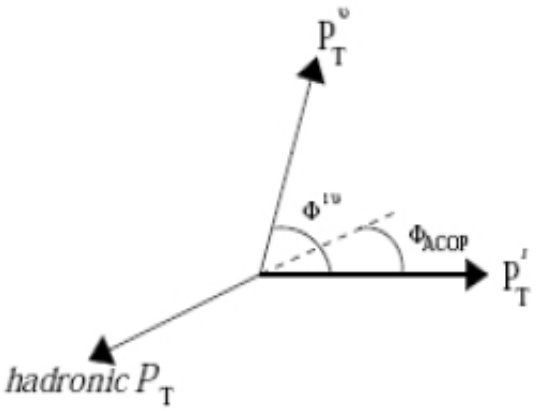

Figure 6.8: *The acoplanarity angle ϕ_{acop}; in the figure is shown even the angle between the missing transverse momentum and the muon $\phi_{l\nu}$, the transverse momentum of the neutrino P_T^{ν}, of the lepton P_T^{l} and hadronic P_T.*

  tween the muon and the vector which balances the hadronic transverse momentum. NC events, for which the hadronic system is balanced by the diffused electron in the transverse plane, have low values of acoplanarity.

The following preselection cuts have been applied to obtain a sample of isolated muons events and verify the agreement between Data and Monte Carlo:

- timing cuts for cosmic rejection (only for data) and tracks cuts for beamgas rejection (see Section 6.1);
- absolute value of the z coordinate of the event vertex $\mid zvtx \mid < 30.cm$;
- $E - p_z < 70.$ GeV;
- $p_T > 5.$ GeV in order to suppress photoproduction background;

- a muon candidate from MV with $p_{T,\mu} > 8.\,\text{GeV}$;
- μ track from primary vertex and isolated from other tracks, $\Delta R_{\mu,trk} > 0.5$;
- μ isolated from jets, $\Delta R_{\mu,jet} > 0.5$;

Preselection plots

In this section we compare Data and MC after the preselection for the muon channel. Data samples 2004-2005(e^-p) and 2006-2007(e^+p) are shown separately. Figs. 6.9-6.14 show the distribution of several muon and global event variables. Black dots are data, red is the contribute from dimuons, green is the contribute from NC, purple from ditaus, yellow from CC and blue is the contribute from W signal.

The preselection plots show an acceptable agreement between Data and Monte Carlo. The distributions exhibit the typical characteristics of dimuon events: low p_T^μ and $E - p_z$, acoplanarity peaked at 0 and low values of p_T^{miss}.

After the preselection cuts the sample selected is reported in the Table 6.3, the reported errors on the expected events from SM processes are statistical only (see Section 6.4). The most relevant sources of systematic errors are discussed in Section 6.4.

6.3 Electron channel

In the electron channel, events useful for the analysis have been collected using a CC trigger. The variables defined for the muon selection in Section 6.2.1 have been used also in the electron channel with the difference that the lepton, in this case, is the electron.

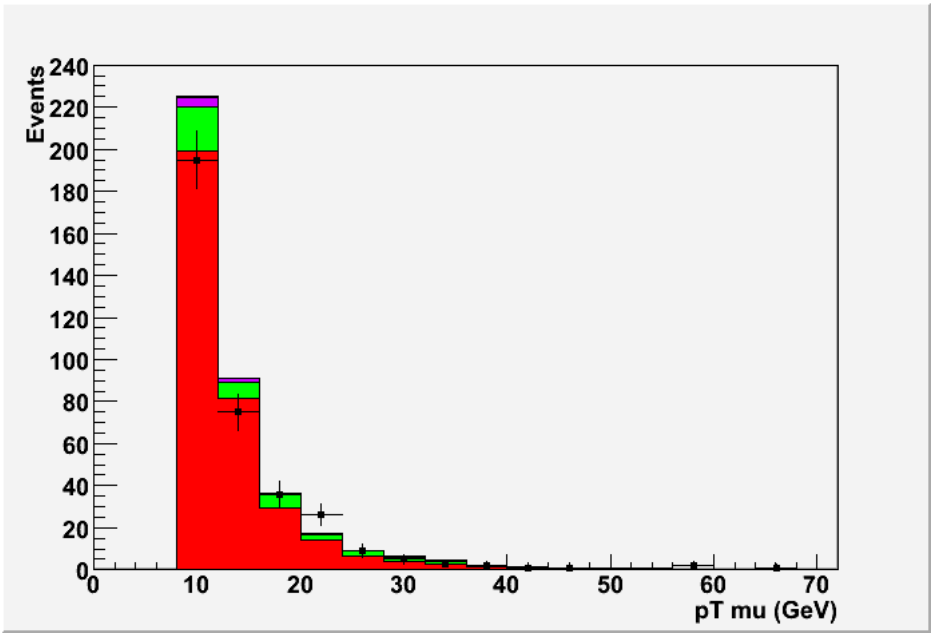

(a) p_T *of the muon 04-05*

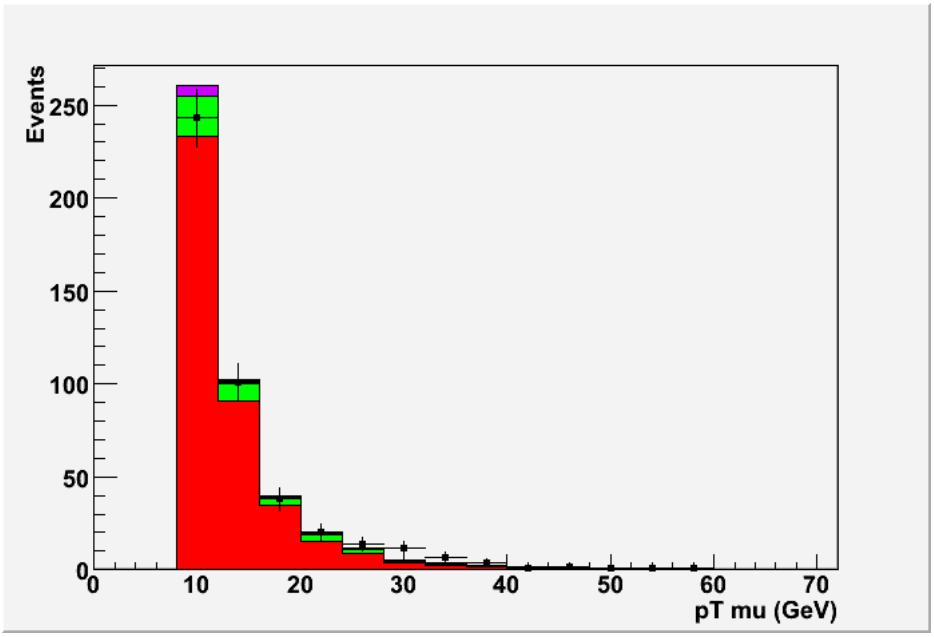

(b) p_T *of the muon 06-07*

Figure 6.9: *Plots of the transverse momentum of the muon.*

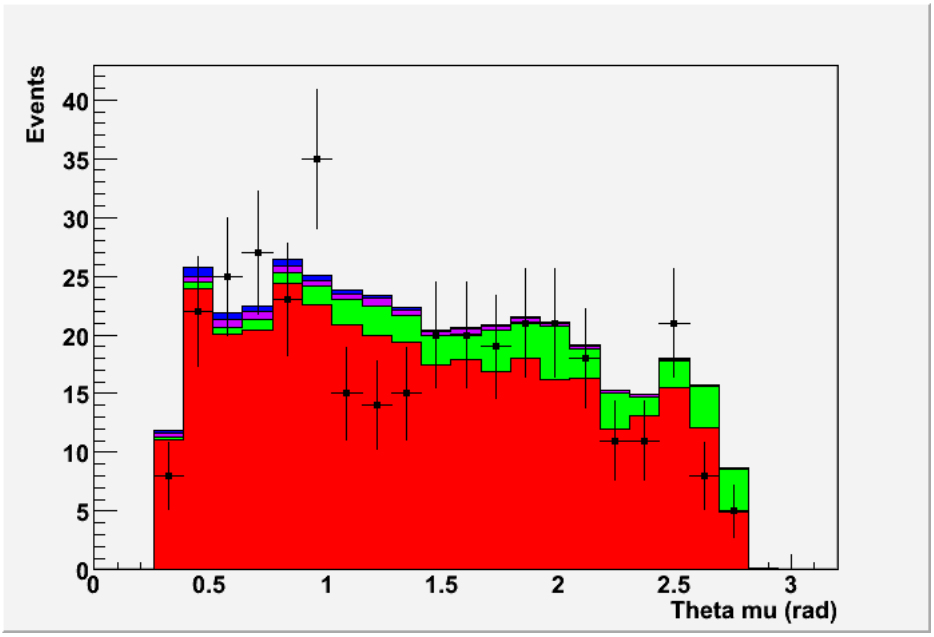

(a) *θ of the muon 04-05*

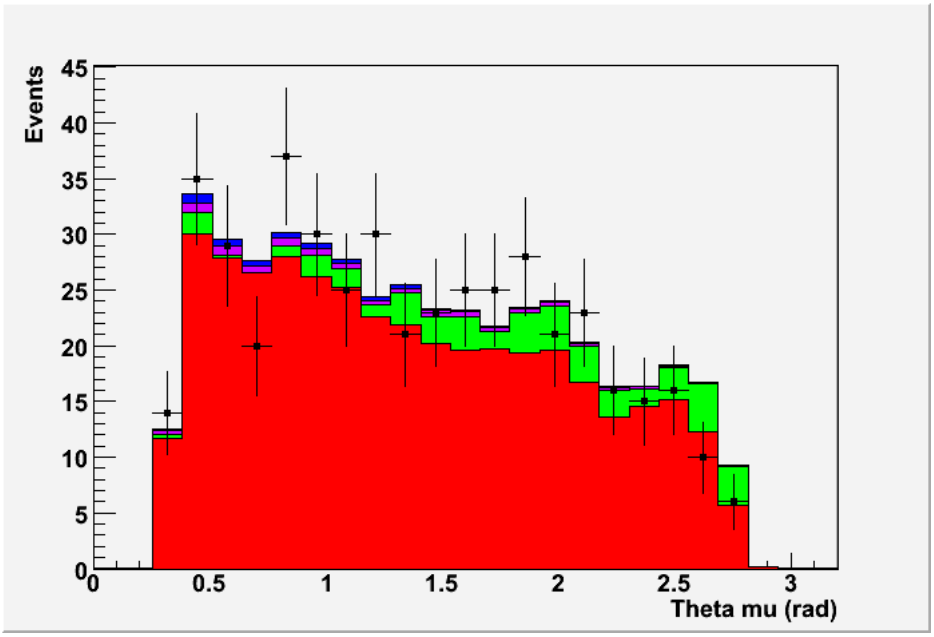

(b) *θ of the muon 06-07*

Figure 6.10: *Plots of the θ of the muon.*

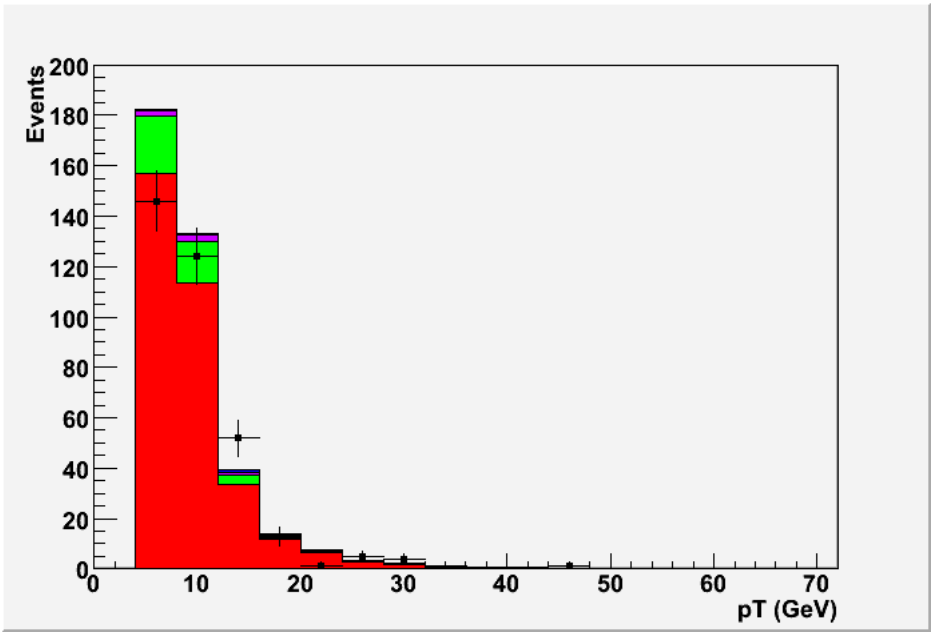

(a) p_T^{corr} *04-05*

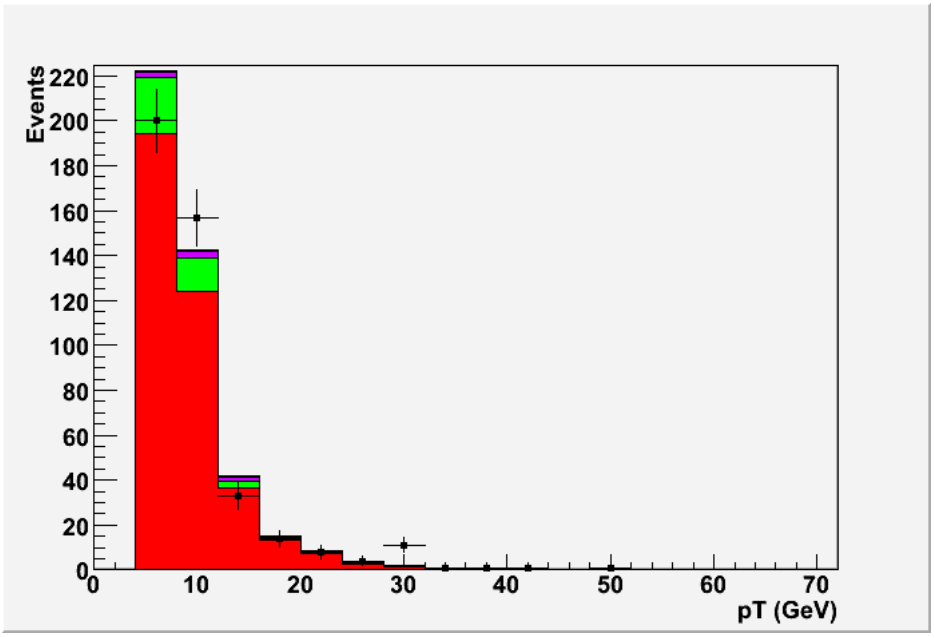

(b) p_T^{corr} *06-07*

Figure 6.11: *Plots of the missing transverse momentum.*

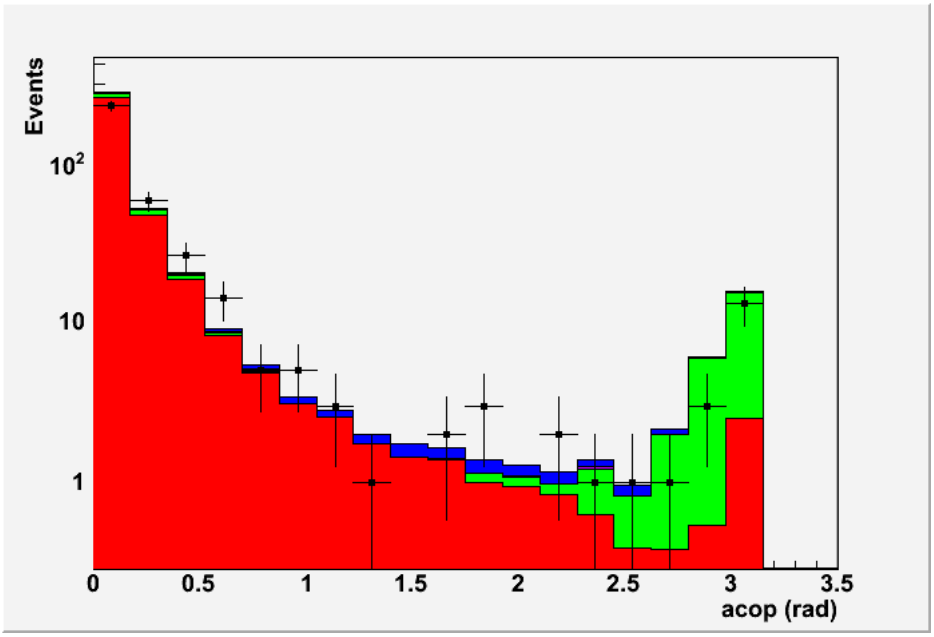

(a) *acoplanarity 04-05*

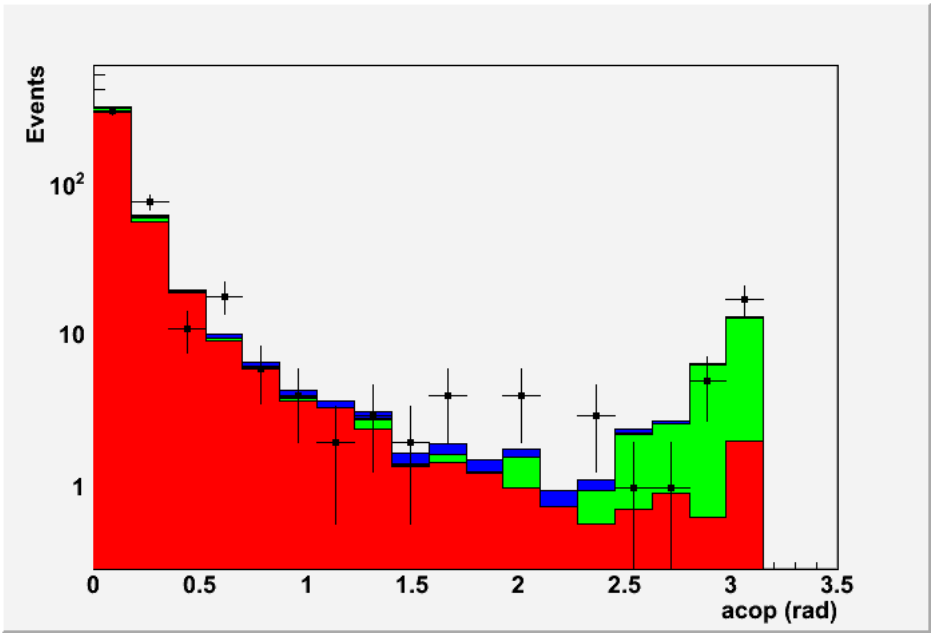

(b) *acoplanarity 06-07*

Figure 6.12: *Plots of the acoplanarity.*

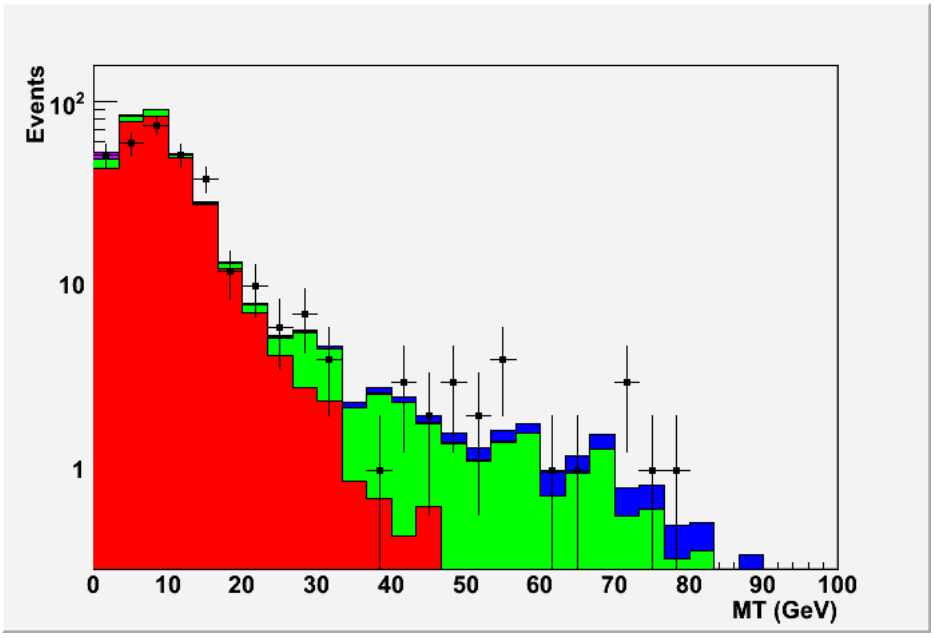

(a) M_T *04-05*

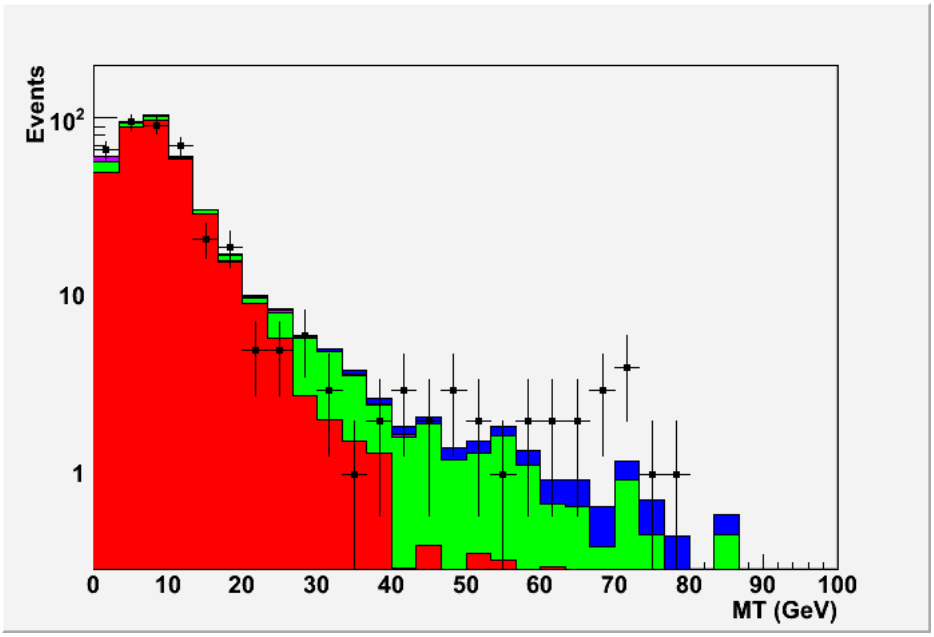

(b) M_T *06-07*

Figure 6.13: *Plots of transverse mass.*

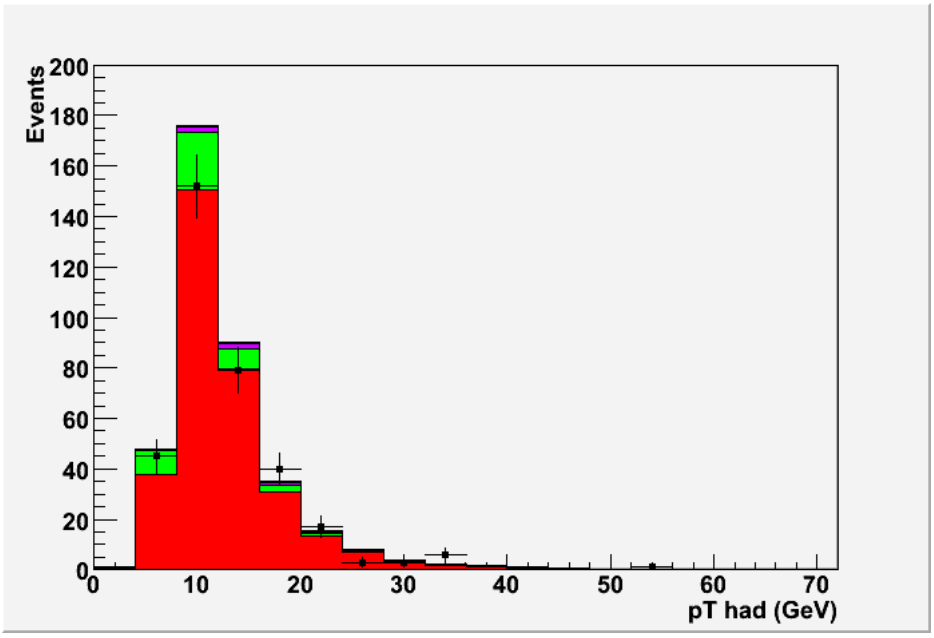

(a) p_T *hadronic 04-05*

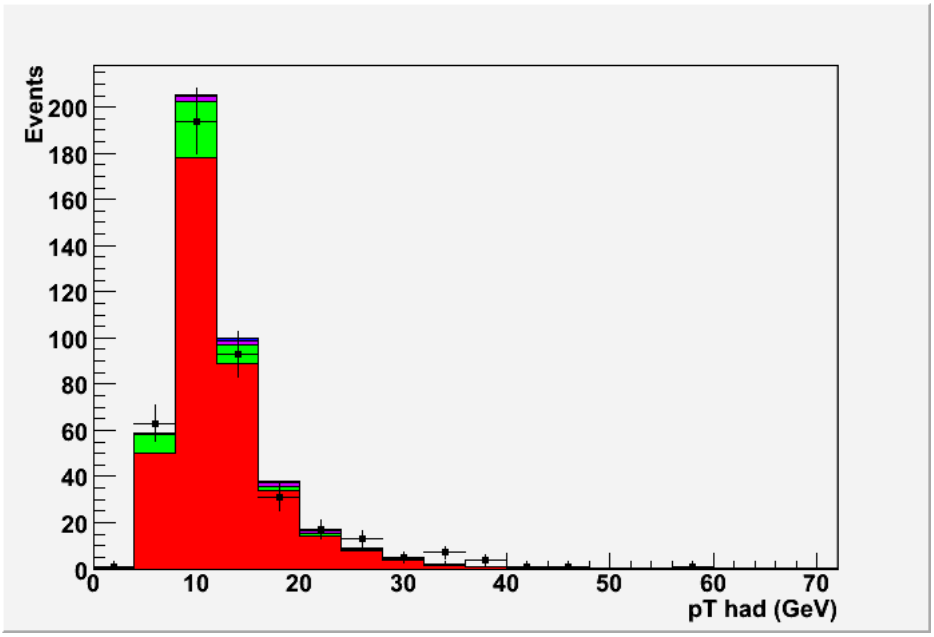

(b) p_T *hadronic 06-07*

Figure 6.14: *Plots of the transverse hadronic momentum.*

Period	Data	Total Monte Carlo	W	NC	CC
04-05 (e^-p)	347	385.20 ± 3.78	4.56 ± 0.07	44.07 ± 2.54	0. ± 0.
				Dimuon	Ditau
				328.93 ± 2.78	7.65 ± 0.31
Period	Data	Total Monte Carlo	W	NC	CC
06-07 (e^+p)	431	438.85 ± 4.26	5.14 ± 0.09	43.51 ± 2.88	0.05 ± 0.04
				Dimuon	Ditau
				381.71 ± 3.12	8.43 ± 0.35

Table 6.3: *Selected events from the sample 04-05e^- and 06-07e^+ after preselection cuts in the muon channel. Uncertainties in the Table are statistical only.*

6.3.1 Preselection

The following cuts have been applied to select a sample of events with a high-p_T electrons and missing p_T:

- timing cuts (only for data) and tracking cuts for beam gas rejection (see Section 6.1);
- $\mid zvtx \mid < 30.$ cm;
- $p_T > 10.$ GeV;
- $5. < E - p_z < 60.$ GeV;
- EM candidate with $p_T^{el} > 10.$ GeV and $0.3 < \theta_{el} < 2.rad$;
- electron track isolated from other tracks in the event $\Delta R_{e,trk} > 0.5$;
- electron isolated from other jets in the event, $\Delta R_{el,jet} > 0.5$;

- the track associated to the electron should have a distance of closest approach to the CAL deposit
  $DCA_{el} < 10.\,\text{cm}$ and $p_T > 5.\text{GeV}$;

- $M_T > 10.\,\text{GeV}$ in order to remove bad reconstructed NC events with large p_T^{miss} along the electron.

Preselection plots

In this section we compare Data and MC after the preselection for the electron channel. Data samples 2004-2005($e^- p$) and 2006-2007($e^+ p$) are shown separately. Figs. 6.15-6.20 show the distribution of several electron and global event variables. Black dots are data, red is the contribute from dielectrons, green is the contribute from NC, purple from ditaus, yellow from CC and blue is the contribute from W signal.

The preselection plots show an acceptable agreement between Data and Monte Carlo. The main background is due to NC DIS events. The distribution of $E - p_z$ shows a peak at $55.\,\text{GeV}$ as expected for NC DIS events. The data events around $E - p_z > 60.\,\text{GeV}$ are due to fluctuations in energy measurement by BCAL and RCAL giving unphysical values; these fluctuations are not well reproduced in the Monte Carlo. The p_T falls off steply as expected from NC DIS events where the apparent missing transverse momentum is caused by measmesurements. The acoplanarity peaks at low values as expected from NC DIS where the electron and the hadronic system are back to back in the transverse plane. The transverse mass, reconstructed from the p_T^{el} and the p_T^{miss}, has a maximum at the W mass for the signal while data events at very low transverse mass are caused by NC events in which a bad reconstructed p_T^{had} or p_T^{el} gives a p_T^{miss} in the direction of the electron.

After the preselection cuts the sample selected is reported in the Table 6.4,

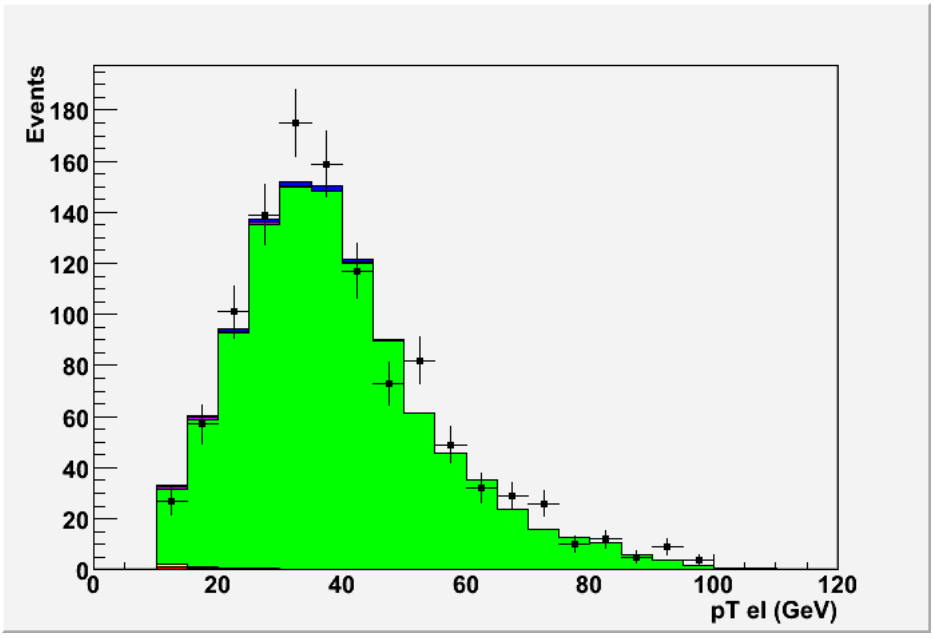

(a) p_T *of the electron 04-05*

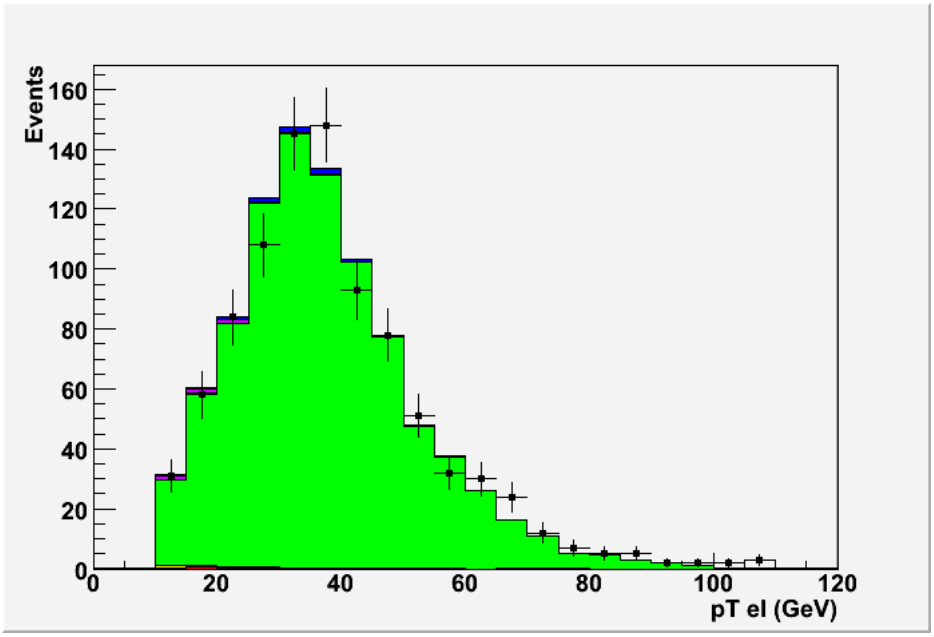

(b) p_T *of the electron 06-07*

Figure 6.15: *Plots of the transverse momentum of the electron.*

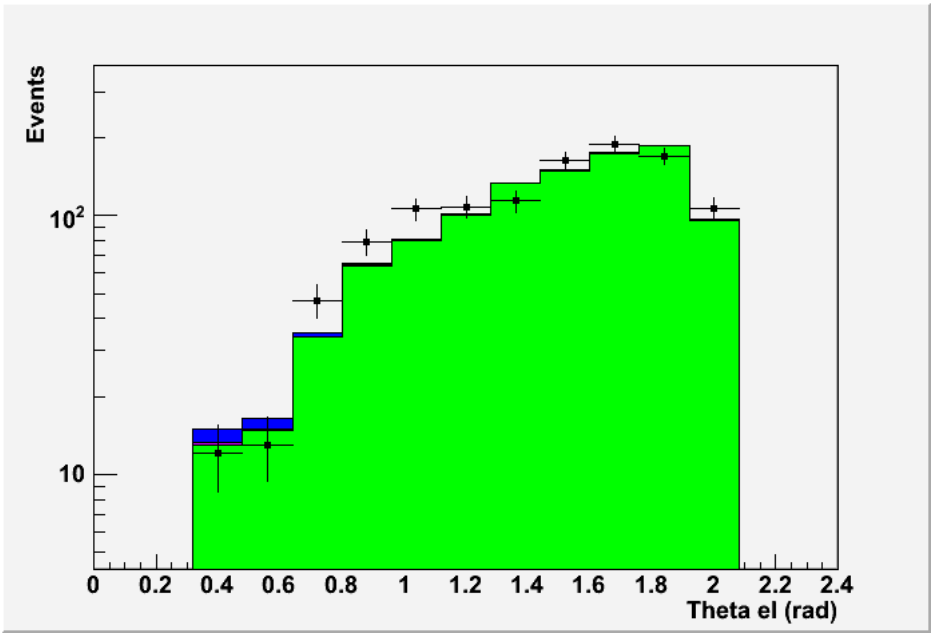

(a) *θ of the electron 04-05*

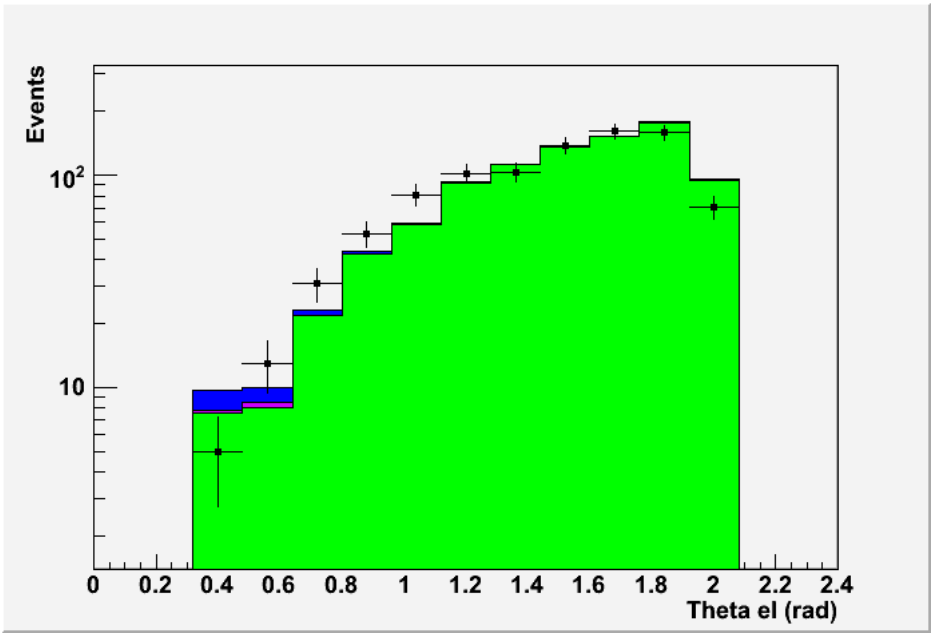

(b) *θ of the electron 06-07*

Figure 6.16: *Plots of the θ of the electron.*

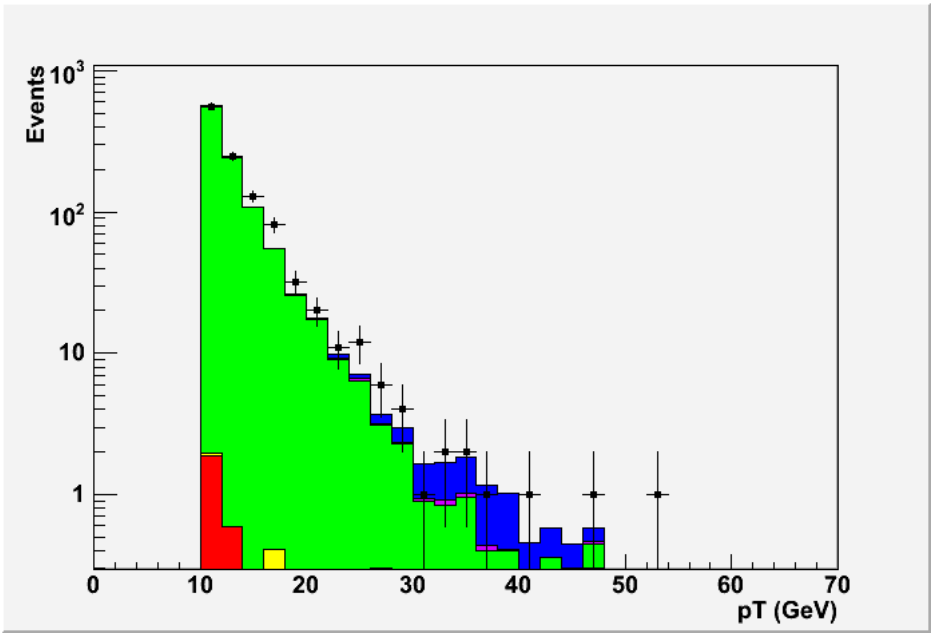

(a) p_T *missing 04-05*

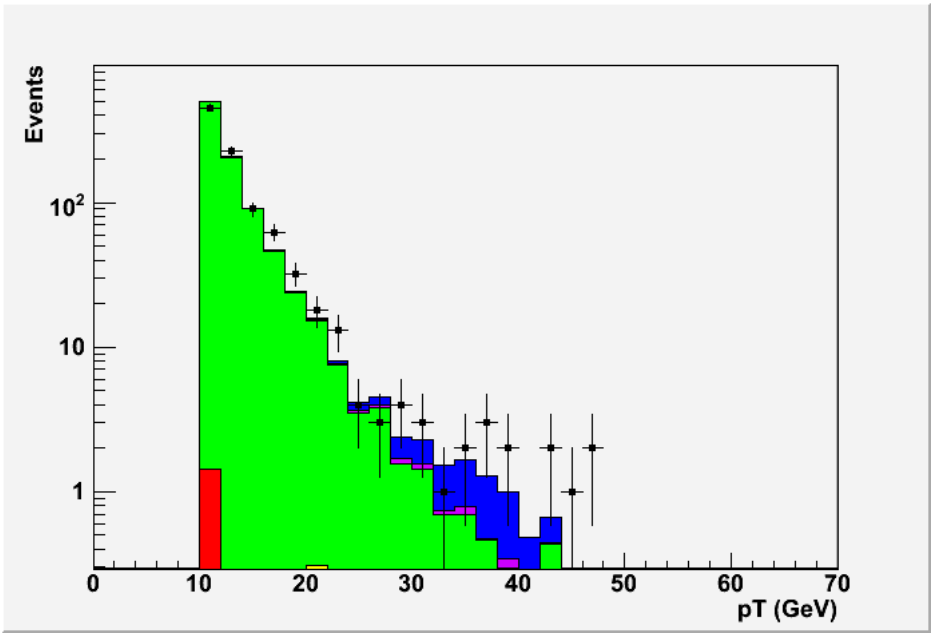

(b) p_T *missing 06-07*

Figure 6.17: *Plots of the missing transverse momentum.*

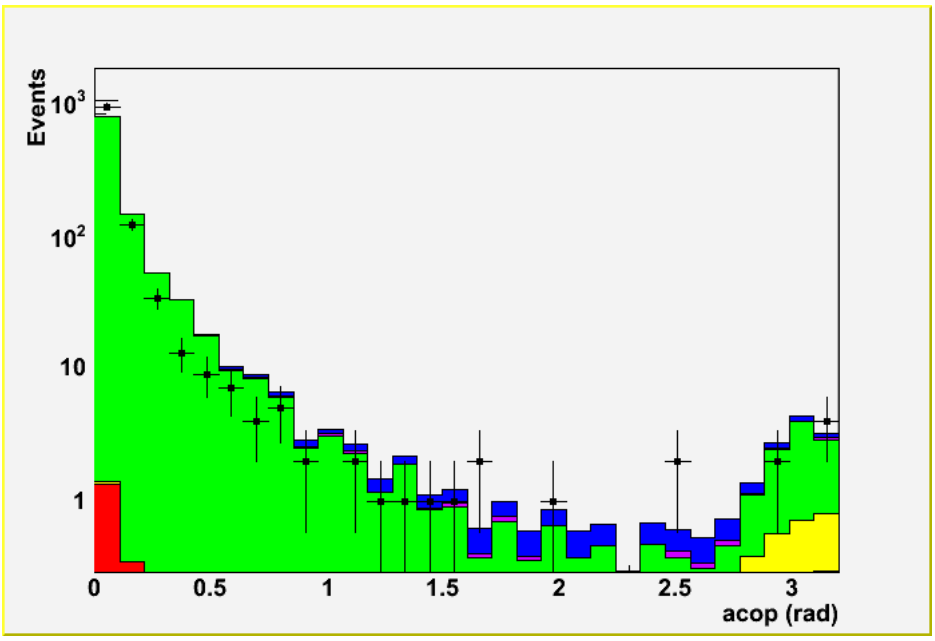

(a) *acoplanarity 04-05*

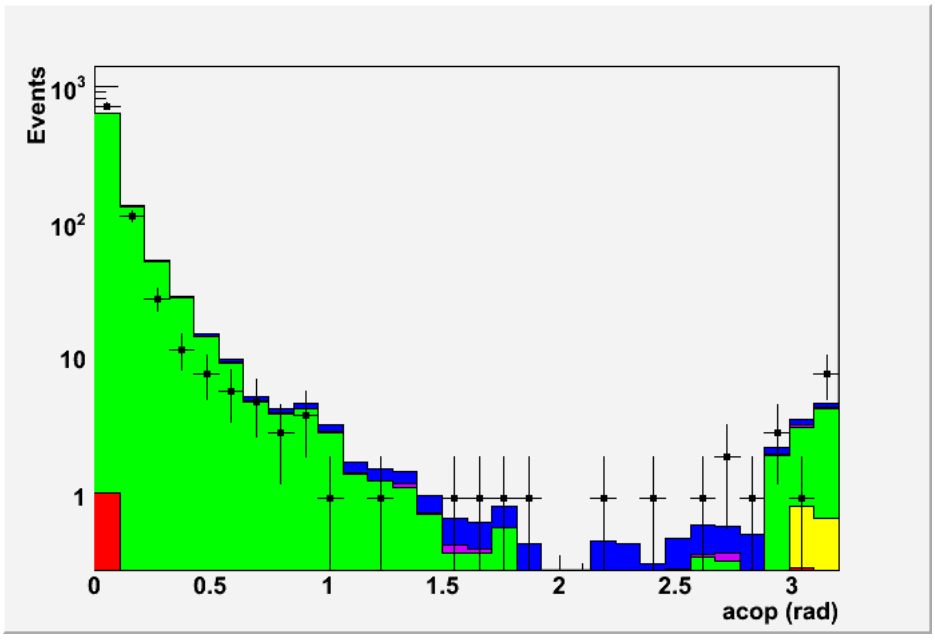

(b) *acoplanarity 06-07*

Figure 6.18: *Plots of the acoplanarity.*

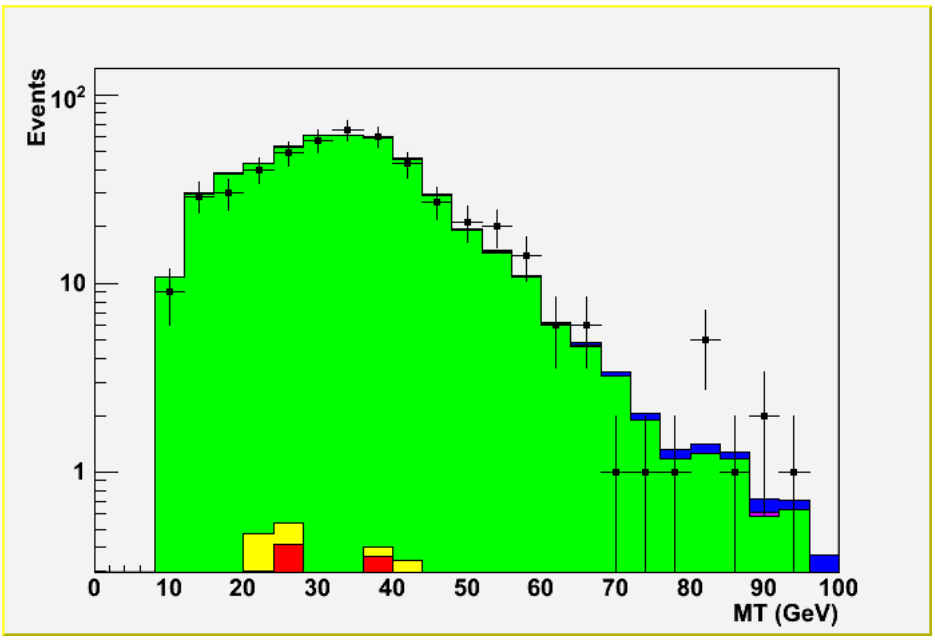

(a) M_T *04-05*

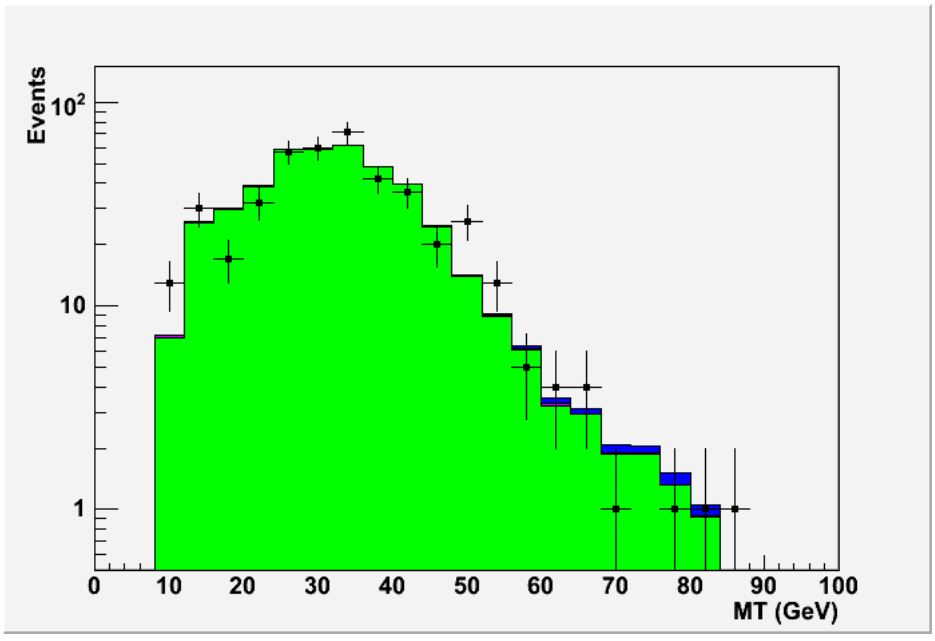

(b) M_T *06-07*

Figure 6.19: *Plots of transverse mass.*

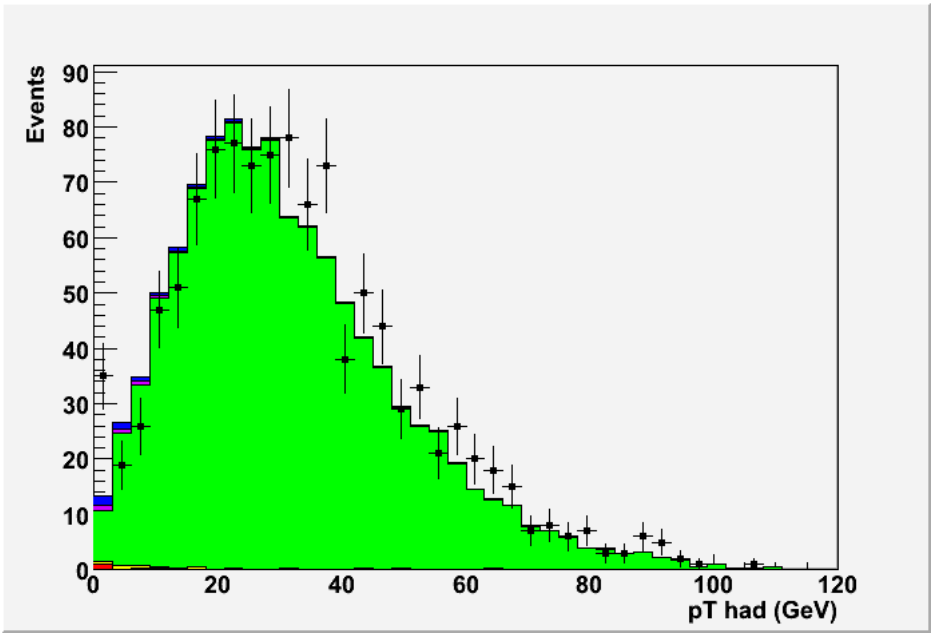

(a) p_T *hadronic 04-05*

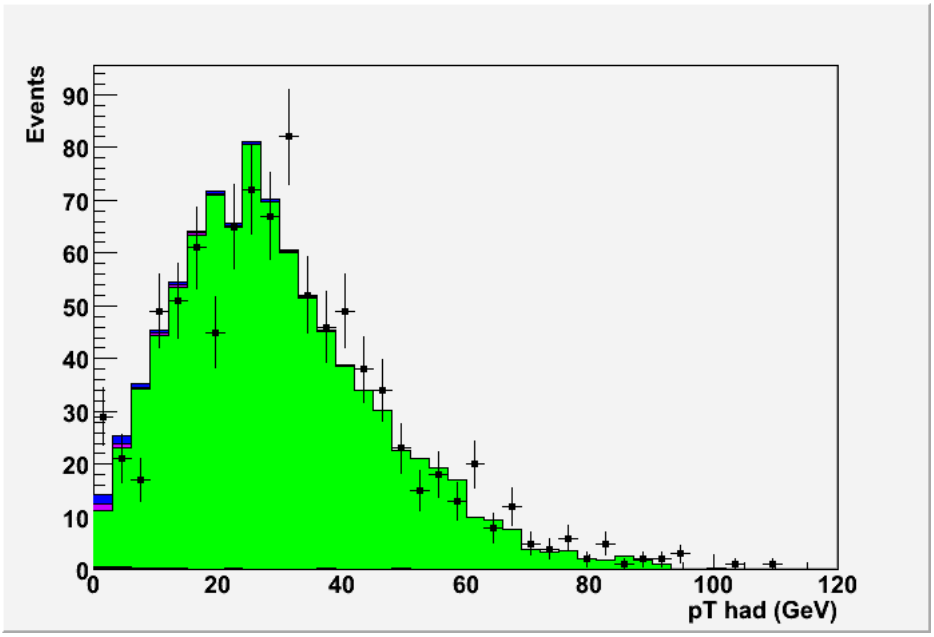

(b) p_T *hadronic 06-07*

Figure 6.20: *Plots of the transverse hadronic momentum.*

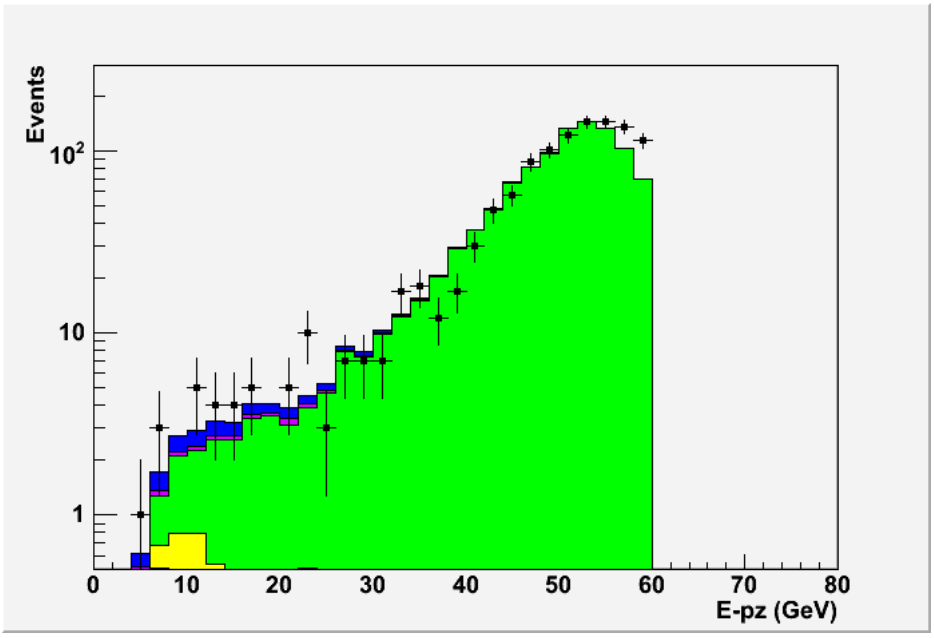

(a) $E - p_z$ *04-05*

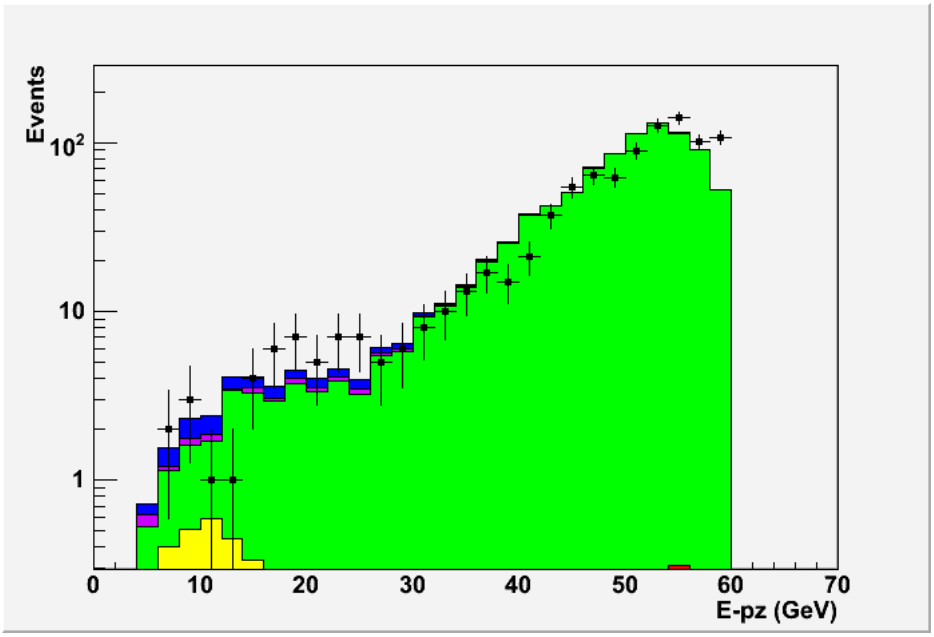

(b) $E - p_z$ *06-07*

Figure 6.21: *Plots of the* $E - pz$.

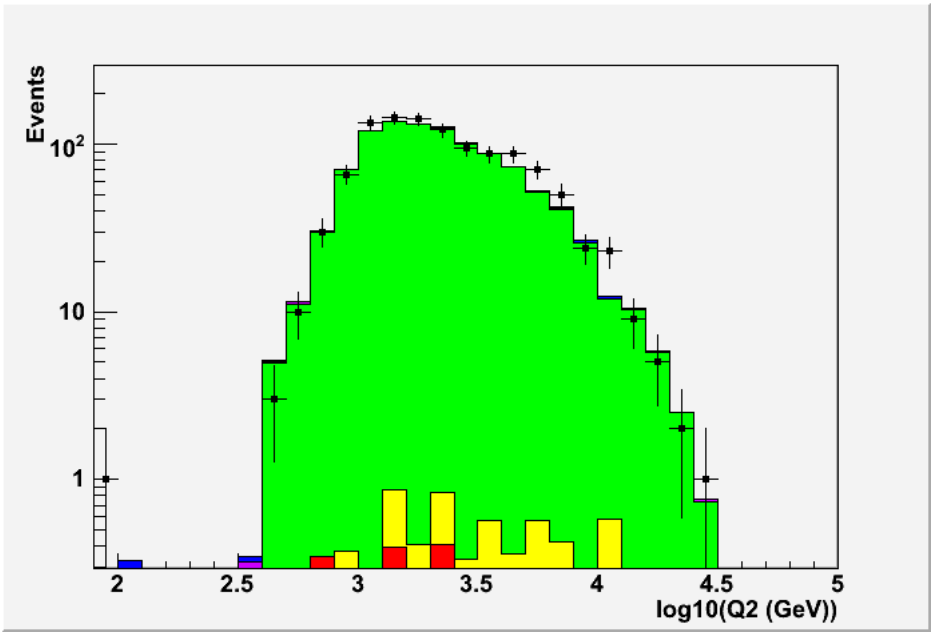

(a) *log*(Q^2) *04-05*

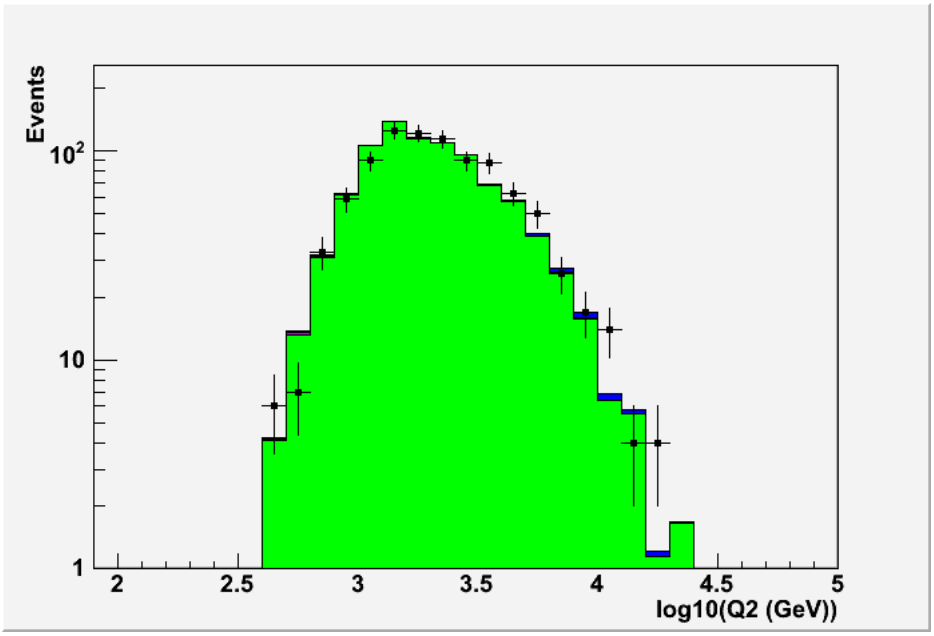

(b) *log*(Q^2) *06-07*

Figure 6.22: *Plots of the log*(Q^2).

the reported errors on the expected events from SM processes are statistical only (see Section 6.4). The most relevant sources of systematic errors are discussed in Section 6.4.

Period	Data	Total Monte Carlo	W	NC	CC
04-05 (e^-p)	1107	1056.80 ± 12.34	8.61 ± 0.08	1036.43 ± 12.32	4.19 ± 0.42
				Diel	Ditau
				2.88 ± 0.50	4.69 ± 0.28
Period	Data	Total Monte Carlo	W	NC	CC
06-07 (e^+p)	919	917.17 ± 12.89	8.95 ± 0.11	898.94 ± 12.88	2.47 ± 0.24
				Diel	Ditau
				1.89 ± 0.39	4.91 ± 0.29

Table 6.4: *Selected events from the sample 06-07e^+ and 04-05e^- after preselection cuts in the electron channel. Uncertainties in the table are statistical only.*

6.4 Statistical and systematic uncertainties

The statistical uncertainties, σ_{stat} for the MC samples have been obtained adding in quadrature the individual statistical uncertainties of the single MC samples.

$$\sigma_{stat} = \sqrt{\sum_i N^i_{MC,sel} \left(\frac{\mathcal{L}_{data} \sigma^i_{MC}}{N^i_{MC,tot}} \right)^2}$$

where i runs over all MC samples, $N^i_{MC,tot}$, $N^i_{MC,sel}$ and σ^i_{MC} are the total number of events, the number of selected events and the cross section of the i_{th} MC sample and $\mathcal{L}_{data}$ is the luminosity of the data taking period.

The following sources of systematic uncertainties have been considered:

- calorimeter energy scale: the uncertainty in the absolute energy scale of the calorimeter is 2% for the electromagnetic section and 3% for the hadronic section. Such uncertainties give a contibution for the number of preselected events in both electron and muon channels of $^{+11\%}_{-8\%}$ (hadronic scale) and $^{+13\%}_{-11\%}$ (em scale);

- QCD radiation model for NC and CC DIS background; the use of LEPTO MEPS instead of ARIADNE CDM for the simulation of the NC and CC DIS background has been considered as a systematic source of uncertainty; its contribute is equal to -11% for the preselected events in the electron channel;

- luminosity; integrated luminosity is known with a systematic uncertainty of 2.6% for e^-p collisions and 3.0% for e^+p collisions;

- muon triggers: the selection efficiency of the muon triggers has an uncertainty of 10%;

The total sytematic uncertainty, obtained adding in quadrature the above sources leads to a total systematic on the number of preselected events of $^{+17\%}_{-18\%}$ for the electron channel and $^{+17\%}_{-14\%}$ for the muon channel. In Fig. 6.23 is shown, as an example, the distribution of the $E - p_z$ for the electron channel after the preselection with the inclusion of systematic uncertainties (yellow band). The systematic uncertainties account for the discrepancy between Data and MC at large $E - p_z$.

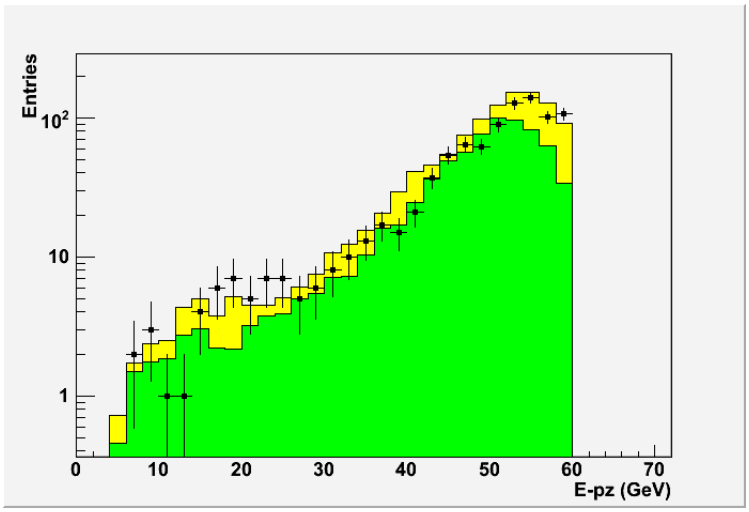

Figure 6.23: *Plot of $E - p_z$; black dots are data and in yellow the area of systematic unertainties.*

6.5 W selection

After the preselection the cuts have been optimized to select a W sample from the preselected data.

A cut optimization has been performed respectively in the electron and muon channel using the Monte Carlo signal and background, in order to maximize the expected ratio $N_{sig}/(\sqrt{N_{sig} + N_{bkg}})$, where N_{sig} is the number of W events and N_{bkg} is the contributions from the other SM processes.

In the electron channel, the optimization for the variables acoplanarity, $E - p_z$ and p_T^{miss} leaded to the following selection cuts:

- $p_T^{miss} > 20.\,\text{GeV}$;
- $E - p_z < 36.\,\text{GeV}$;
- $0.1 <$ acoplanarity $< 0.5\,rad.$

In the muon channel, the optimization was performed on the acoplanarity,

and M_T leading to the following selection:

- $M_T > 40.\,\mathrm{GeV}$;
- $0.2 <$ acoplanarity $< 2.5\,rad.$

The Table 6.5 summarize the results of the selection; uncertainties in the Table are statistical only.

Period	Lepton channel	Data	Total Monte Carlo	W MC	$N_{sig}/(\sqrt{N_{sig}+N_{bkg}})$
04-05e^-	e	6	10.49 ± 0.70	4.73 ± 0.07	1.38
06-07e^+	e	8	8.85 ± 0.62	4.98 ± 0.09	1.71
04-05e^-	μ	5	5.71 ± 0.52	2.73 ± 0.06	1.14
06-07e^+	μ	5	4.87 ± 0.34	3.03 ± 0.07	1.37

Table 6.5: *Selected W events from the sample 06-07e^+ and 04-05e^- in the muon and electron channels; uncertainties in the table are statistical only.*

Figs. 6.24, 6.25 and 6.26 show the comparison between Data and MC for p_T^{had}, M_T and p_T^{miss} respectively. Black dots are data, black histogram the total expected SM prediction, red is the W signal and blue is the single top in arbitrary normalisation.

Two selected events (one for each channel) are shown in see Figs. 6.27, 6.28.

The results show a full compatibility between data and SM expectation. Since there is no evidence of extra W production, we proceed to evaluate limits for single top at HERA.

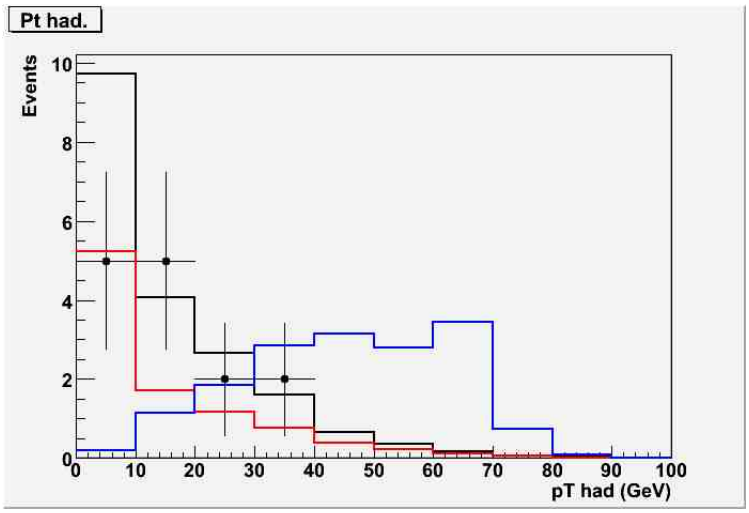

(a) p_T^{had}

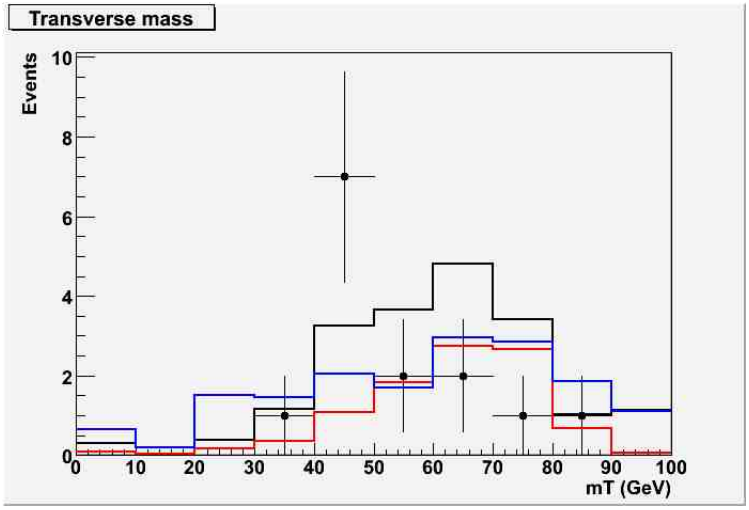

(b) M_T

Figure 6.24: *Plots of the p_T^{had} and M_T in the electron channel; black dots are data, black histogram the total expected SM prediction, red is the W signal and blue is the single top in arbitrary normalisation.*

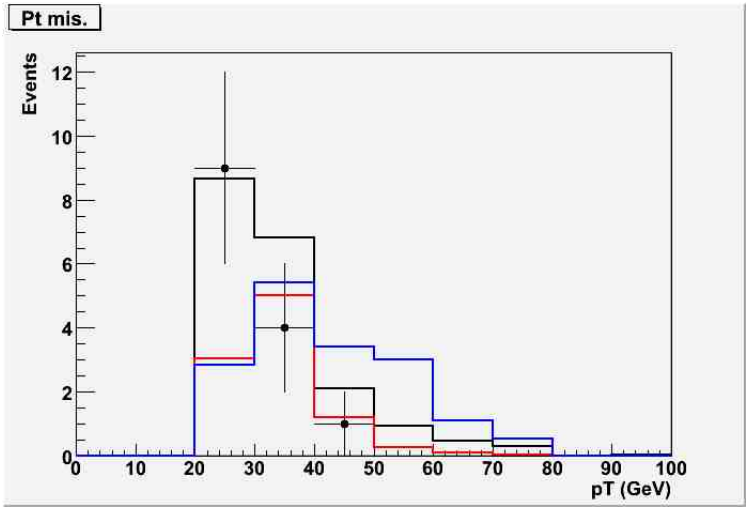

(a) p_T

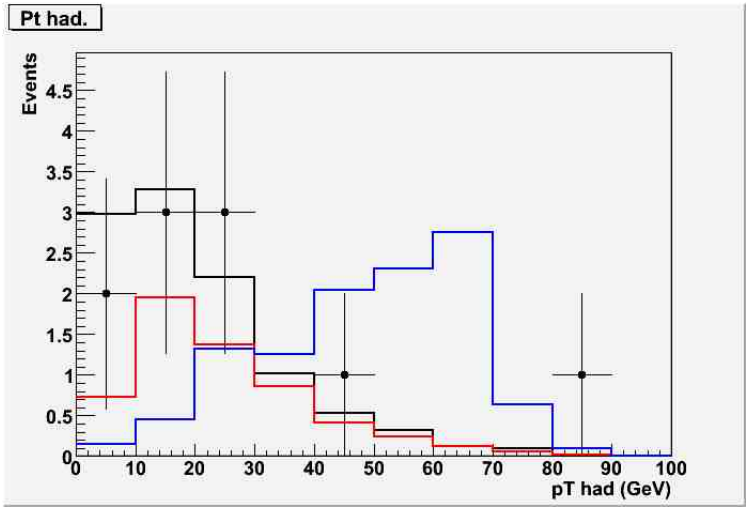

(b) p_T^{had}

Figure 6.25: *Plots of the p_T in the electron channel (a) and p_T^{had} in the muon channel (b); black dots are data, black histogram the total expected SM prediction, red is the W signal and blue is the single top in arbitrary normalisation.*

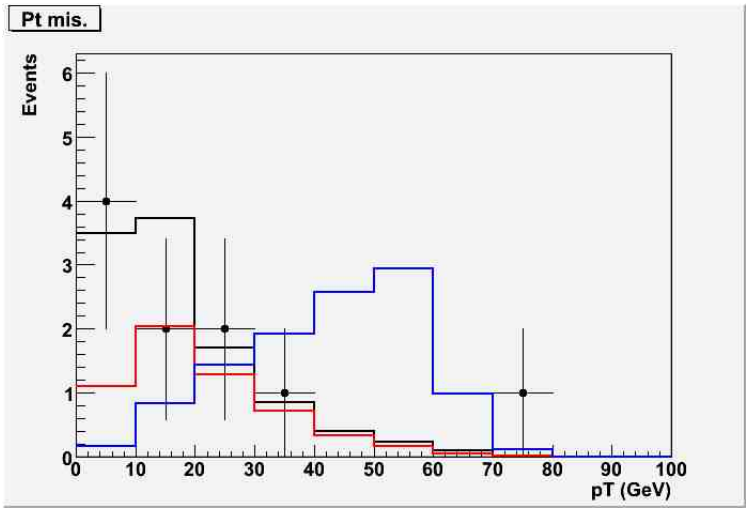

(a) p_T

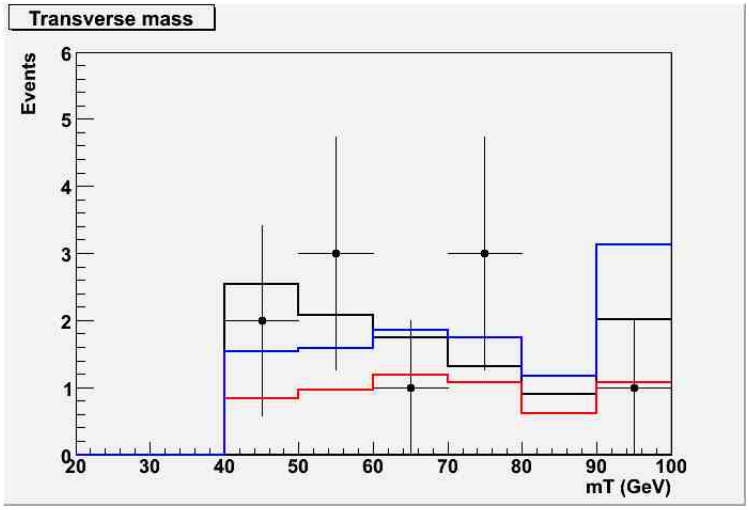

(b) M_T

Figure 6.26: *Plots of the p_T and M_T in the muon channel; black dots are data, black histogram the total expected SM prediction, red is the W signal and blue is the single top in arbitrary normalisation.*

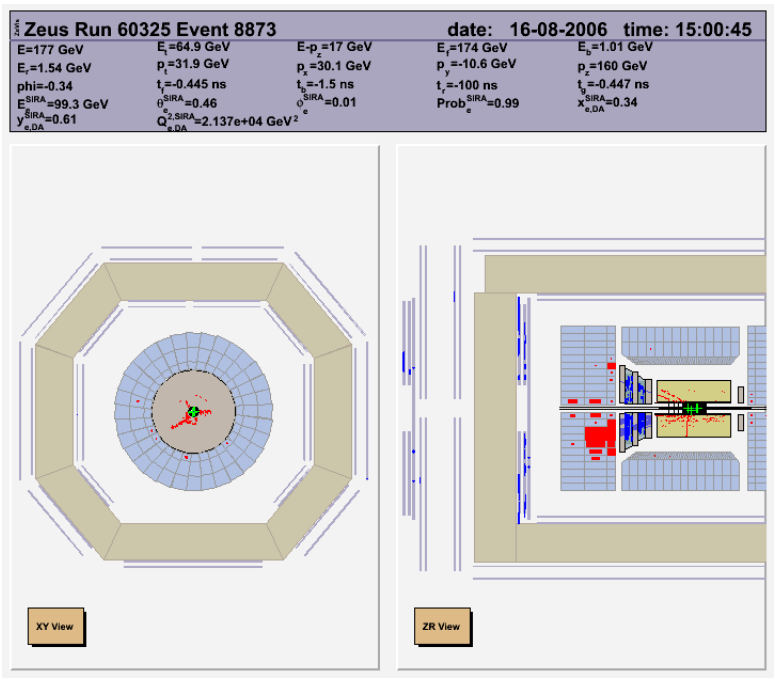

Figure 6.27: *A candidate event for the W decay in the electron channel.*

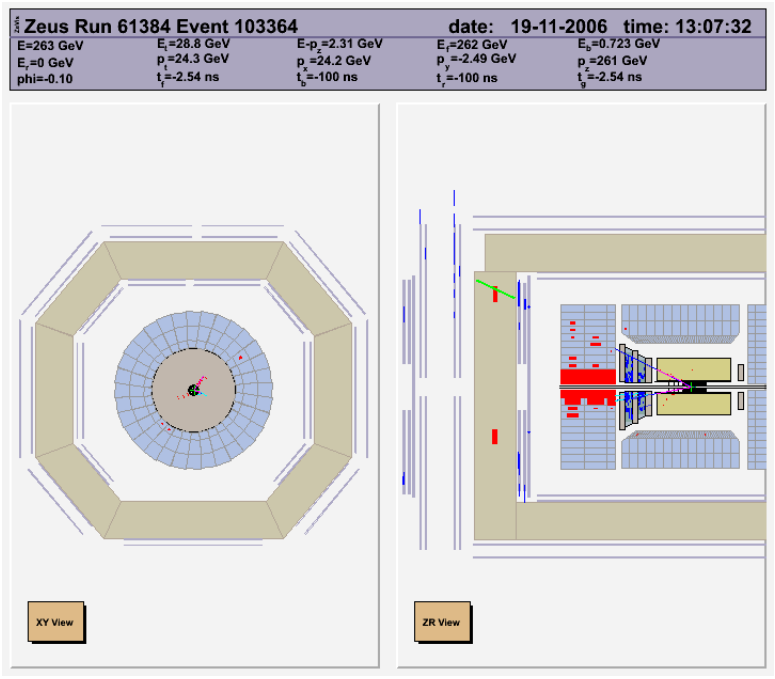

Figure 6.28: *A candidate event for the W decay in the muon channel.*

6.6 Search for single top

Differently for SM W production, single top events are characterised by large p_T^{had} due to the b-quark coming from the top decay This is clearly visible in Figs. 6.24 and 6.25 where the p_T^{had} distribution of W SM prediction and single top is shown.

The following further selection cut $p_T^{had} > 40.\,\text{GeV}$ has been hence imposed to the Data and MC.

Table 6.6 summarise the results of the final selection; uncertainties in the Table are statistical only.

Period	Lepton channel	Data	Monte Carlo	W
04-05e^-	e	0	0.70 ± 0.11 (CC)	0.40 ± 0.02
06-07e^+	e	0	0.57 ± 0.07 (CC)	0.39 ± 0.02
04-05e^-	μ	1	0.52 ± 0.07 (DIMUONS)	0.41 ± 0.02
06-07e^+	μ	1	0.59 ± 0.09 (DIMUONS)	0.45 ± 0.02

Table 6.6: *Observed and expected data after top selection for 06-07e^+ and 04-05e^- in the muon and electron channels. In parenthesis the background contribution. Uncertainties in the Table are statistical only.*

The two remaining events are shown, see Figs. 6.29 and the values of some kinematical variables are reported in Table 6.7

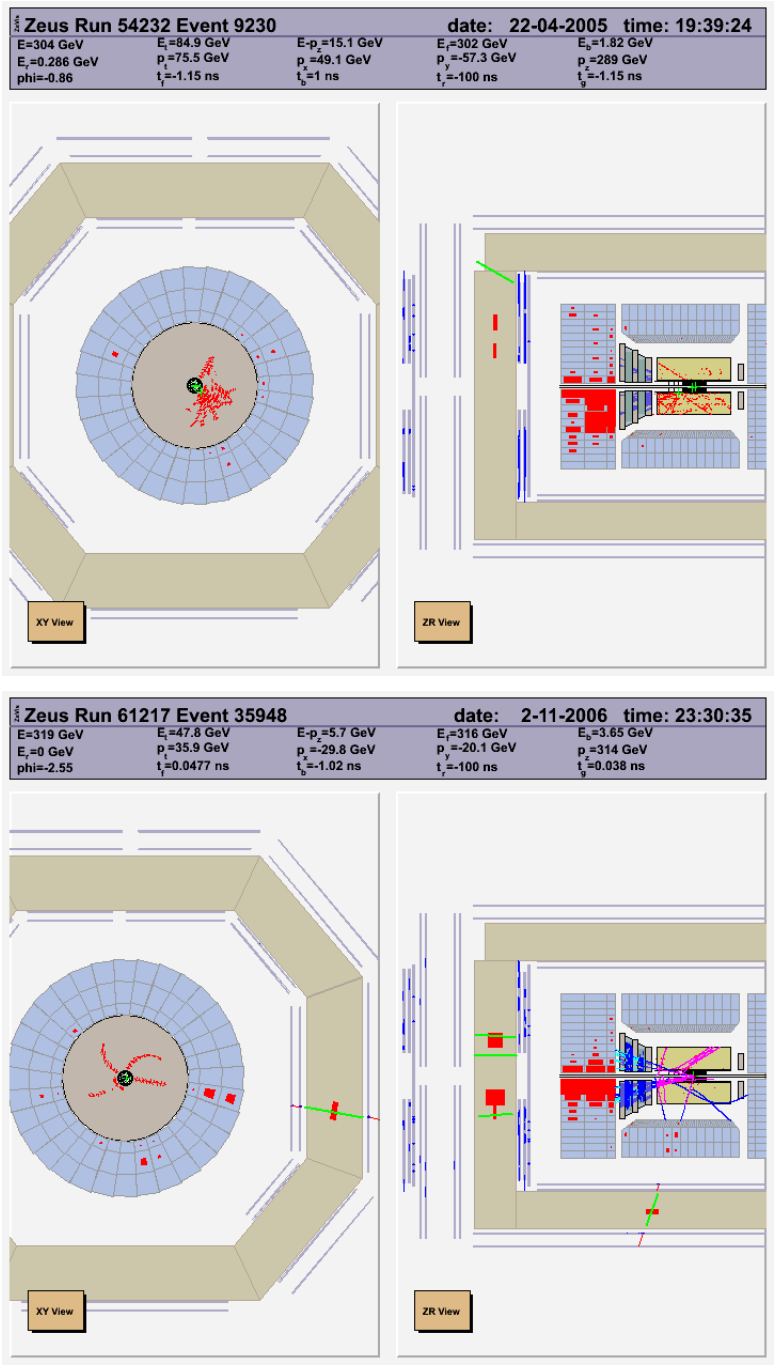

Figure 6.29: *Two remaining events in the muon channel after the top selection.*

run	evt	p_T^{corr} (GeV)	p_T^{had} (GeV)	M_T (GeV)
54232	9230	77.4	84.3	76.9
61217	35948	36.9	43.7	71.4

Table 6.7: *Two remaining events in the muon channel after the cut in* $p_T^{had} > 40.$ *GeV*.

Chapter 7

Single top limits

No events in the electron channel while 1.3 ± 0.2 are expected from SM and two events in the muon channel while 1.1 ± 0.2 are expected from SM have been selected after the final cuts. This chapter describes how this results has been used for setting limits single top production at HERA mediated by an anomalous $\kappa_{tu\gamma}$ FCNC coupling.

7.1 Limit calculation

Limits have been set using a Bayesian approach [70]. Given a set of experimental measurements $\vec{m}$, whose probability distribution depends on an unknown parameter p, the *a posteriori* probability distribution function (pdf) $f(p|\vec{m})$ gives the degree of belief of p to assume certain values given the set of measurements $\vec{m}$. According to the Bayes theorem, the $f(p|\vec{m})$ is:

$$f(p|\vec{m}) = \frac{L(\vec{m}|p)f'(p)}{\int L(\vec{m}|p')f'(p')dp'} \tag{7.1}$$

The quantity $L(\vec{m}|p)$ is the likelihood function and gives the probability of obtaining $\vec{m}$ given the value of the parameter p. The function $f(p)$ is the

prior probability and is the degree of knowledge of p before the experiment. The denominator is a normalisation factor so that $\int f(p|\vec{m})dp = 1$. In a counting experiment, the likelihood is given by a Poissonian distribution. Given N_{obs} observed events and N_{exp} expected events, the likelihood is:

$$L(N_{obs}|N_{exp}) = \frac{N_{exp}^{N_{obs}} e^{-N_{exp}}}{N_{obs}!} \tag{7.2}$$

The N_{exp} includes the number of background and signal events:
$N_{exp} = N_{bkg} + N_{sig}$ with $N_{sig} = \sigma\epsilon\mathcal{L}$ where σ is the signal cross section, ϵ the signal efficiency and $\mathcal{L}$ the luminosity of the data sample.

In our case, having four data samples (electron and muon channels for the periods 2004-2005 and 2006-2007), our total likelihood will be a product of the single likelihoods for each period (since they are independent).

$$L_{tot}(N_{obs}|(N_{bkg} + N_{sig})) = \prod_{i=1}^{4} \frac{(N_{bkg}^i + \sigma\mathcal{L}^i\epsilon^i)^{N_{obs}^i} exp^{-(N_{bkg}^i + \sigma\mathcal{L}^i\epsilon^i)}}{N_{obs}^i!}$$

Fig. 7.1 shows the plot of the four likelihoods. The likelihoods for the electron channels (red and black) give better constraints respect to the muon (green and blue) since no electron events are observed. Within the same channel, the slightly different shapes are due to the different luminosities of the two data samples, a bit higher for 2006-2007 (blue and red respectively for muon and electron channels). Signal efficiency have been evaluated using a simulation of the process done with CompHEP and PYTHIA (see Section 4.3.5) for a top mass of 175 GeV. The efficiency for our selection is 0.035 and 0.033 for the electron and muon channel, respectively. The efficiencies include also the branching ratio of top in the two channels. The dependence of the efficiency on the top mass has been investigated using signal samples generated wiht HEXF (see Section 4.3.5) at different top masses. The difference in efficiency between the generated value $M_{top} = 175$ GeV and the

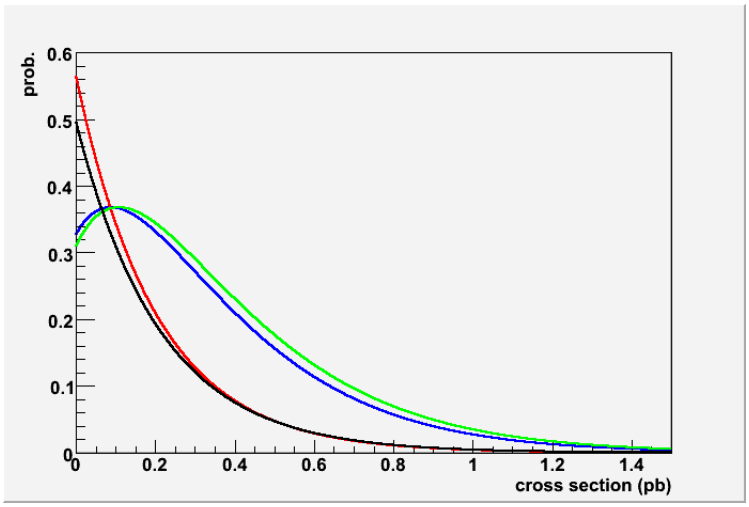

Figure 7.1: *Plot of the four likelihoods; in green and blue the samples 2004-2005 and 2006-2007 respectively for the muon channel and in black and red the samples 2004-2005 and 2006-2007 respectively for the electron channel.*

present measurement $M_{top} = 171.2 \pm 2.1$GeV [72] amounts to few percent and are neglected.

The 95% C.L. limit on the signal cross section is then obtained using a constant prior. The probability density function of the signal cross section and its integral are shown in Fig. 7.2(a) and (b) respectively. The limit (also shown in the figures) is: $\sigma < 0.25$ at 95% C.L. Such limit is comparable to that obtained in HERAI analysis [71]. This is due to the fact that, despite the higher integrated luminosity of the present data sample (a factor $\sim$2 larger) no events were observed in HERAI analysis and also the W hadronic decay was included in the single top search.

The cross section limit can be converted in limits on the $\kappa_{tu\gamma}$ coupling using CompHEP for the evaluation of the tree level cross section of the process. The corresponding limit on $\kappa_{tu\gamma}$ is: $\kappa_{tu\gamma} < 0.19$ at 95% C.L. The dependence of the limit on the top mass was also investigated varying the top

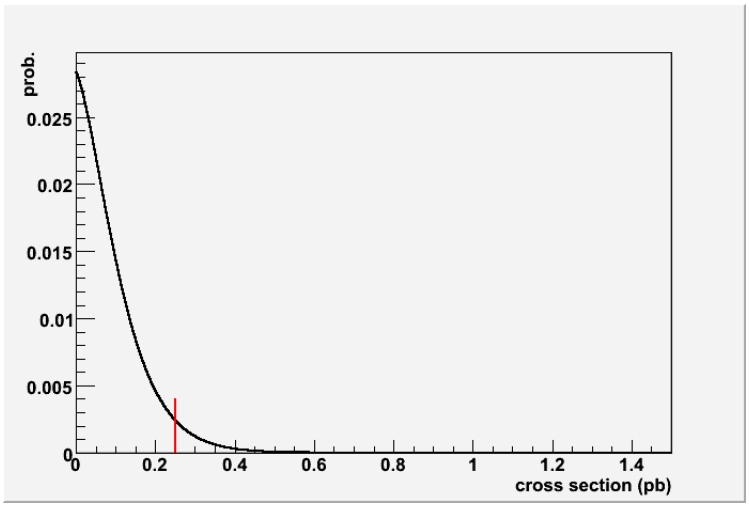

(a) *total pdf*

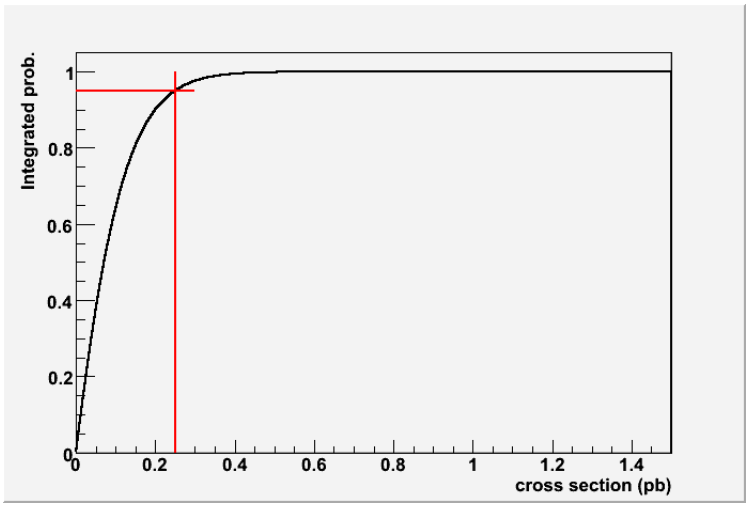

(b) *integrated probability*

Figure 7.2: *Plot of the pdf (probability density function) (a). In red the value of the cross section at 95% of C.L. (b) shows the integral of the pdf with the indication of the 95% C.L. limit.*

mass within its uncertainty ($\pm 2.1\,\text{GeV}$); the corresponding $\kappa_{tu\gamma}$ limit ranges between 0.18-0.20.

Conclusions

This thesis has presented a search for high p_T isolated leptons in events with large missing p_T at HERA. Both electronic and muonic channels have been studied. A data sample with a total integrated luminosity of 276.35 pb at $\sqrt{s} = 318\,\text{GeV}$ has been used. At HERA, events with high p_T leptons and high missing p_T are predominantly produced, within the SM, by processes leading to a single W in the final state. The total cross section of this processes is quite low ~ 1.2 pb.

Given the low expected rate and the clear topology, these kind of events are very well suited to look for possible signal of physics beyond the SM. One of the most plausible extra W production at HERA could be due to an anomalous single top production via a FCNC process involving a coupling $u - t - \gamma$ ($\kappa_{tu\gamma}$). Such events differently from ordinary W production, are characterized by large hadronic p_T due to the b-quark produced together with the W after the top decay.

The selection has started with a generic search for isolated electrons and muons in events with large missing transverse momentum. The sample selected has shown an acceptable agreement with the expectation of SM processes. Subsequently a selection optimized for W has been performed.

In the electron channel 14 events have been observed while 19.4 ± 1.3 were expected. In the muon channel 10 events were observed while 10.6 ± 0.9 were

expected. Since no excess beyond the SM expectation is observed, a final selection has been designed requiring high hadronic p_T in order to constrain single top production at HERA.

In the electron channel, no events have been observed while 1.3 ± 0.2 were expected, mainly from W production. In the muon channel, two events have been observed while 1.1 ± 0.1 were expected, mainly from W production.

These results have been combined to constrain the single top production. An upper limit on the cross section has been calculated and its value is 0.25 pb at 95% C.L. This value, has been used to put a constraint on the upper value of the $\kappa_{tu\gamma}$ FCNC coupling corresponding to 0.19 at 95% C.L. This is the first HERAII result on single top production of the ZEUS collaboration at HERA.

A similar analysis performed using HERAI data [71] and using also the hadronic decay of the W had obtained comparable results.

Acknowledgements

I would like to thank my supervisor Prof. G.Venturi; I would like to thank also all the ZEUS/ATLAS group in Bologna: Dott. M.Bindi, Dott. D.Boscherini, Dott.ssa A.Bruni, Dott. G.Bruni, Dott. M.Corradi, Dott. G.Iacobucci, Dott. A.Polini, Dott. L.Rinaldi and a very special thanks to Dott. L.Bellagamba.

Bibliography

[1] ZEUS Collab., The ZEUS detector, Status Report 1993, DESY (1993), available on `http://www-zeus.desy.de/bluebook/bluebook.html`

[2] HERA - *A proposal for a large electron-proton colliding beam facility at DESY*, Report DESY HERA 81/10, July 1981

[3] G. Ingelman, A. De Roeck, R. Klanner, Proceeding of the Workshop Future Physics at HERA, DESY(1995-1996)

[4] U. Schneekloth, DESY-HERA-98-05

[5] D.Bailey et al., *Study of beam-induced backgrounds in the ZEUS detector from 2002 HERA running* (unpublished), 2002, available on `http://www.zeus-desy.de/~kuze/zeusbg/`, ZEUS-Note 02-018
D. Bailey et al., *Study of beam-induced backgrounds in the ZEUS detector from 2002 HERA running (Addendum 1)* (unpublished), 2002, available on `http://www.zeus-desy.de/~kuze/zeusbg`, ZEUS-Note 02-020
D. Bailey et al., *Study of beam-induced backgrounds in the ZEUS detector from 2002 HERA running (Addendum 2)* (unpublished), 2003, available on `http://www.zeus-desy.de/~kuze/zeusbg/`, ZEUS-Note 02-027

[6] B.Parker et al., *HERA Luminosity Upgrade Superconducting Magnets Production at BNL*, BNL-68284

[7] DESY HERA 81-10 (81, REC.AUG.) 292p

[8] M.Seidel, DESY HERA-00-01

[9] N.Harnew et al., *Nuc. Inst. Meth.* **A 279** 290 (1989)
B.Foster et al., *Nucl. Phys. Proc. Suppl.* **B 32** 81 (1993)
B.Foster et al., *Nuc. Inst. Meth.* **A 338** 254 (1994)

[10] E.Maddox, *Study of heavy quark production at HERA using the ZEUS microvertex detector*, PhD thesis (2004)

[11] C.Coldwey, *Nuc. Inst. Meth.* **A 447** 44 (2000)

[12] M.Derrick et al., *Nuc. Inst. Meth.* **A 309** 77 (1991)
A.Andersen et al., *Nuc. Inst. Meth.* **A 309** 101 (1991)
A.Caldwell et al., *Nuc. Inst. Meth.* **A 321** 356 (1991)

[13] A.Berstein et al., *Nuc. Inst. Meth.* **A 336** 23 (1993)

[14] A.Barbenger et al., *Nuc. Inst. Meth.* **A 382** 419 (1996)

[15] G.Battistoni et al., *Nuc. Inst. Meth.* 176 297 (1980)

[16] A.Margotti, Diploma Thesis, University of Bologna (1990)

[17] G.Abbiendi et al., *Nuc. Inst. Meth.* **A 333** 342 (1993)

[18] T.Jezynski et al., Proc. SPIE 5484 180 (2004)
K.T.Pozniak et al., Proc. SPIE 5484 186 (2004)

[19] C.G.Callan and D.J.Gross, *Phys. Rev. Lett.* 22, 156 (1969)

[20] T.Han et al., *Phys. Rev.* **B 426**, 073008 (1998)

BIBLIOGRAPHY

[21] G.Altarelli, G.Parisi, *Nucl. Phys.* **B 126**, 298 (1977)
V.N.Gribov and L.N.Lipatov, Sov.J.Nucl.Phys. 15, 438 (1972)
Yu.L.Dokshitzer, Sov.Phys. JETP 46, 641 (1977)

[22] ZEUS Collab., S.Chekanov et al., Preprint DESY-02-105, 2002

[23] U.Baur, D.Zeppenfeld, *Nucl. Phys.* **B 325**, 253 (1989)

[24] P.Nason, R.Rückl and M.Spira, *J.Phys.* **G 25**, 1434 (1999)
M.Spira, Preprint DESY-99-060 (hep-ph/9905469) (1999)
K.P.Diener, C.Schwanenberger and M.Spira, *Eur. Phys. J.* **C 25**, 405 (2002)
K.P.Diener, C.Schwanenberger and M.Spira, Preprint hep-ex/0302040, (2003)

[25] CDF Coll., F.Abe et al., *Phys. Rev. Lett.* 74, 2626 (1995)

[26] DØ Coll., S.Abachi et al., *Phys. Rev. Lett.* 74, 2632 (1995)

[27] K.Hagiwara et al., *Phys. Rev.* **D 66**, 010001 (2002)

[28] M.Gell-Mann, *Phys. Lett.* 8 214 (1964)

[29] E.D.Bloom et al., *Phys. Rev. Lett.* 8, 214 (1964)

[30] J.D.Bjorken, *Phys. Rev.* 179, 1547 (1969)

[31] M.Gell-Mann, *Phys. Lett.* 8 1365 (1964)

[32] G.Zweig, CERN-8192/TH 401 (1964)
G.Zweig, CERN-8419/TH 402 (1964)

[33] R.P.Feynman, *Phys. Rev. Lett.*23, 1415 (1969)

[34] N.Cabibbo, *Phys. Rev. Lett.* 10, 531 (1963)
M.Kobayashi and T.Maskawa, Prog. Theor. Phys 49, 652 (1973)

[35] S.Moretti and K.Odagiri, *Phys. Rev.* **D 57**, 3040 (1998) [hep-ph/9709435]

[36] L3 Collaboration, P.Achard et al., *Phys. Lett.***B 549**, 290 (2002)

[37] G.Gustafson, U.Petterson, *Nucl. Phys.* **B 306**, 746 (1988)
B.Anderson et al., *Z. Phys.* **C 43**, 625 (1989)

[38] B.Andersson et al., *Phys. Rev.* **97**, 31 (1983)

[39] R.D.Field and S.Wolfram, *Nucl. Phys.* **B 213**, 65 (1983)
B.R.Webber, *Nucl. Phys.* **B 238**, 492 (1984)

[40] G.Marchesini et al., *Comp. Phys. Comm.* **67**, 465 (1992)

[41] H.L.Lai et al., *Phys. Rev.* **D 55**, 1280 (1997)

[42] M.Gluck, E.Reya and A.Vogt, *Phys. Rev.*, **D 46**, 1973 (1992)

[43] A.Kwiatkowski, H.Spiesberger and H.-J.Möhring, *Comp. Phys. Comm.* **69**, 155 (1992). Also in *Proc. of the Workshop on Physics at HERA*, 1991, DESY, Hamburg

[44] G.A.Schuler and H.Spiesberger, *Proc. of the Workshop on Physics at HERA* G.Ingelman, Proceedings of the Workshop Physics at HERA, vol.3, DESY 1992, 1419

[45] CTEQ Coll., H.L.Lai et al., *Eur. Phys. J.* **C 12**, 375 (2000)

[46] L.Lönnblad, *Comp. Phys. Comm.* **71**, 15 (1992)

[47] T.Abe, *Comp. Phys. Comm.* **136**, 126 (2001)

[48] U.Baur, J.A.M.Vermaseren, D.Zeppenfeld, EPVEC 1.1: A parton level Monte Carlosimulation package for W and Z production in ep collisions, *Nucl. Phys.* **B 375**, 3 (1992)

[49] R.Brun et al., GEANT 3.13: Detector Descriptions and Simulation Tools, CERN DD/EE/84-1 (1987)

[50] `http://giroz.desy.de/components/funnel/MONTE_CARLO/MOZART_desc.html`

[51] R.van Woudenberg, ZGANA Version 3.05/01, User manual and Documentation, (1993)

[52] E.Tschelog, ZEUS Reconstruction Program, Organization and Control, ZEUS-note 91-37, internal report

[53] S.M.Fisher, P.Palazzi, ADAMO programmers Manual-Version 3.2 CERN Programming Techniques Group ECP Division, available on `http://adamo.web.cern.ch/Adamo/`

[54] T.Sjöstrand, *Comp. Phys. Comm.* **39**, 347 (1986)
T.Sjöstrand and M.Bengtsson, *Comp. Phys. Comm.* **43**, 367 (1987)
T.Sjöstrand, *Comp. Phys. Comm.* **82**, 74 (1994)

[55] K.0.Diener, C.Schwanenberger and M.Spira, Preprint hep-ex/0302040, 2003

[56] H.J.Kim and S.Kartik, Preprint LSUHE-145-1993, 1993

[57] E.Boos et al., *Nuc. Inst. Meth.* **A 534** 250 (2004)
A.Pukhov et al., CompHEP - a package for evaluation of Feynman diagrams and integration over multi-particle phase space. User's manual

for version 3.3, INP MSU report 98-41/542
Home page: http://comphep.sinp.msu.ru

[58] K.Hagiwara, S.Komamiya and D.Zeppenfeld, *Z. Phys.* **C 29**, 115 (1985)

[59] F.Boudjema, A.Djouadi and J.L.Kneur, *Z. Phys.* **C 57**, 425 (1993)

[60] H.Baer, J.Ohenemus, J.F.Owens, *Z. Phys.* **C 42**, (1992) 404

[61] G.Ingelman, A.Edin and J.Rathsman, *Comp. Phys. Comm.* **101**, 108 (1997)

[62] T.Sjöstrand, *Comp. Phys. Comm.* **67**, 465 (1992)

[63] G.Hartner, VCTRAK: Online Output Information, ZEUS-Note 97-064

[64] ZEUS Collab., J.Breitweg et al., *Z. Phys.* **C 74**, 207 (1997)
A.Kappes, Verwendung von neuronalen netzen zur identification des gestreuten Elektrons in *ep* Ereignissen mit hohen Q^2 bei ZEUS, Diploma thesis, Universität Bonn, Bonn, Germany, Report BONN -IB-97-28, 1997, available on http://www-zeus.physik.uni-bonn.de/german/diploma.html
http://www-zeus.desy.de/~straub/ZEUS_ONLY/doc/em.ps
http://www-zeus.desy.de/~straub/ZEUS_ONLY/doc/em.v1.6.html

[65] V.Kuzmin, *Nuc. Inst. Meth.* **A 453**, 336 (2000)

[66] S.Catani et al., *Nucl. Phys.* **B 406**, 187 (1993)

[67] S.D.Ellis and D.E.Soper, *Phys. Rev.* **D 48**, 3160 (1993)

[68] M.H.Seymour, *Nucl. Phys.* **B 513**, 269 (1998)

[69] T.Matsushita, *Search for events with a high energy isolated lepton and large missing transverse momentum in ep collisions at* $\sqrt{s} = 300\,GeV$., PhD thesis, Tokio Metropolitan University, Tokio (Japan), 1998

[70] G.D'Agostini, Bayesian Reasoning in High Energy Physics -Principles and Applications-, CERN Yellow Report 99-03, July 1999
M.Corradi, *Proceedings of the Workshop on Confidence Limits*, F.James, L.Lyons, Y.Perrin (ed.), Geneva, Switzerland, CERN (2000), 237. Available at `http://doc.cern.ch/yellowrep/2000/2000-005/p237.pdf`
G.D'Agostini, *Probability and measurement uncertainty in physics: a bayesian primer*, DESY 95-242

[71] ZEUS Collab., S.Chekanov et al., *Phys. Lett.* **B 559**, 153 (2003)

[72] *Phys. Lett.* **B 667/1**, 568 (2008)

[73] W.H.Smith, K.Tokushuku and L.W.Wiggens *Proc. Computing in High-Energy Physics (CHEP)*, Annecy, France, Sept.1992, C.Verkerk and W.Wojcik (eds), p.222, CERN, Geneva, Switzerland(1992). also in preprint DESY 92-150B